THESIS

MODELING ABLATIVE AND REGENERATIVE COOLING SYSTEMS FOR AN ETHYLENE/ETHANE/NITROUS OXIDE LIQUID FUEL ROCKET ENGINE

Submitted by

Elizabeth C. Browne

Department of Mechanical Engineering

In partial fulfillment of the requirements

For the Degree of Master of Science

Colorado State University

Fort Collins, Colorado

Summer 2020

Master's Committee:

Advisor: Anthony Marchese
Co-Advisor: Bret Windom

Ted Watson

ABSTRACT

MODELING ABLATIVE AND REGENERATIVE COOLING SYSTEMS FOR AN ETHYLENE/ETHANE/NITROUS OXIDE LIQUID FUEL ROCKET ENGINE

Rocket engines create extreme conditions for any material to withstand. The combustion temperatures in rocket engines are substantially greater than the melting points of metals, and wall temperatures must be maintained well below the melting point to ensure structural integrity. This requirement necessitates a robust cooling system for the combustion chamber and nozzle to endure the mandated burn times. A liquid rocket engine utilizing ethane/ethylene as the fuel and nitrous oxide as the oxidizer, which is currently under development by Pioneer Astronautics, required a detailed analysis of thrust chamber cooling options. Due to the impracticality of experimentally validating the performance of each design parameter, this thesis employed computational methods to investigate two common cooling systems for rocket engines - ablative and regenerative - to determine their effectiveness at 130 and 200 chamber pressures, as prescribed by Pioneer Astronautics. Additional 1000-psi chamber pressure models were investigated for prediction validation. An analytical model was developed and utilized to elucidate the behavior of both cooling methods, while regenerative cooling was additionally analyzed using numerical modeling, coupling finite element analysis (FEA) and computational fluid dynamics (CFD) software. Simulations were created of the fluid dynamics and heat transfer within the rocket engine and coolant channels for numerous regenerative designs. The designs examined included a single-channel model utilizing only the liquid ethylene/ethane fuel as the coolant, and a dual-channel model using both the fuel and the nitrous oxide as coolants in separate sets of channels. In the single-channel regenerative cooling design, both the analytical and numerical models exhibited insufficient cooling capacity with coolant temperatures of 3-11 K above the critical temperature of 292.5 K. However, the dual-channel model provided the supplemental thermal energy absorption necessary to maintain

engine wall and coolant temperatures within the allowable limits. From a design and manufacturing standpoint, ablative cooling is far simpler to implement than regenerative cooling. Although, material erosion at the throat reduces engine performance over time. Integrating ablative cooling in the combustion chamber and nozzle bell with dual-channel regenerative cooling near the throat has the potential to provide the requisite heat removal to ensure sustained material strength while maintaining all reactants in a condensed liquid phase.

ACKNOWLEDGEMENTS

I would like to thank the CSU Graduate Student Council and the CSU Graduate School for initiating, commissioning and supporting this project. I would also like to thank Anthony Marchese and Bret Windom for their support and ensuring that we followed through with this project to completion. I would like to thank my daughters Louise Browne, Kalia Gregory, and Savannah Browne for their tireless patience and encouragement. I would like to thank Steve Cox, Ivan Lopez, Ashis Nandy, Ana Vasilic, Ruth Hidalgo, Mike Beddo and Claudia Aprea for their guidance and generous bestowal of knowledge. They changed the trajectory of my life, and I could not be more grateful. I would like to thank Robert Reines and William W. Saylor for their insight and encouragement. I want to thank my extensive community of family and friends for their deeply rooted support and love, which make my endeavors possible. Lastly, I would also like to thank my parents, for everything I have achieved is because of them.

DEDICATION

I would like to dedicate this thesis to my dad. He taught me that I can overcome any obstacle if I set my mind to it. As Norman Vincent Peale stated, "Shoot for the moon. Even if you miss you'll land among the stars."

TABLE OF CONTENTS

LIST OF TABLES

LIST OF FIGURES

LIST OF SYMBOLS

The next list describes several symbols that will be later used within the body of the document.

Δ	change	$dimensionless$
$\dot{m}$	Mass flow rate	$\frac{kg}{s}$
$\dot{Q}$	Heat transfer rate	W
γ	Specific heat ratio	$dimensionless$
μ	Dynamic viscosity	$Pa \cdot s$
ρ	Density	$\frac{kg}{m^3}$
A_{cs}	Cross-sectional area	m^2
A_s	Surface area	m^2
C^*	Characteristic velocity	$\frac{m}{s}$
c_p	Specific heat capacity at constant pressure	$\frac{J}{kg \cdot K}$
E_{r_t}	Erosion rate	$\frac{mm}{s}$
f	Friction factor	$dimensionless$
h	Convection coefficient	$\frac{W}{m^2 \cdot K}$
I_{sp}	Specific impulse	s
K	Kelvin	$dimesnionless$
k	Thermal conductivity	$\frac{W}{m \cdot K}$
M	Mach number	$dimesnionless$
m	Mass	kg

Nu	Nusselt number	$dimensionless$
P	Pressure	psi, $Pa\ or\ MPa$
Pr	Prandtl number	$dimensionless$
Re	Reynold's number	$dimensionless$
T	Temperature	K
t	Time	s
u	Directional velocity component	$\frac{m}{s}$
v	Velocity	$\frac{m}{s}$
X	Mole fraction of molecular species specified by subscript	$dimensionless$
x	x axis of Cartesian coordinate	$unitless$
y	y axis of Cartesian coordinate	$unitless$
z	z axis of Cartesian coordinate	$unitless$
q	Heat flux	$\frac{W}{m^2}$

Chapter 1

Introduction

To design a high-performance rocket engine capable of long burn durations and reliable ignition, it is paramount to have precise predictions of the behavior of chemical kinetics, fluid mechanics, thermodynamics, heat transfer, and temperature-dependent material properties. Rocket engines are propelled by exhausting high-temperature gas from the combustion chamber through a supersonic nozzle. Propulsion can be achieved using a range of energy sources including chemical, nuclear, solar, and electrical; however, this research focused on chemical rocket propulsion.

Chemical propulsion can be further categorized by propellant type, liquid, solid, and hybrid fuel. Liquid fuel rocket engines require storage tanks, pumps, and injectors; however, they allow combustion cessation and re-ignition which facilitates steering and increases application potential. Solid fuel rocket engines do not require the complicated mechanics of liquid fuel, although once ignited the fuel burns until the charge has been exhausted. Hybrid fuel rocket engines typically use solid fuel and a liquid oxidizer, albeit, a variety of propellant combinations have been explored. Hybrid rocket engines assume the relative safety and simplicity of solid fuel as well as the start-stop capability of liquid fuel but tend to have decreased performance.

The extreme temperature gradients found in rocket engines and the upper atmosphere cause high heat transfer rates and significant material stress. Combustion temperatures in rocket engines typically range from 2700 K to 3600 K, which is substantially higher than the melting point of metals. This necessitates a sagacious cooling system to extend engine lifespans, despite enduring harsh conditions for prolonged burn times. There are numerous cooling methods for rocket nozzles, including dump, film, transpiration, radiation, ablative, and regenerative cooling. Ablative and regenerative cooling are two of the most commonly utilized methods and were therefore chosen as the cooling methods to be investigated for this research.

Ablative cooling is a process that utilizes a sacrificial liner which cools the engine through chemical reactions and the enthalpy of vaporization, which is the energy expended to induce a

phase change. During a phase change, the temperature of the material remains fixed. Ablative materials can be categorized into two types, pyrolyzing and non-pyrolyzing. Pyrolyzing materials are usually composites made up of a silica or carbon fiber matrix embedded with a resin. When exposed to the high-temperature combustion products, the resin undergoes an endothermic degradation. This causes the material to char and pyrolysis gas to evaporate into the boundary layer. Non-pyrolyzing materials, such as carbon and graphite, melt or sublimate causing thermochemical erosion at the surface. The charring and melting temperatures of ablative materials are low enough to ensure the strength of the nozzle wall; however, material erosion reduces the performance of the rocket engine by changing the supersonic area ratio with time.

Regenerative cooling incorporates the flow of pressurized propellants on the exterior surface of the rocket nozzle. Flowing liquid along the outside surface of the nozzle wall acts as a heat exchanger by absorbing thermal energy through convection. In the process, the fuel is preheated, which resembles a regenerative heating cycle, hence the name. Additionally, the material between the cooling channels behaves like cooling fins by transferring heat from the engine to the atmosphere through conduction. The efficacy of regenerative cooling soon led to it becoming the most widely utilized method for cooling rocket engines; however, sufficient regenerative cooling requires relatively high mass flow rates characteristic of large rocket engines. The development of a scalable regenerative cooling design capable of absorbing ample thermal energy is cardinal to meeting the ever-increasing demand of small payload engines, such as for low-Earth orbit (LEO) launches. LEO launches are frequently deployed for placing small satellites in orbit, which have an extensive range of applications but are more challenging to cool regeneratively due to the smaller engines having lower mass flow rates.

Liquid rocket fuels offer notable advantages over solid fuels; however, they also require more complex designs due to the pressurization and injection of the propellants. One considerable convenience of Liquid Rocket Engines (LREs) is the ability to throttle, stop, and reignite. Additionally, LREs enable the potential use of the fuel as a coolant; however, liquid fuels have a relatively small temperature gradient before a phase change occurs. Two-phase flow demands a more complicated injector design to accommodate the transient behavior inherent to a phase change; therefore, fuel is

generally injected as a liquid due to the simplified physics of the homogeneous operation. Reserving the limited single-phase temperature gradient for regions near the throat of the nozzle which experience the highest heat flux allows for the most appreciable benefit. The geometry developed in SolidWorks of the proposed rocket nozzle with a supersonic area ratio of 100, and dual sets of cooling channels in a housing near the throat is depicted in Figure 1.1.

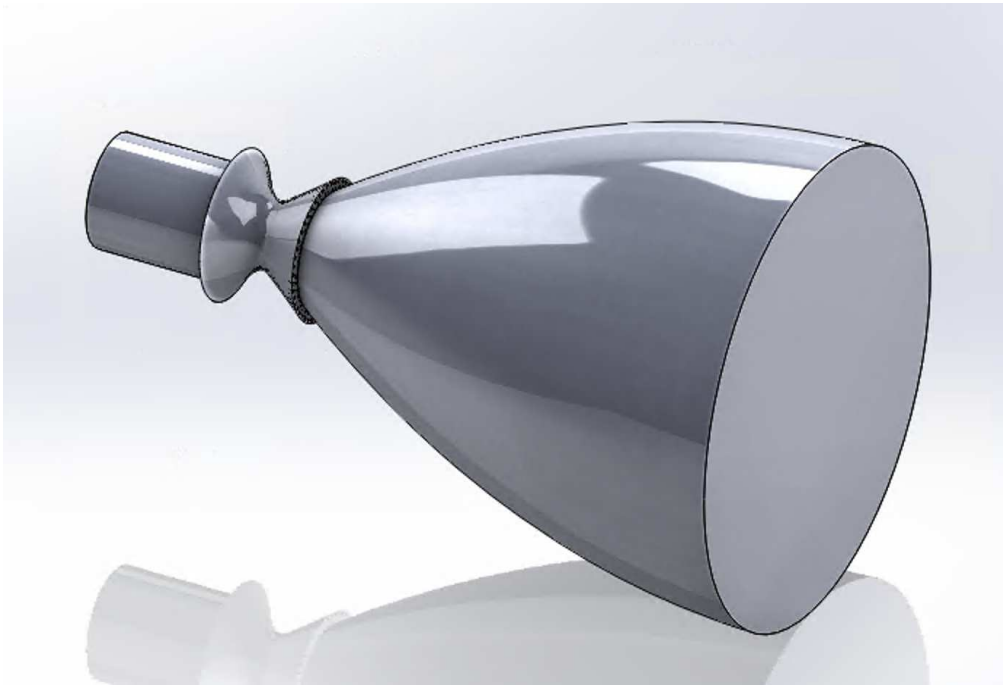

Figure 1.1: Proposed rocket nozzle with dual-channel regenerative cooling channels

It is impractical to physically validate the performance of each design specification, and calculating outcomes mathematically saves critical time and resources. Consequently, this thesis employed computational methods to investigate ablative and regenerative cooling systems for liquid fuel rocket engine (LRE). Ablative cooling was studied with an analytical model for a range of pyrolyzing and non-pyrolyzing materials at various chamber pressures to determine the effects on erosion rates, heat flux, and wall temperatures. Regenerative cooling was examined using both analytical and numerical models for an array of designs, including annular cooling, a single-channel design consisting of a set of fifty rectangular C_2H_4/C_2H_6 cooling channels, as well as a

dual-channel design with both C_2H_4/C_2H_6 and N_2O as coolants flowing in separate sets of fifty channels each. The channels were situated inside of a steel housing enveloping the nozzle from the interface of the combustion chamber and the converging section to a supersonic area ratio of 5.9423 in the diverging section.

The analytical and numerical models both assumed steady-state. In the analytical model the convection coefficients were solved for using an empirical correlation, and the thermal resistance was solved in one-dimension for in the cooled section of the nozzle for over four hundred differential slices creating a quasi 2D solution. The CFD utilized for the numerical modeling solves the Naiver-Stokes equations as opposed to using empirical correlations, and therefore does not consider internal convection. The numerical modeling was performed with finite element analysis (FEA) and computational fluid dynamics (CFD) software. The employment of software simulations has proven to be a powerful tool for determining the most efficient design specifications by elucidating the fluid dynamics and heat transfer behavior within the rocket engine and cooling channels. Simulations were subsequently created in both 2D and 3D of the uncooled and annularly cooled models. Additional 3D simulations were developed for the proposed single-channel and dual-channel regenerative cooling designs. The models were compared to determine the optimal design for enabling the engine to tolerate long burn durations and increase the lifespan of the engine.

Chapter 2

Background

Rocket engines are constructed of a combustion chamber exhausting through a supersonic nozzle. The nozzle consists of a converging section from the combustion chamber to the throat, or most narrow cross-section of the nozzle, and a diverging section from the throat to the exit. The combustion products provide the necessary high temperatures and pressures to induce the conversion into high-velocity exhaust gas. In supersonic flow, a preponderance of enthalpy is converted into kinetic energy resulting in thrust. Thrust force is due to Newton's third law of physics, the conservation of momentum. The pressure force on the wall are balanced by the equal and opposite reaction force by the walls; however, the pressure force at the exit is not compensated for. The high velocity gas exiting the nozzle propels the rocket in the opposite direction, as seen in Figure 2.1 [1].

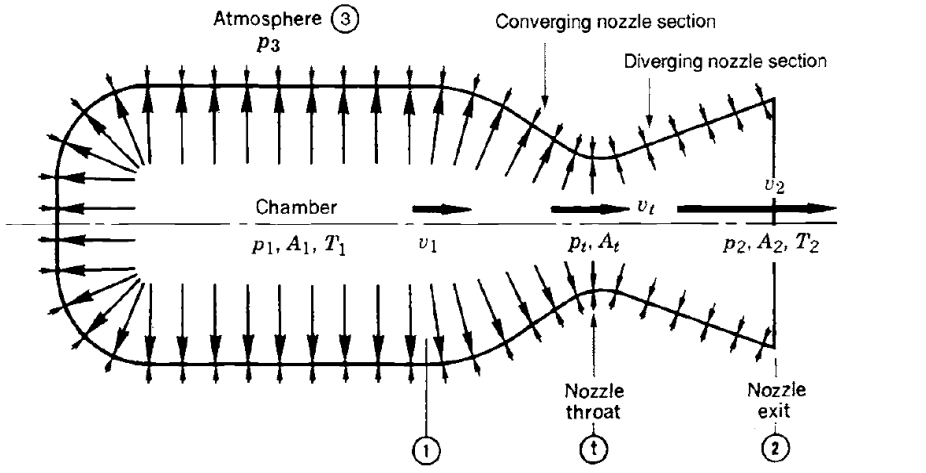

Figure 2.1: Rocket propulsion principles
[1]

The nozzle geometry produces high velocities by choking the high-pressure combustion gas through the throat. The geometrical convergence causes the pressure to decrease, and thus the velocity to increase from subsonic in the combustion chamber to Mach 1 at the throat. The subsequent rapid thermodynamic expansion of the gas into the diverging section causes the velocity to become supersonic. Mach number is the ratio of the velocity of the moving body to the velocity of the speed of sound in the same medium. A Mach number of one indicates that the body is moving at the speed of sound in the given medium. Mach numbers less than one are called subsonic, while Mach numbers greater than one are supersonic. Local Mach numbers in rocket engines are referring to the velocity of the exhaust flow. The local Mach number is calculated at a particular location within the nozzle by:

$$M_x = v_x \sqrt{\gamma R T_x} \tag{2.1}$$

where the subscript x implies at a given location in the nozzle, M is the Mach number, v is the velocity, γ is the specific heat ratio, R is the gas constant for the particular gas, and T is the absolute temperature in Kelvin.

The expansion area ratio of the exit to the throat combined with the chemical kinetics of the fuel determines what Mach numbers can be achieved, as well as the exit pressure. Rocket engines are considered perfectly expanded and have the most efficient performance when the outlet pressure is equal to the ambient pressure. Due to the precipitous altitude changes inherent to rockets, and the subsequent rapidly changing atmospheric pressure, a rocket engine would ideally have a dynamic expansion area ratio that adjusted with altitude. However, because thus far rockets have only been viable for one flight, this would involve impractical mechanical design complications. Since a dynamic area ratio is not yet feasible, the nozzle needs to be designed with an area ratio that is operative over a wide range of altitudes but most efficient at the target ambient pressure [1].

If the exit pressure is greater than the ambient pressure, the rocket is under-expanded, which would normally be seen in the vacuum of space, as seen on the left in Figure 2.2. This prevents the exhaust gas from fully expanding, which lowers the velocity due to less enthalpy being converted to kinetic energy. If the exit pressure is less than the ambient pressure the rocket is over-expanded,

which is often the case at sea level, as seen on the right in Figure 2.2. This causes shock waves to occur at the exit of the nozzle, and kinetic energy to convert back to enthalpy. In both the under and over-expanded cases, there is a notable reduction in thrust. The two adverse pressure ratio cases, as well as the perfect expansion case, are depicted in Figure 2.2 [1].

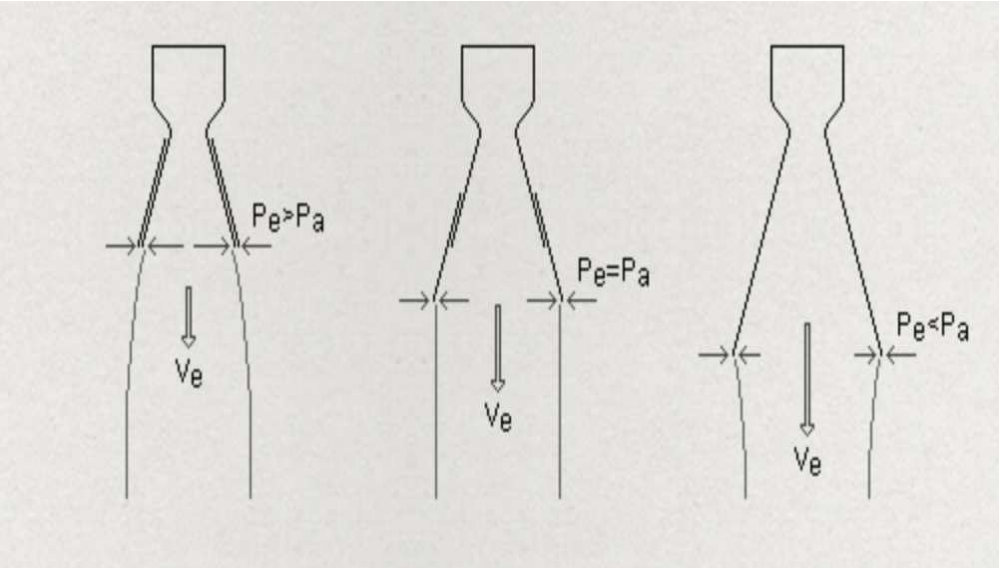

Figure 2.2: Rocket nozzle efficiency with respect to pressure ratio
[1]

The thrust force of the rocket engine is a function of pressure, exit velocity, and mass flow rate. This equation for thrust force further shows that when the exit pressure is equal to the ambient pressure the maximum thrust is achieved.

$$F_t = \dot{m} \cdot v_e + (P_e - P_a)A_e \tag{2.2}$$

where F_t is the thrust force in N, $\dot{m}$ is the mass flow rate in kg/s, v_e is the exit velocity in m/s, P_e is the exit pressure, P_a is the ambient atmospheric pressure in Pascals, and A_e is the cross-sectional area of the exit of the nozzle in m^2. The perfectly expanded nozzle, with an outlet pressure equal to the ambient pressure, attains the maximum thrust force possible, as seen in Figure 2.3 [1].

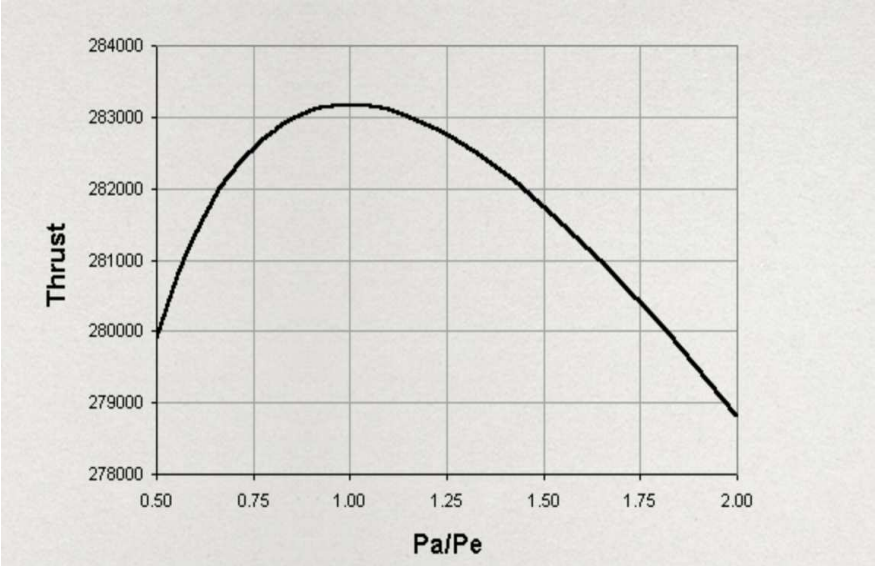

Figure 2.3: Thrust vs pressure ratio curve
[1]

Rocket engines need to carry enough fuel for the entirety of the expedition; therefore, to reduce the weight to thrust ratio it is necessary to design a high-efficiency nozzle. Utilizing fuels with high concentrations of hydrogen decreases the molecular weight of the exhaust and improves engine performance. Additionally, increasing combustion temperature increases efficiency. Specific impulse is indicative of the engine efficiency, and therefore a commonly calculated parameter for rocket engine design. Specific impulse is calculated using:

$$I_{sp} = \frac{F_t}{\dot{m} \cdot g_o} \tag{2.3}$$

where I_{sp} is specific impulse in seconds, and g_o is gravity at sea level in m/s^2. It can be seen from this equation that I_{sp} is inversely proportional to the mass flow rate, evidence that reducing molecular mass increases engine performance [1]. Characteristic velocity, C^*, also shows the merit of a rocket engine's performance. C^* is a convenient assumption, which simplifies the velocity calculations by eliminating the radial velocity gradients. C^* is calculated by:

$$C^* = \frac{P_c A_t}{\dot{m}} \tag{2.4}$$

Rocket design relies on numerous ideal rocket assumptions. These assumptions have been shown to give performance values ranging from 1% - 6% lower than measured values, which is negligible in comparison to the computational gains of the greatly simplified calculations. According to Sutton, the assumptions include: homogeneous chemical reactions, the chemical products obey ideal gas law due to high combustion temperatures, adiabatic flow, frictionless flow allowing boundary layer effects to be neglected, steady flow with no internal shock waves, velocity only in the axial direction, uniform gas properties at any cross-section, and chemical equilibrium established in the combustion chamber and maintained throughout nozzle. For adiabatic flow, the conservation of energy equations can be used, and for ideal gases, the enthalpy can be easily calculated. Adiabatic flame temperature assumes no changes in kinetic or potential energy giving the highest combustion temperature achievable for the particular propellant. Since the flow is assumed to be steady with no shock waves, isentropic expansion calculations can be used for the flow inside the nozzle [1]. These assumptions were exploited in the analytical analysis for this thesis, although the effects of thermal boundary layers in both the nozzle and the regenerative cooling channels were explored in the numerical models. In both the numerical and analytical analyses steady-state was also assumed.

2.1 Ablative Cooling

Ablative cooling is a process that utilizes a sacrificial liner to cool the engine through chemical reactions and the enthalpy of vaporization. The latent heat of vaporization, h_{fg}, is the thermal energy required to break molecular bonds during a phase change in a constant pressure process. Ablative liners are lightweight, relatively simple to implement, and inexpensive. Due to the typically low thermal conductivity of ablative materials, they reduce heat transfer rates to the rocket housing from the combustion gas and effectively insulate the nozzle walls. A preliminary survey was conducted of both historic and more recent peer-reviewed research papers for comparable erosion rates of a variety of ablative materials, accounting for the design specification differences of the rockets. The intention was to determine the most durable ablative material to keep the chamber

and nozzle walls within the allowable temperature range to ensure material soundness, while also exhibiting low enough recession rates to maintain engine efficiency.

2.1.1 Ablative Materials

Ablative materials can be separated into two main categories; pyrolyzing and non-pyrolyzing. Pyrolyzing materials are composites made up of a reinforcing fiber matrix impregnated by a resin, often phenolic or epoxy, whereas carbon-carbon and graphite are non-pyrolyzing materials. Pyrolysis causes an irreversible chemical alteration of the material that creates a highly carbonaceous char on the surface and diffuses pyrolytic gases into the flow. Pyrolytic gases, which have negligible oxidizing species present, are injected into the boundary layer forcing oxidizing species away from the surface and reducing the erosion rates. As the material pyrolyzes, the enthalpy of vaporization converts an immense amount of thermal energy into latent energy associated with the material phase change. Latent energy breaks the molecular bonds of the material as opposed to heating it, which allows the subsurface temperatures to remain within the material limits [2].

With non-pyrolyzing materials, heterogeneous thermochemical reactions occur at the surface between the thermal protective material and oxidizing species in the combustion gas. These reactions decrease temperatures in the boundary layer keeping the surface cooler, but also precipitate mass consumption and material recession [3]. Recession rates are dependent on the complicated relationship between pressure, propellant composition, chemical kinetics, burn duration, nozzle geometry, and ablative material properties. Recession at the throat of the nozzle reduces the supersonic area ratio and thus many performance parameters, including the exit velocity of the exhaust gas. The local velocity, v_x, within the rocket nozzle can be calculated by:

$$v_x = \frac{\dot{m} V_x}{A_x} \tag{2.5}$$

where V_x is the specific volume in m^3/kg, which is the inverse of density, ρ in kg/m^3. Substituting the equation for the velocity at the exit into the equation for thrust force and including the thrust coefficient gives:

$$F_t = \frac{C_f \dot{m}^2}{\rho_e A_e} \tag{2.6}$$

where F_t is thrust force in N, $\dot{m}$ is the mass flow rate in kg/s, v_e is the exit velocity in m/s, and C_f is the thrust coefficient. The thrust coefficient represents the amplification of the thrust due to the thermodynamic expansion in the bell of the supersonic nozzle. The equation for thrust coefficient is:

$$C_f = \frac{v_e^2 A_e}{P_c A_t v_e} + \frac{P_e A_e}{P_c A_t} - \frac{P_a A_e}{P_c A_e} \tag{2.7}$$

where A_e is the cross-sectional area at the exit of the nozzle in m, P_c is the chamber pressure in Pa, A_t is the cross-sectional area at the throat in m, P_e is the exit pressure in Pa, and P_a is the ambient pressure in Pa. As the ablative material recesses, the cross-sectional area of the throat increases. This causes the I_{sp}, P_c, and C_f to decrease, and thus the thrust force to decrease necessitating the use of ablative materials with low erosion rates to obtain the highest potential engine performance. The increase of the throat cross-sectional area decreases C_f as seen in Figure 2.4.

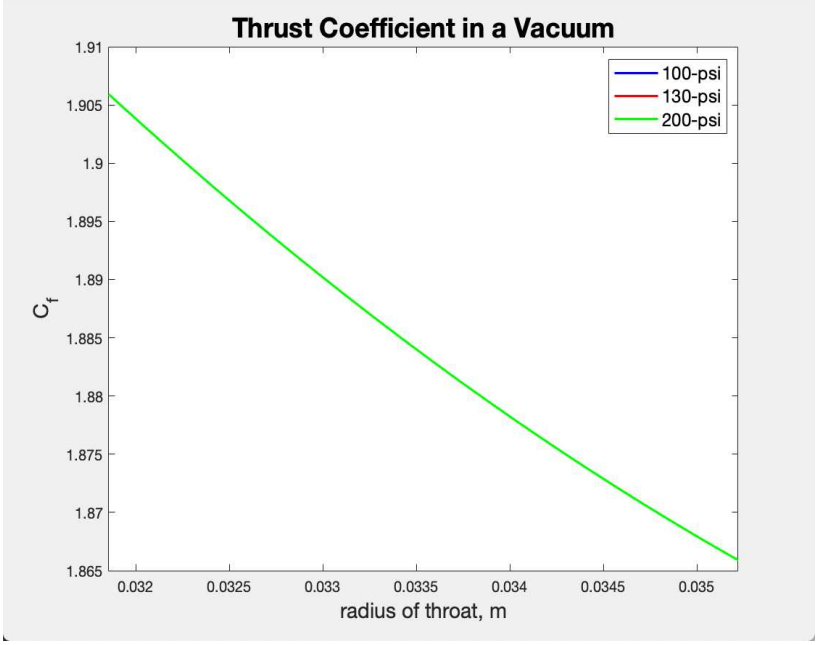

Figure 2.4: Effects of erosion on thrust coefficient

Notably, the thrust coefficient was the same for all chamber pressures due to the change in exit velocity, pressure ratio, and area ratio changing at the same rates with respect to chamber pressure. In addition to the thrust coefficient decreasing as the throat area increases, the chamber pressure also decreases with the erosion of the ablative material, as seen in Figure 2.5.

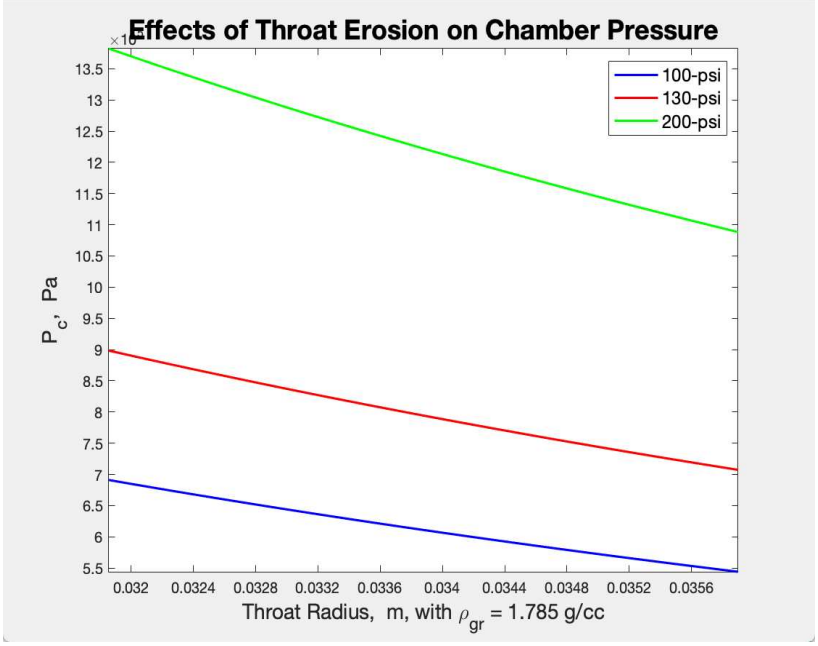

Figure 2.5: Effects of erosion on chamber pressure

The chamber pressure plotted was calculated assuming a constant C^* and $\dot{m}$ using the equation:

$$P_c = \frac{\dot{m}C^*}{A_t} \tag{2.8}$$

If the chamber pressure were to be kept constant as the throat area increased with a throttle valve and either a constant pressure tank or turbo pump system, the performance of the engine would still decline as the supersonic area ratio decreased because the specific impulse decreases with increased throat area. The proposed rocket engine intends to self pressurize with an approximately constant $\dot{m}$; therefore, the specific impulse would decrease more rapidly. Utilizing the equation:

$$I_{sp} = \frac{C^* C_f}{g_o} \tag{2.9}$$

the specific impulse was calculated as a function of throat radius. This equation assumes that C^* is constant, which is a valid assumption since C^* is a weak function of chamber pressure. Figure 2.6 depicts the reduction in specific impulse, which is analogous to miles per gallon, as the throat area increases.

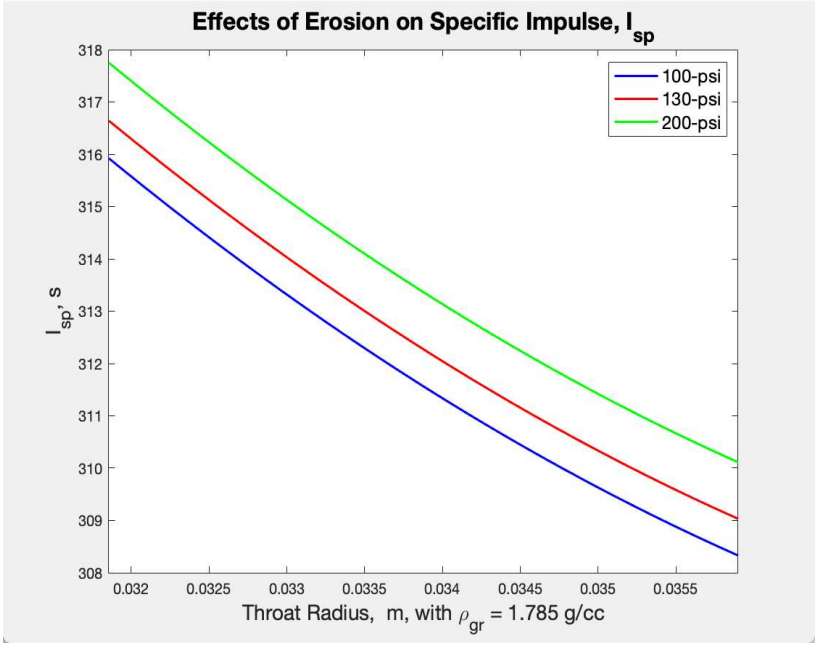

Figure 2.6: Effects of erosion on specific impulse

The decrease in all of these critical parameters cause the thrust force of the rocket engine to decrease as the ablative material recesses. The adverse effects on performance is less evident with liquid fuel than solid rocket fuel engines. Figure 2.7 shows the adverse effects of material erosion at the throat on the thrust of the engine for the three mass flow rates associated with 100-psi, 130-psi, and 200-psi chamber pressures.

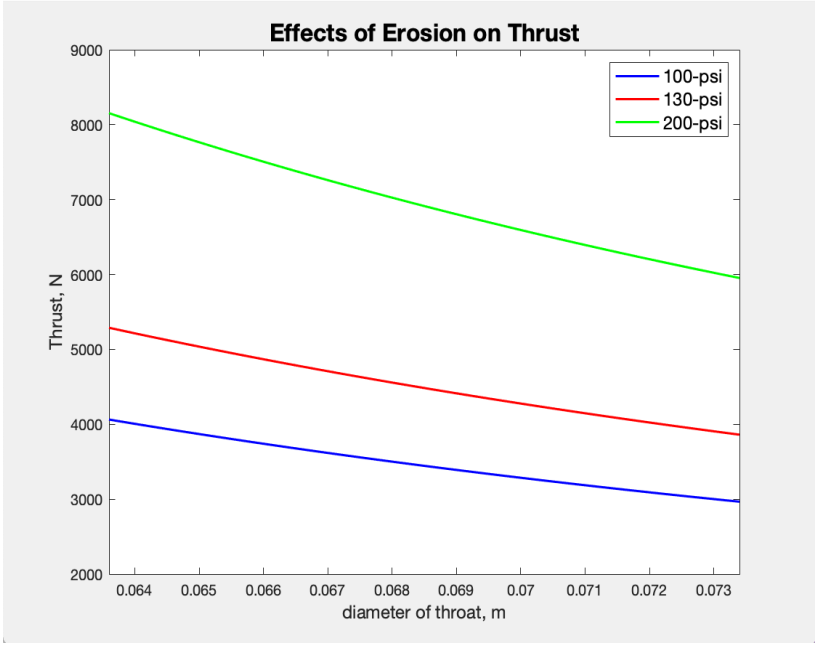

Figure 2.7: Effects of erosion on thrust at various chamber pressures

Balancing thrust, I_{sp}, and C^* with erosion rates and mass ratios of ablative cooling has been a challenge that rocket designers have faced for decades. Determining the best material to withstand both the chemical and mechanical erosion incited by the hostile conditions inherent to rocket nozzles is essential for maintaining optimally efficient propulsion. Fortunately, there has been a substantial amount of research published which explicates these relationships, including empirically derived functions for calculating erosion rates.

2.1.2 Literature Survey of Ablative Cooling

The surveyed literature focused primarily on solid rocket propellants with chamber pressures ranging from 1000-psi to greater than 2000-psi, typically an order of magnitude higher than proposed in this investigation. Research performed by Klager has shown that the recession of non-pyrolyzing inserts in rocket nozzles is predominantly caused by chemical processes [4]. Furthermore, Kuo and Keswani developed a method for modeling the recession of carbon/carbon nozzles [5]. These findings consistently showed that both the diffusion rate of oxidizing species across

the boundary layer to the surface and pressure are the largest contributing factors to erosion rates of non-pyrolyzing materials.

Density is proportional to pressure; therefore, the increased pressure causes a larger concentration of oxidizing species to be present within the volume. Higher chamber pressure also leads to higher combustion temperatures. The increased kinetics due to higher temperatures result in larger concentration gradients and thus higher diffusion rates of oxidizing species across the boundary layer to the surface [6]. The higher diffusion rate of oxidizing species increases surface erosion; however, because recession rates are linearly proportional to chamber pressure, comparable erosion rates can be extrapolated from the experimental data. Therefore, the pressure differences were accounted for by dividing the erosion rates for each material found in the literature by a linear scaling factor. Table 2.1 lists recession rates for four of the most commonly used ablative materials.

Table 2.1: Erosion rates for ablative materials

	Erosion Range, mm/s	**Tested Pressure,** MPa	**Adjusted Erosion Range,** mm/s	**Thermal Conductivity,** W/m^2K
Carbon-Phenolic [7]	$0.015-0.02$	0.689	$0.015-0.02$	1.43/14.27 Virgin/ Char [8]
Carbon-Carbon [6]	$0.246-0.335$	$4.73-4.86$	$0.035-0.049$	22.49/7.3 Parallel/ Normal [9]
Graphite [10]	$0.033-0.035$	6.89	$0.0032-0.0034$	63.81001[11]
Pyrolytic Graphite [12]	$0.03-0.05$	0.689	$0.03-0.05$	1.71001[12]

Experimental findings by Bianchi et al. involving carbon-carbon nozzle inserts and carbon-phenolic lining in the bell of two different rocket nozzles show that the erosion rates are highest near the throat. Recession of the ablative material at the throat contributes substantially to the reduced efficiency of the rocket engine with burn time [13].

2.2 Regenerative Cooling

Regenerative cooling has been successfully employed for decades on countless well-known rocket engines. The pioneering of regenerative cooling allowed material stability to be maintained over longer burn durations. Regenerative cooling incorporates the flow of pressurized propellants either in an annulus or in channels on the exterior surface of the rocket nozzle. Flowing liquid along the outside surface of the nozzle wall acts as a heat exchanger by absorbing thermal energy from the combustion gas through convection. In the process the fuel is preheated, which resembles a regenerative heating cycle, hence the name.

In contrast to the reduced engine performance with time associated with material erosion in ablative cooling methods, regenerative cooling increases combustion efficiency by preheating the propellant and thus increasing enthalpy. Research done by Pizzarelli has shown that the preheating of the fuel by absorption of thermal energy increases the exhaust velocity by approximately 1.5%. This sounds nominal; however, at the characteristic high exhaust velocities found in rocket nozzles, it can be quite advantageous [14].

Liquid rocket engines offer the merit of utilizing the fuel as a coolant; although, liquid fuels have a narrow single-phase temperature differential. The throat of the nozzle sustains the most intense heat transfer rates, and thus mandates robust heat mitigation; however, the throat is least suitable for ablative cooling due to the effects of erosion rates on engine performance. Exploiting the benefits of regenerative cooling near the throat offers critical heat removal without performance reduction. Despite the increase of thrust to weight ratio due to the inherent design complications, regenerative cooling is widely viewed as a superior cooling option; therefore, an array of regenerative cooling designs were investigated.

Literature Survey of Regenerative Cooling

The effects of channel geometry, especially aspect ratio, have been well documented in peer-reviewed literature. It has been determined that high aspect ratios in rectangular channels offer superior heat absorption. Research by NASA has found that high aspect ratio rectangular channels can increase cooling capabilities by more than 30% due to thermal stratification, while only

increasing the pressure drop through the channels by approximately 2% due to adverse flow behavior. The adverse flow conditions are caused by the increased surface area in rectangular channels, which creates more boundary layer effects and possible flow stagnation in the corners [15].

Research done by Pizzarelli et al. at the Sapienza University of Rome determined there is an optimal aspect ratio often for the most substantial heat transfer away from the engine wall. Once the aspect ratio increases beyond ten, the thermal stratification becomes excessive and reduces cooling efficiency [16]. Additionally, if high-aspect-ratio channels are used, the solid material between the cooling channels behaves like cooling fins by transferring heat from the engine to the atmosphere through conduction in parallel with the convective cooling. The literature review showed that for analytical calculations of heat transfer with regenerative cooling, simplifications are often utilized, such as thin wall assumptions and annular flow calculations. Annular flow and thin wall calculations allow the conduction from the combustion gases through the walls between the channels to be ignored, making the analytical calculations much more feasible [14].

There are numerous peer-reviewed journal papers published with findings regarding the regenerative cooling effects of a diversity of liquid fuels in various geometrical configurations; however, of the research surveyed, there were none found that investigated the use of both the fuel and oxidizer as coolants. Naraghi et al. in 2006 explored a method of regenerative cooling referred to as dual regenerative cooling circuits. In contrast to the dual-channel design examined for this research, their design for dual regenerative cooling used either the fuel or the coolant injected into channels at the throat with one circuit of channels flowing counter to the combustion gas, and the other circuit of channels flowing parallel to the combustion gas, as seen in Figure 2.8.

This method offered increased cooling benefit due to the coolant being at its lowest temperature in the region of the highest heat flux. The disadvantage was that the downstream portion of the coolant was typically dumped, which was not only wasteful but also increased the ratio of weight to thrust for the engine. The only proposed method to avoid dumping the downstream portion of the coolant was to incorporate an additional injection manifold, which would have added further complication, weight, and cost [17].

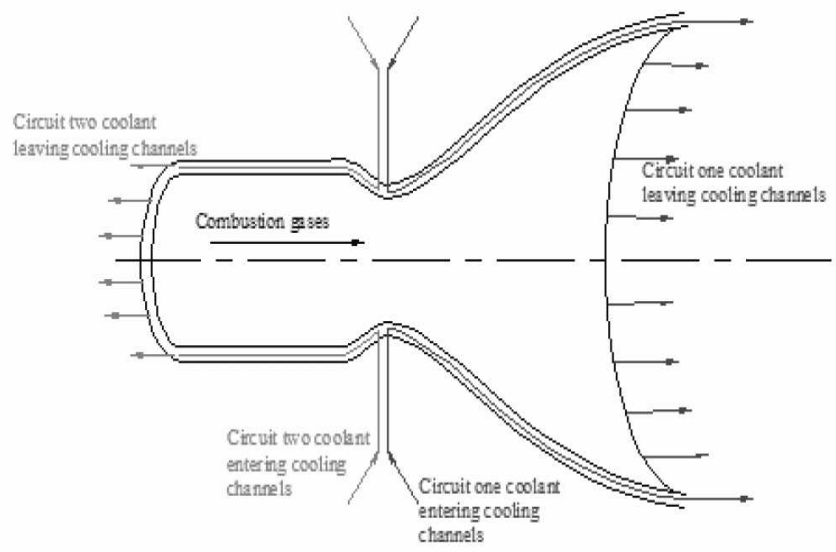

Figure 2.8: Dual regenerative circuits
[17]

Although considerable research has been published regarding regenerative cooling, at the time of this research there seemed to have been a lack of investigation into the advantage of using both the fuel and the oxidizer in separate sets of channels as coolants. For the proposed engine, the mass flow rates of oxidizers were substantially higher than the fuel mass flow rates. This allowed for more heat transfer capability from the oxidizer; however, the concern of corrosion due to oxidation could be a concern. For rocket engines, long burn times are typically in the range of minutes, which is a relatively short time scale when considering the potential of fouling the channels. Determining whether the benefit would be adequate to warrant the risk was evaluated for this thesis using both analytical modeling with MATLAB and numerical modeling with FEA-CFD software.

Chapter 3

Combustion Analysis

The application of high-performance, yet stable and inexpensive propellant, have the potential to attenuate the financial and environmental impacts of rocket fuel combustion. Ethane, ethylene, and nitrous oxide have relatively non-toxic, non-corrosive, and stable characteristics, which allow much of the rigorous transportation safety requirements for typical rocket fuels to be circumvented. For this research, the combustion behavior was investigated for a range of liquid ethane to ethylene ratios as well as oxidizer to fuel, O/F, ratios to determine the optimum specifications for the proposed rocket engine. The executable version of the NASA CEA, chemical equilibrium with applications, and Chemkin software were chosen to solve the conservation equations for both transient and steady states.

The thermophysical properties for the combustion gas were calculated using NASA CEA code at focal subsonic and supersonic area ratios, the combustion chamber, and the throat of the rocket engine for each pressure, and O/F mass ratio requested in the input file. The values were then used to develop functions in MATLAB for each thermophysical property with respect to axial position. For the analytical models, MATLAB was selected to iteratively calculate the heat transfer rates ($\dot{Q}$), surface temperatures, and erosion rates given various parameters, such as O/F ratio, ablative material, and wall thickness to determine the ideal cooling design specifications. The combination of NASA CEA and MATLAB provided and Chemkin validated the accuracy of crucial boundary condition values that were later utilized for the CFD simulations. For the numerical models, ANSYS Fluent was chosen as the CFD software to simulate fluid dynamics and heat transfer due to its accurate predictions within reasonable time frames.

Stoichiometric combustion is defined as the precise fuel to air ratio for complete combustion. Equivalence ratio (ϕ) is the actual fuel to air ratio to the stoichiometric fuel to air ratio. An equivalence ratio, ϕ, of one is indicative of stoichiometric combustion, ϕ less than one is a fuel-lean mixture, and ϕ greater than one represents a fuel-rich mixture. Balancing a chemical equation

computes the moles of each reactant and product species for a stoichiometric reaction, and offers a reference frame for analyzing the combustion behavior. Gas compositions are generally given in moles since mole fractions do not change with temperature or pressure. The conversion from mass ratio to a mole ratio is given by:

$$\left(\frac{F}{O}\right)_{mol} = \left(\frac{MW_{O_x}}{MW_F}\right)\left(\frac{F}{O}\right)_{mass} \tag{3.1}$$

Mixing ethane, C_2H_6, and ethylene, C_2H_4, in a 50/50 mixture has a molecular weight of 29.0606 g/mol, and the molecular weight of N_2O is 44.0134 g/mol. Therefore, 4.621 is the O/F mole ratio of the proposed engine. At a stoichiometric ϕ for the proposed propellant, the O/F mass ratio was calculated to be 9.84; however, the target O/F mass ratio is 7 for this engine. This translates to a ϕ slightly above 1.4, which is a fuel-rich mixture. In fuel-rich mixtures, there is insufficient oxygen for complete combustion. This results in the combustion products containing unburned hydrocarbons, which dissociate into minor molecular species and dramatically complicate balancing the chemical equation [18]. Balancing fuel-rich combustion requires simultaneously solving non-linear sets of equations. Due to the nonlinearity of solving for the number of moles in the products of fuel-rich combustion, the concentration of molecular species in the products was verified using NASA CEA code [19].

The NASA CEA code calculated many important properties of the combustion gas in the rocket engine, such as the density, dynamic viscosity, thermal conductivity, constant pressure specific heat capacity, gamma, equivalence ratio, temperatures, pressures, enthalpy, internal energy, entropy, molecular weight, mass fractions of molecular species, Prandtl number, sonic velocity, Mach number, C^*, and specific impulse for each subsonic and supersonic area ratio, pressure, and O/F mass ratio requested in the input file. The mole fractions of oxidizing species in the proposed engine with respect to the O/F mass ratio are shown in Figure 3.1.

Chemkin is not specific to rocket engines but is able to calculate a wide range of combustion characteristics, including surface temperature, adiabatic flame temperature, mass density, fractions of molecular species, and volumetric heat production rate. Chemkin is capable of plotting these

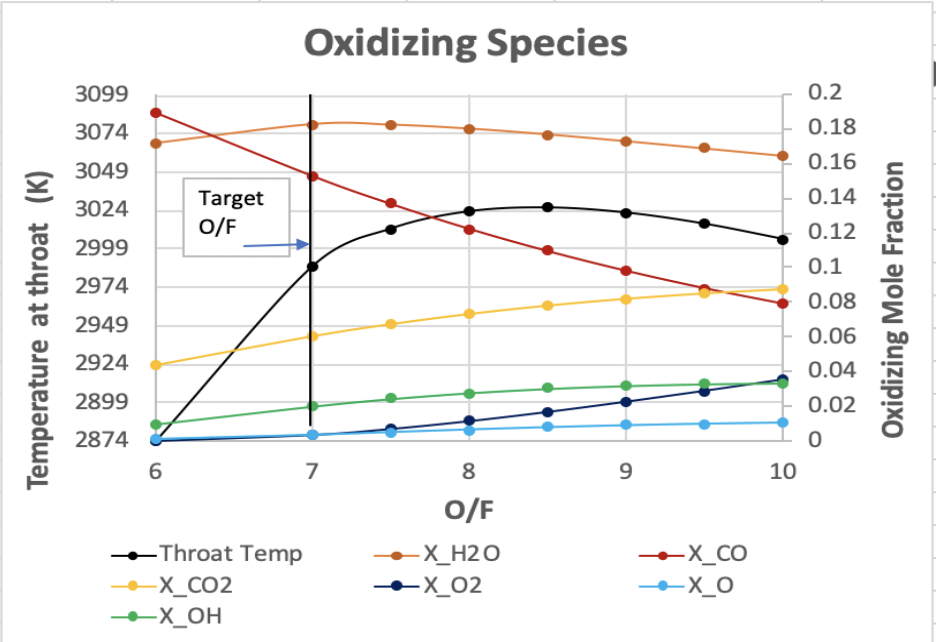

Figure 3.1: Oxidizing species with respect to O/F mass ratio

quantities with respect to a variety of properties, such as residence time, equivalence ratio, or mass flow rates [20]. The graphical representations offer the ability to investigate the combustion behavior for nearly any propellants at any equivalence ratios of interest.

In Chemkin, the chemical mechanism produced by El Bakali, et al., which includes NO_x, was used to simulate the combustion of the proposed propellants sweeping through equivalence ratios and mass flow rates to inform the most advantageous O/F mass ratio [21]. The combustion chamber was modeled as a well-stirred reactor with finite rate chemistry to determine blow-out limits and the effect of residence time on the chemical composition and temperature entering the nozzle. The proposed O/F ratio and mass flow rates were well below the blowout limit calculated with Chemkin, further validating the combustion stability of the proposed design. The blowout limit with respect to mass flow rate can be seen in Figure 3.2.

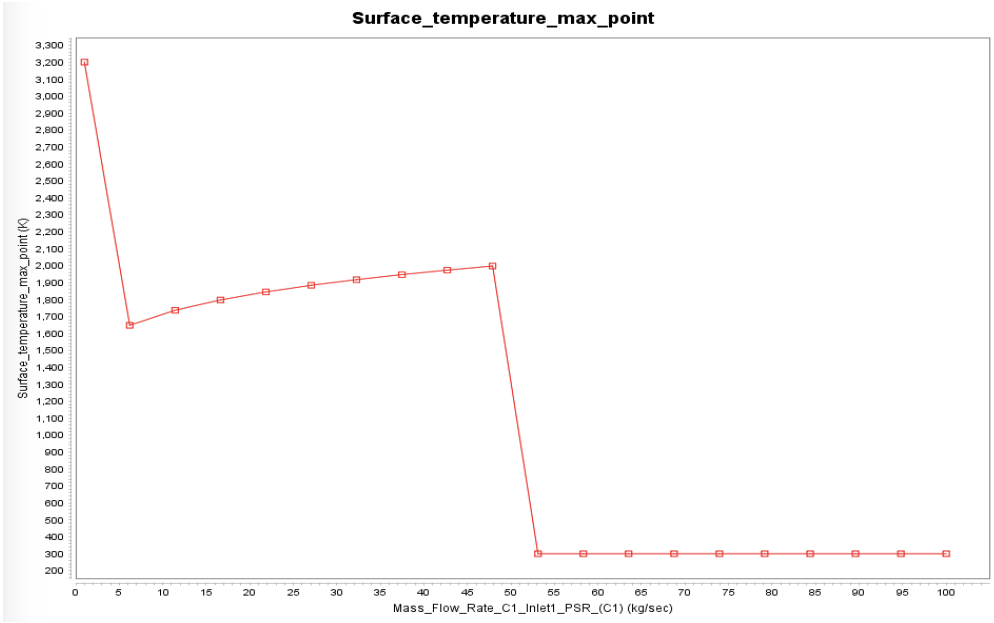

Figure 3.2: Blowout limit with respect to mass flow rate

The maximum surface temperature versus the equivalence ratio can be seen in Figure 3.3. Notably, the equivalence ratio of 1.4 has a lower combustion temperature than the leaner O/F ratios that displayed the peak power.

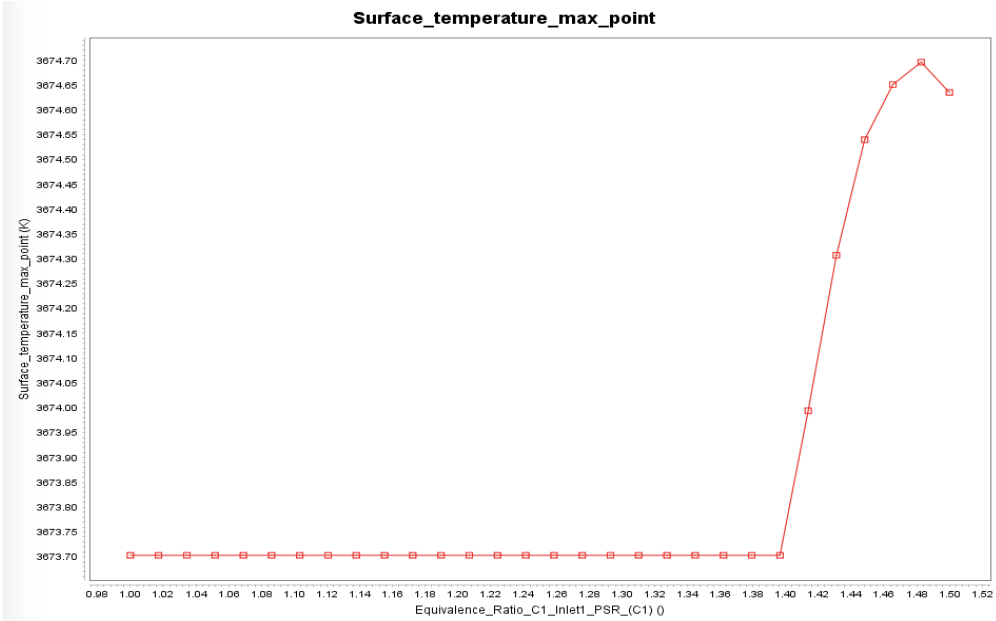

Figure 3.3: Surface temperature vs equivalence ratio

For this thesis, a range of ratios of ethane and ethylene as the liquid fuel were explored. A 50/50 mixture of ethane and ethylene exhibits the same vapor pressure curve as nitrous oxide, as shown in Figure 3.4a. This enables the propellants to be stored in common-bulkhead isothermal tanks and nitrous oxide to be used as an autogenously pressurizing oxidizer; therefore, a 50/50 blend of C_2H_4/C_2H_6 and N_2O constrained below their saturated vapor pressures were utilized for this research.

This simplified engine design reduces the weight to thrust ratio as well as the potential for mechanical failures when compared with conventional liquid rocket engines, yet also results in a powerful and efficient propellant for air-launch upper stage liquid rocket engines [22]. The calculated thrust of this engine is approximately 4000 N at the exit, and the predicted specific impulse (I_{sp}) is approximately 320 s at the target C_2H_4/C_2H_6 mixture of 50/50 and O/F mass ratio of 7:1 as seen in Figure 3.4b. These performance parameters, in addition to the previously mentioned advantages of LREs, prompted the propellant choice for this project.

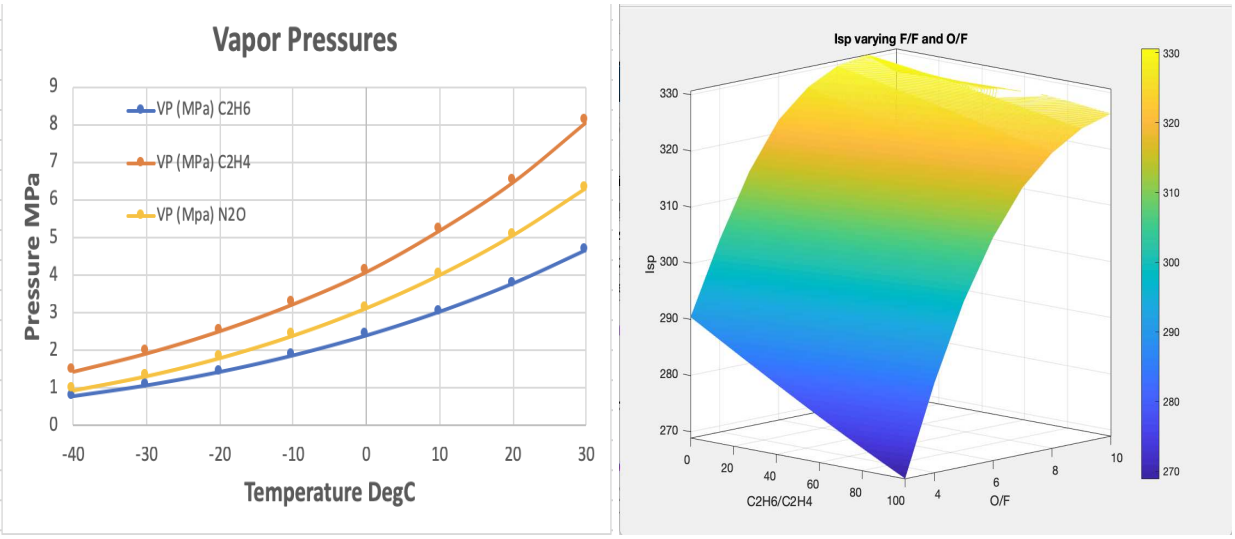

(a) Vapor pressures of C_2H_6, C_2H_4 and N_2O **(b)** Predicted ISP vs F/F and O/F

Figure 3.4: Fuel analyses

Chapter 4

Methods

Due to the impracticality of experimentally verifying the performance of each design parameter, mathematically computing outcomes save valuable time and resources and can also avoid disastrous design flaws. The employment of both analytical and numerical modeling has proven to be powerful tools for informing optimal design specifications. For the analytical model implemented in this research, a combination of NASA CEA and MATLAB were employed to calculate thermophysical properties, heat transfer rates, wall, and fluid temperatures. For the numerical method, CFD software was implemented to simulate the fluid dynamics and heat transfer within the rocket engine and cooling channels. Numerous regenerative cooling designs were investigated with both 2D and 3D analyses, including annular flow, a single-channel design with only fuel as the coolant, and a dual-channel design using both the fuel and oxidizer as coolants in separate sets of channels. Annular flow is simpler to analyze; however, cooling channels provide more effective cooling and controlled flow of the coolants.

4.0.1 Analytical Modeling Methods

In the analytical models, a quasi-2D model was used to iteratively solve for the heat transfer from the exhaust gas to the nozzle wall, ablative surfaces, and coolant channel walls, as well as the liquid coolants. The resistance method with cylindrical coordinates was used to solve for the heat transfer rates, ablative surface, engine wall, and coolant temperatures. The thermal circuit for ablative cooling was a simple series circuit; whereas, the thermal circuit implemented for the regenerative cooling model was a more complicated series/parallel resistance configuration. The surface areas, arc lengths, and local convection coefficients of the combustion gas and free convection were required for both ablative and regenerative cooling models. The surface areas of the channels and local convection coefficients of the coolants were additionally required for the regenerative cooling models. The required surface areas and arc lengths of each section were calculated

using MATLAB. The equation for the surface area integral utilized, where $z = g(x,y)$, was:

$$\iint_S f(x,y,z)\,\mathrm{d}S = \iint_D f(x,y,g(x,y))\sqrt{\left(\frac{\partial g}{\partial x}\right)^2 + \left(\frac{\partial g}{\partial y}\right)^2 + 1}\,\mathrm{d}A \tag{4.1}$$

The total heat transfer rate needed to first be calculated in order to use the thermal resistance to solve for surface temperatures. The generalized heat transfer equations for conduction, convection, steady flow, and radiation, as indicated by the subscripts, at steady-state and with no heat generation are:

$$\dot{Q}_{cond} = -k\frac{(T_1 - T_2)}{L} \tag{4.2a}$$

$$\dot{Q}_{conv} = hA_s(T_s - T_\infty) \tag{4.2b}$$

$$\dot{Q}_{sf} = \dot{m}c_p(T_{out} - T_{in}) \tag{4.2c}$$

$$\dot{Q}_{rad} = \varepsilon A_s \sigma(T_c^4 - T_{sur}^4) \tag{4.2d}$$

where $\dot{Q}$ is the heat transfer rate in W, k is the thermal conductivity in W/mK, L is the wall thickness in m, h is the convection coefficient in W/m^2K, A_s is the convective surface area in m^2, T_s is the surface temperature, T_∞ is the free-stream temperature, $\dot{m}$ is the mass flow rate in kg/s, c_p is the specific heat capacity in J/kgK, ε is a radiative property of the surface termed emissivity, σ is the Stefan Boltzmann constant $5.67 \cdot 10^{-8}$ in W/m^2K^4, T_c is the temperature of the surface, and T_{sur} is the temperature of the surroundings, with all temperatures absolute in the unit of K.

For the primary heat transfer analyses for annular cooling, the nozzle geometry was divided into six sections; uncooled chamber, cooled chamber, converging section, throat, cooled portion of the diverging section, and uncooled diverging section, with the throat being at axial position zero for all analyses, as seen in Figure 4.1a. The surface area and arc lengths were calculated for the 35° using MATLAB, as seen in Figure 4.1b with the dark red being the cooled section of the nozzle.

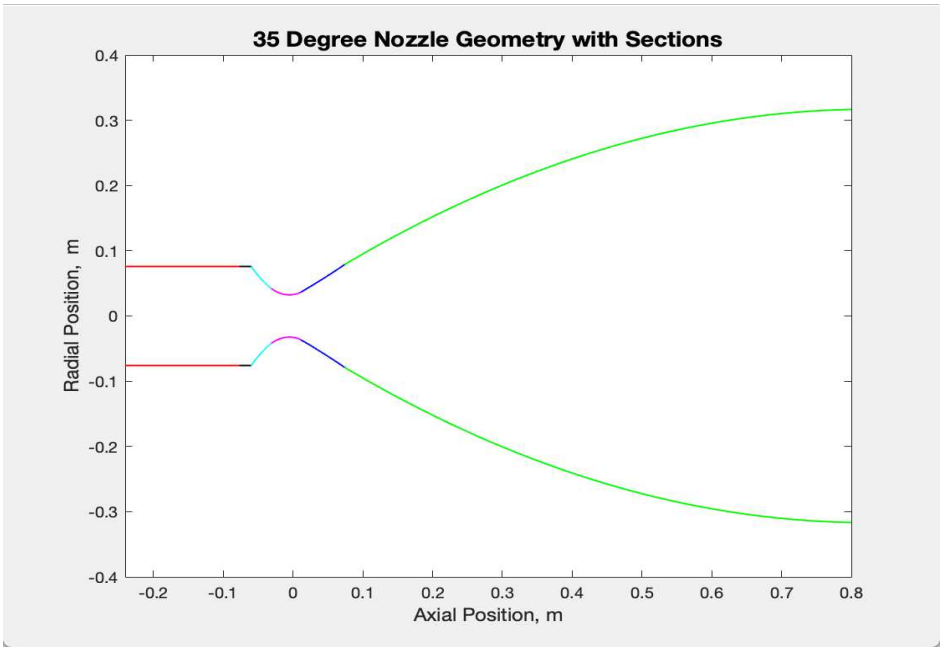

(a) 35° Nozzle Geometry with Sections

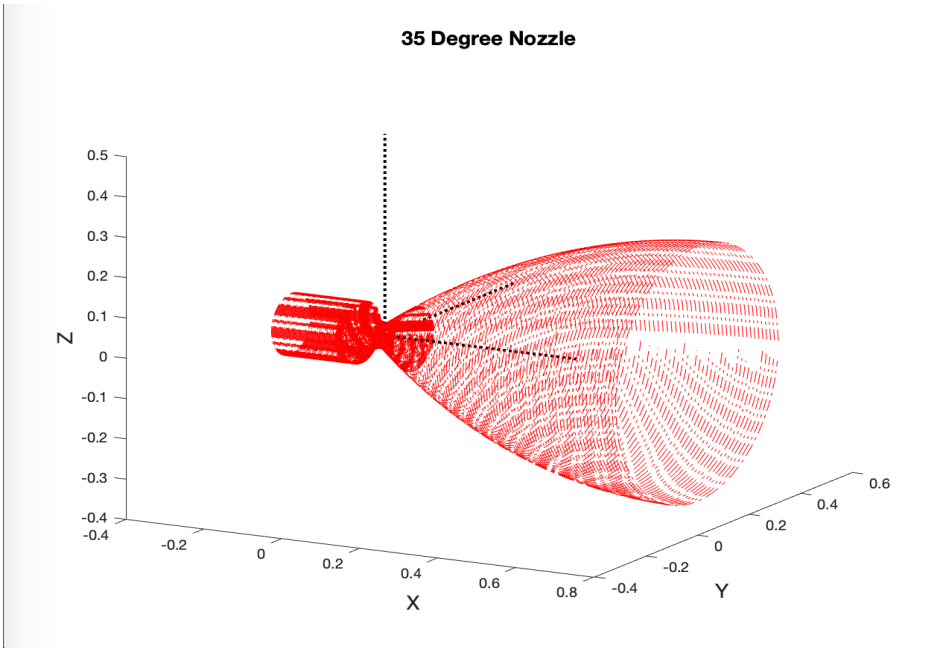

(b) Geometry for surface integrals and arc lengths

Figure 4.1: 35 Degree Nozzle Geometry

Initially, the cooled section of the nozzle extended from near the interface of the combustion chamber and the converging section through the throat to a supersonic area ratio of 3.9801. The cooled section was separated into four sections, and each of these sections was then divided into differential $\Delta x = 3.8355 \cdot 10^{-4}\ m$. The arc length of the entire engine with the combustion chamber

and bell was calculated as 1.1033 m, while 0.1657 m was the calculated arc length of the cooled section. For later analyses with cooling channels, the cooled section of the combustion chamber was eliminated to avoid a sharp turn in the channels, but the arc length of the cooled section was maintained by extending the cooled section to a supersonic area ratio of 5.9423 in the diverging section.

For the regenerative cooling models, all necessary thermophysical properties values were derived for the combustion gas, liquid C_2H_4/C_2H_6, and liquid N_2O. The properties of the combustion gas were calculated at inflection points using NASA CEA code. These data points were then utilized to create functions for the properties as a function of axial position for each of the six sections of the nozzle. The properties of liquid C_2H_4/C_2H_6 at 1000-psi, or 6.89 MPa, were provided by, NIST, the National Institute of Standards and Technology Refprop software [23]. Thermophysical properties of liquid N_2O were calculated as functions of temperature using empirical constants and equations provided by ESDU, the Engineering Sciences Data Unit [24]. The initial values established were used as the inlet boundary condition for the first node of the iterative process for the analytical model. The exit values at every Δx were then used as the inlet boundary conditions for the next node. The heat transfer from the combustion gas to the coolants was calculated iteratively from the supersonic side towards the combustion chamber due to the counter-flow configuration of the coolants.

The mass flow rates of the fuel and oxidizer were calculated for each chamber pressure of interest from the characteristic velocity values, C^*, from the NASA CEA code. The equation used to calculate the mass flow rates from the C^* was:

$$\dot{m} = \frac{P_c A_t}{C^*} \tag{4.3}$$

where $\dot{m}$ is the mass flow rate in kg/s, P_c is the chamber pressure in Pa, A_t is the cross-sectional area at the throat in m^2, and C^* in m/s. The values for C^* given by NASA CEA code were 1629.8 m/s and 1635.5 m/s for the 130-psi and 200-psi chamber pressures. Subsequently, mass flow rates of 0.22 kg/s and 0.3368 kg/s respectively were calculated.

The temperature and pressure of the inlet of the coolant chambers were specified to be 203 K and 6.89 MPa respectively. The velocities were computed for the combustion gas and coolants at all chamber pressures of interest using the mass flow rates, densities, and cross-sectional areas. Due to the fuel coolant channels being rectangular, the hydraulic diameter cross-sectional area of the C_2H_4/C_2H_6 coolant channels was applied; however, for the cylindrical N_2O channels, the actual diameter was used. The pressure drop was initially calculated through the channels for both coolants using the geometry, friction factors, and thermophysical properties and later validated by comparing the calculated values with the CFD predictions. The boiling temperatures of both C_2H_4/C_2H_6 and N_2O were computed as functions of pressure, and due to the pressure drop in the channels, a conservative temperature gradient was examined. The temperature range analyzed was divided into ΔT sections of $0.25\,K$.

The non-dimensionalized Reynolds and Prandtl numbers were then calculated for the fluid flow in the nozzle, as well as the two sets of cooling channels as functions of axial position. The Nusselt number was determined using the Gnielinski correlation for turbulent flow with a friction factor [25]. Simpler correlations are typically used for turbulent flow through a cylinder; however, due to the irregular geometry and the smaller margin of error, the more complicated Gnielinski correlation was employed [26]. The Nusselt number was then utilized to calculate local convection coefficients of the combustion gas, liquid C_2H_4/C_2H_6 coolant, and N_2O. The equation for Reynold's number is:

$$R_e = \frac{\rho v D}{\mu} \tag{4.4}$$

where ρ is the density of the fluid in kg/m^3, v is the velocity of the fluid in m/s, D is the characteristic diameter in m, and μ is the dynamic viscosity of the fluid in $Pa \cdot s$. The equation for the Prandtlnumber is:

$$Pr = \frac{c_p \mu}{k} \tag{4.5}$$

where c_p is the specific heat capacity in J/kgK, and k is the thermal conductivity of the fluid in W/mK. The dimensionless friction factor was calculated by:

$$f = \left(0.79\,ln(R_e) - 1.64\right)^{-2} \tag{4.6}$$

These values were then used to find the Nusselt number with the Gnielinski correlation:

$$Nu = \frac{\left((f/8)(Re - 1000)\,Pr\right)}{\left(1 + 12.7\,(f/8)^{\frac{1}{2}}\,(Pr^{\frac{2}{3}} - 1)\right)} \tag{4.7}$$

This correlation is valid for Prandtl and Reynold's number in the range of $0.5 < Pr < 2000$ and $3000 < Re < 5 \cdot 10^6$ [26]. The ranges of Prandtland Reynolds numbers for the combustion gas, fuel coolant, and oxidizer coolant for all chamber pressures were within this range. Therefore, the local convection coefficients in W/m^2K were calculated from the Nusselt number for every Δx using:

$$h = \frac{Nu \cdot k}{D_h} \tag{4.8}$$

where Nu is the Nusslet number, k is the thermal conductivity of the fluid in W/mK, and D_h is the hydraulic diameter in m of the cooling channels. The hydraulic diameter is calculated as $4 \cdot A_{cs}/P$, with A_{cs} being the cross-sectional area, and P being the perimeter of the channel in m. The convection coefficients of the combustion gas throughout the cooled portion of the nozzle were orders of magnitude lower than the coolants due to the much larger diameters, as well as the drastically lower density and viscosity of the combustion gas.

It was possible to calculate the local convection coefficients for the combustion gas as a function of axial position because the temperatures and thermophysical properties had been previously calculated as functions of position for each chamber pressure of interest. The temperatures of the coolants with respect to axial position is exactly the topic of interest for this thesis; therefore, the thermophysical properties, and thus the local convection coefficients of the coolants, could only be graphically represented definitively as functions of temperature. The convection coefficients of N_2O were significantly lower than C_2H_4/C_2H6 for each chamber pressure due to the much higher density and lower viscosity of N_2O. The calculated values for local convection coefficients of the

combustion gas and both liquid coolants with respect to the mass flow rates correlated with each chamber pressure are shown in Figures 4.2a and 4.2b.

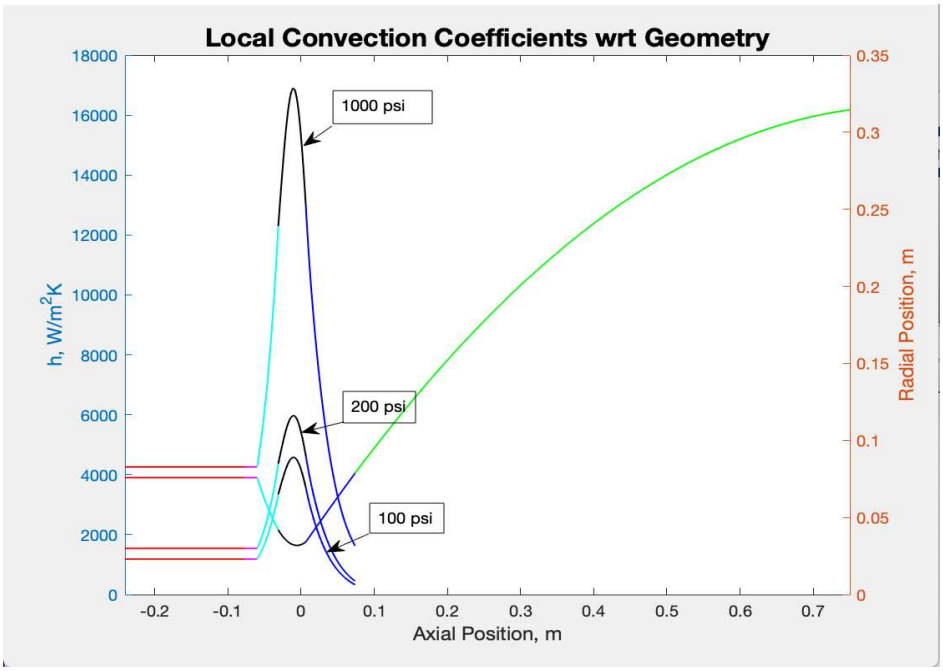

(a) Local convection coefficients of combustion gas with respect to axial position

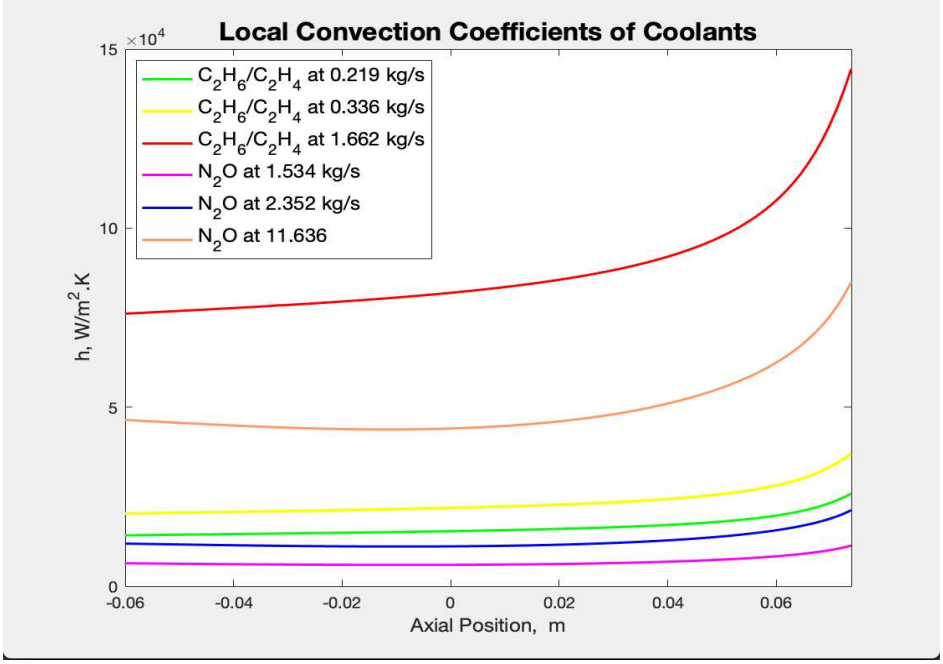

(b) Local convection coefficients of coolants with respect to temperature

Figure 4.2: Local convection coefficients for both liquid coolants at the mass flow rates correlated with each chamber pressure.

The Reynolds and Prandtl numbers and subsequent local convection coefficients for the liquid coolants were calculated using the thermophysical properties ranging from the inlet temperature of 203 K to 303 K, slightly above the boiling temperature of the fuel mixture. These data points were then used as the equivalent axial position values for the iterative solution. There is some loss of accuracy with this method; however, because there was no way to know the exact temperature at a given location, it was a necessary assumption.

The free convection coefficient on the exterior surface of the nozzle was found using tabulated thermophysical properties of air and characteristic length of the nozzle to find the nondimensional Grashof number. The Grashof number is a ratio of buoyancy forces to viscous forces in the velocity boundary layer. It is used similarly for free convection as the Reynolds number is used for forced convection [26]. The Grashof number is calculated by:

$$G_R = \frac{g_o \cdot \beta (T_s - T_\infty) L_c^3}{\nu_{air}^2} \tag{4.9}$$

where G_R is the Grashof number, g_o is gravity at sea level in m/s^s, β is the expansion coefficient with a unit of K^{-1}, T_s is the surface temperature in K, T_∞ is the free-stream temperature in K, L_c is the characteristic length of the nozzle, and ν_{air} is kinematic viscosity in m^2/s. The expansion coefficient, β, is found in a variety of ways depending on the fluid. For these calculations, the ideal gas β was utilized, which was calculated by:

$$\beta = -\frac{1}{\rho}\left(\frac{\partial \rho}{\partial T}\right)_p = \frac{1}{\rho}\frac{p}{RT^2} = \frac{1}{T} \tag{4.10}$$

For non-ideal gases, β must be obtained from tables. Given the application of external convection over a high-velocity rocket, turbulent boundary layers are to be expected. To determine whether the boundary layer needs to be treated as turbulent, the Rayleigh number is analyzed. The boundary layer is considered in transition if the Rayleigh number $\approx 10^9$. The Rayleigh number is the product of the Grashof and Prandtl numbers. In this case, the Rayleigh number was calculated as $6.03 \cdot 10^9$, which is well within the range for turbulent flow. This determines the coefficient and

exponent in the empirical correlation for external flow geometries, known as the average Nusselt number:

$$\overline{Nu_L} = \frac{\bar{h}L}{k} = C \cdot Ra_L^n \tag{4.11}$$

Subsequent to the total heat transfer rate being found, the analogous current division was calculated using the equivalent resistance of each branch. The ratio of the area of the fins between the channels and the conduction straight to the channels was calculated and utilized as area fractions in the calculations. The mass flow rate and specific heat capacity were used to calculate the liquid coolant temperatures in the channels for the subsequent nodes iteratively, where the subscript i was the index used for iteration, and Q_i was the heat flux at the i^{th} node.

$$Q_i = \dot{m} \cdot c_p(T_{i+1} - T_i) \tag{4.12}$$

Next, each hot wall temperature, as well the liquid coolant temperatures were solved iteratively for every i_{th} node using Kirchhoff's current law:

$$\sum_{k=1}^{n} I_{k_{in}} = \sum_{k=1}^{n} I_{k_{out}} \tag{4.13}$$

where I_k was the analogous current of each branch, and n was the number of analogous current branches going into the node. The cross-section at the throat of the dual-channel regenerative cooling model can be seen in Figure 4.3a. The derived parallel-series thermal resistance circuit including free convection using the calculated local free convection coefficients and radial coordinates for logarithmic conduction can be seen in Figure 4.3b.

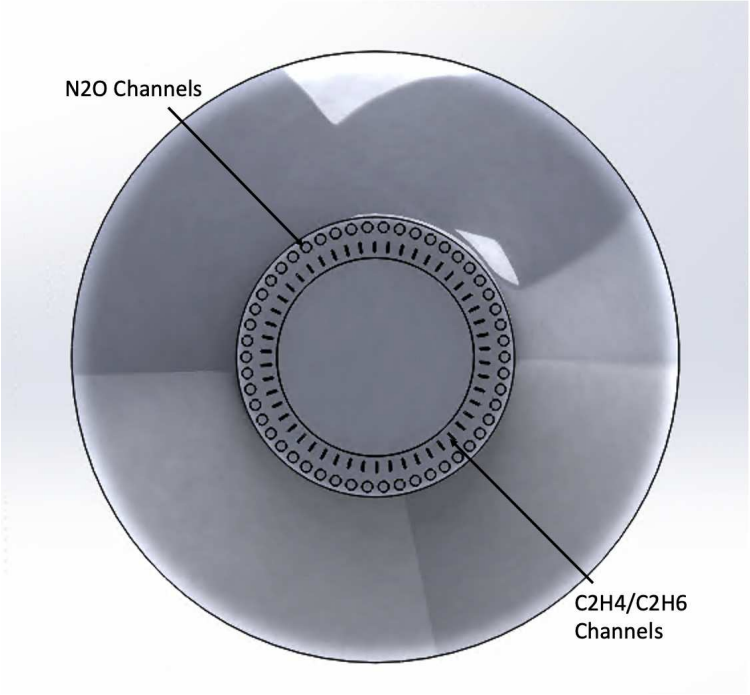

(a) Dual-channel cross-section at the throat

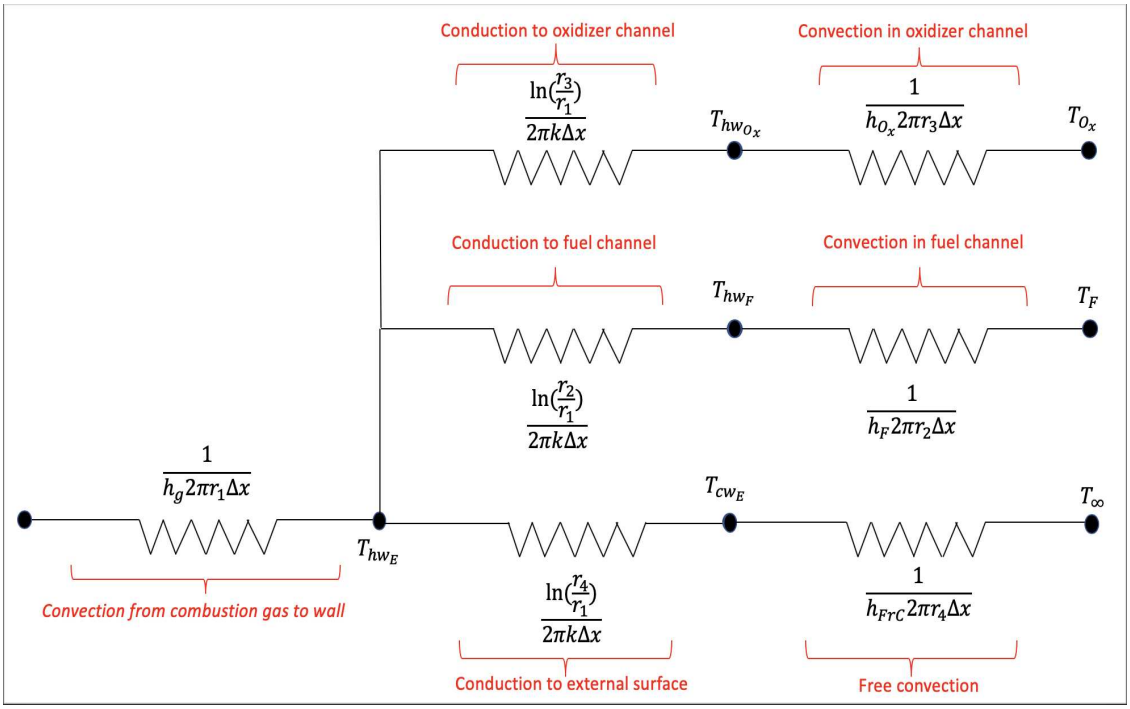

(b) Resistance circuit with free convection

Figure 4.3: Cross-section and resistance circuit with free convection

The equivalent thermal resistances employed to determine $\dot{Q}_{tot}$ were calculated first for each branch and subsequently for the complete parallel-series circuit by:

$$R_{Ox} = \frac{ln(r_3/r_1)}{2\pi k\Delta x} + \frac{1}{h_{O_x} 2\pi r_3 \Delta x} \tag{4.14a}$$

$$R_F = \frac{ln(r_2/r_1}{2\pi k\Delta x} + \frac{1}{h_F 2\pi r_2 \Delta x} \tag{4.14b}$$

$$R_{E_w} = \frac{ln(r_4/r_1}{2\pi k\Delta x} + \frac{1}{h_{fc} 2\pi r_4 \Delta x} \tag{4.14c}$$

$$R_{EQ_{tot}} = \left(\frac{1}{R_{Ox}} + \frac{1}{R_F} + \frac{1}{R_{E_w}} \right)^{-1} \tag{4.14d}$$

where k is the thermal conductivity in W/mK, h_{O_x}, h_F, and h_{fc} were the previously calculated local convection coefficients in W/m^2K for the liquid oxidizer coolant, fuel coolant, and free convection respectively, r_1, r_2, r_3, and r_4 were the radii in m from the axis to the hot wall of the engine, fuel channels, oxidizer channels and the exterior surface of the channel housing respectively.

4.0.2 Numerical Modeling with ANSYS

Numerical models of the fluid dynamics and heat transfer within the rocket engine were created using ANSYS Fluent software. ANSYS Fluent was chosen because it is a powerful simulation tool for a wide range of physics problems including finite element analysis (FEA) and computational fluid dynamics (CFD), providing accurate predictive models in a relatively short timeframe. It was determined that Fluent was a high-quality computer-aided engineering (CAE) tool for modeling the turbulent flow and heat transfer from the exhaust gas through the walls of the rocket nozzle within the required computational constraints. ANSYS Fluent has four integral software components, the Workbench, Design Modeler CAD software, ANSYS Meshing, and the solver, Fluent.

The Workbench is a graphical user interface (GUI) where the solving method is chosen, such as mechanical or fluid flow. The Workbench has twenty-three analysis systems, twenty-four component systems, and six design exploration systems to choose from in its toolbox. Workbench is also where ANSYS Design Modeler and ANSYS Meshing are accessed. The Design Modeler is internal computer-aided drafting (CAD) software; however, other CAD software designs can also be imported. Each individual part within the geometry needs to be defined to meet Fluent requirements for material domains and topography and then exported to ANSYS Meshing. Furthermore, it is advised to simplify geometry as much as possible before exporting it to the mesher. The ANSYS Meshing software discretizes the geometry domain into a finite number of control volumes, referred to in ANSYS as elements. The regions requiring mesh refinement is determined by the physics of the prototype being modeled. For example, in fluid flow, the no-slip condition occurring at the walls creates thermal and velocity boundary layers, which require mesh refinement for adequate evaluation of the gradients within the boundary layer occurring between the walls and the fully developed flow. Once a high-quality mesh is developed, it is exported to the solver, ANSYS Fluent.

Fluent allows the solution model type to be defined from an extensive list of options, including multiphase, turbulence, electrical potential, mechanical, and transport models. Fluent requires values for the thermophysical properties of materials to be input in SI units for density, specific heat capacity, and thermal conductivity for solids. For fluids, Fluent requires dynamic viscosity in addition to these properties. Fluent has a thorough internal database that can be used or defined by the user. The zones that were previously defined in Meshing are then set to the appropriate material. There are also numerous options for defining boundaries, such as velocity, pressure, or mass flow inlets and outlets. Once the boundary type has been selected, the conditions are informed by the physics of the particular model being evaluated. The reference values, methods, and controls must then be established. The parameters to monitor for convergence are designated, and the solution is initialized. After initialization has been completed, either steady or transient calculations are run for a chosen number of iterations or until convergence criteria have been satisfied. Fluent solves the Naiver-Stokes, continuity, and energy equations for each element iteratively. Fluent maintains

the user-defined inlet boundary conditions but treats the outlet boundary conditions as the initial values for the iterative solution. Furthermore, Fluent incorporates a comprehensive toolbox for post-processing [27].

Methods for Developing Numerical Models

To draw the geometry in CAD software, text files with the data points for the curves need to be imported. For this project, the text files were developed through derived functions written in MATLAB for the 35° nozzle, the channel housing, and the channels. The geometry of the housing wall and channels were created with functions to calculate the true offsets from the nozzle. The MATLAB code created text files of the points for the curves that were then converted to the format required to upload to the particular CAD software. The data points created for these lines by MATLAB were then uploaded to either Design Modeler or SolidWorks.

ANSYS Design Modeler was effective for drawing the geometry for the initial 2D and 3D models, both uncooled and regeneratively cooled with annular flow. SolidWorks was employed for the more complicated 3D single and dual-channel models. For the single and dual-channel designs, rotations, sweep cuts, circular patterns, and intersect tools were utilized to create four separate parts. The parts consisted of the nozzle, the steel housing for the channels, fifty rectangular C_2H_4/C_2H_6 channels, and fifty cylindrical N_2O channels. The parts were then assembled and uploaded to the ANSYS Workbench. From the ANSYS Workbench, the Design Modeler was used to edit the geometry to meet the required parameters for ANSYS Fluent. In Design Modeler, the channels and nozzle were defined as fluid and the housing was defined as solid, and topology was shared between all parts.

In the initial regenerative cooling model, an annulus was chosen for simplicity as Pizzarelli advised [14]. The annulus extended 0.017 m onto the combustion chamber; however, this proved challenging for the more complicated models with cooling channels. Therefore, the coolant channel housing in the single and dual-channel models terminated at the interface of the combustion chamber and converging section. The arc length of the housing was maintained by extending further into the diverging section. This design modification eliminated the abrupt turn in the small

channels, which significantly simplified the CAD drawing, as well as the ability for Fluent to converge the solutions. The more complex single and dual-channel regeneratively cooled nozzle geometries drawn in SolidWorks can be seen in Figures 4.4a and 4.4b. A solid housing model without internal cooling channels was also developed for a closer geometric comparison with the single-channel regeneratively cooled model. The solid housing design exhibited the full extent of the cooling effects of the channels.

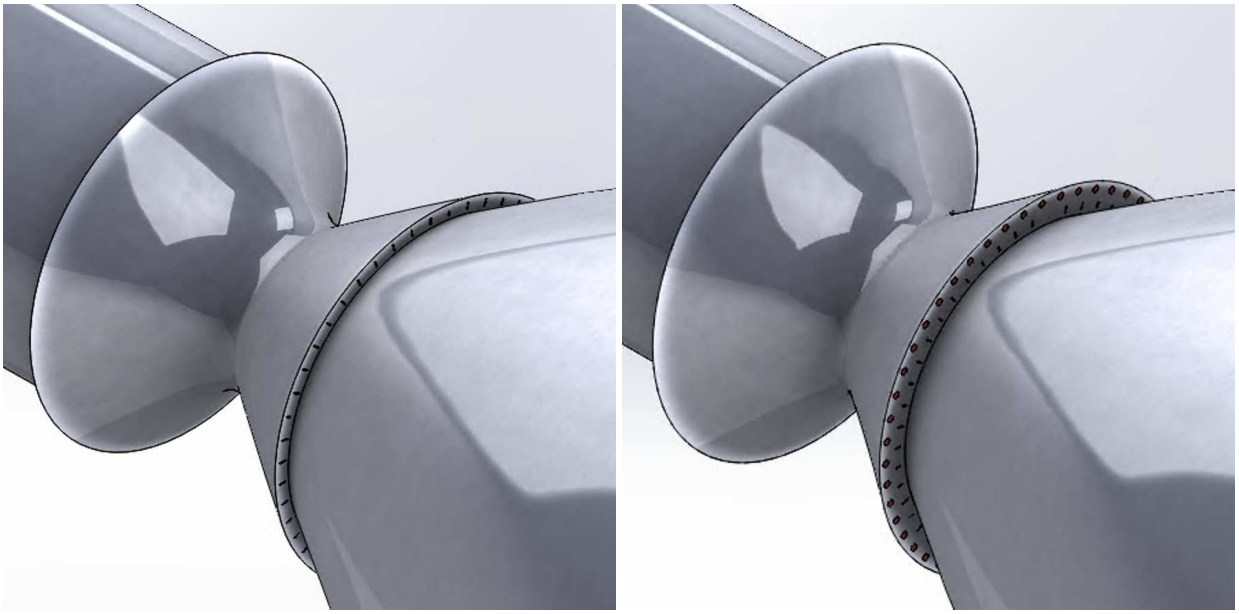

(a) Single-channel model geometry **(b)** Dual-channel model geometry

Figure 4.4: Regenerative cooling model geometry

The single-channel regeneratively cooled model was designed with a steel housing containing fifty rectangular channels. Each channel had a width of 0.5 *mm* and a height of 3.302 *mm*, yielding an aspect ratio of 6.604. The steel housing, having an arc length of 0.1657 *m* and a 0.0063 *m* thickness, was located at the throat of the nozzle where the highest heat flux and material stress was expected to occur. The coolant channels were arranged in a counter-flow configuration to the exhaust gas with the inlet to the channels at a supersonic area ratio of 5.9423 in the diverging

section. The outlets of the channels were placed at the interface of the converging section and the combustion chamber, which has a 5.6638 subsonic area ratio.

The dual-channel housing was increased in thickness from 6.3 *mm* to 12.6 *mm* to accommodate a second layer of fifty cylindrical channels, each with a diameter of 3.3 *mm*. The set of oxidizer channels was constructed in a staggered formation distal to the fuel channels. The C_2H_4/C_2H_6 channels were situated proximal to the nozzle with respect to the N_2O channels. The dual-channel model was configured with both of the coolants flowing parallel to each other (in the same direction) and counter to the nozzle flow. The 3D geometry developed in SolidWorks needed to then be imported to the workbench and edited in Design Modeler to meet Fluent specifications for shared topology between parts and to define material domains. Once the parameters for the required specifications were completely explicated for the geometry, it was exported to ANSYS Meshing.

In ANSYS Meshing, if more than one material phase is defined either a Eulerian or Lagrangian reference frame needs to be selected even if multi-phase modeling is not selected. The Eulerian reference frame considers the mesh a framework that does not interact with the fluid flowing through it. Using the Eulerian method for multiphase flow allows each phase to be solved individually. For this treatment, the phases must share the same pressure, but the momentum and continuity equations are solved for each phase. With this method, particles can be tracked, but only in the primary phase. The Eulerian method cannot solve inviscid flow, Reynolds stress turbulent models, melting nor solidification.

The Lagrangian method is used in multiphase flow with many particles as long as there is a small volume fraction in the secondary phase and particles are not indefinitely suspended. Using a Lagrangian reference frame in Ansys allows particle trajectories to be calculated. The calculations are made using force balance, including gravity, drag force, and any additional forces, such as from pressure gradients in the fluid, vorticity, thermophoretic forces, Brownian motion, and lift due to shear. Using the Lagrangian reference frame, Fluent is also able to calculate the heat and mass transfer to and from particles, droplet breakup, coalescence, turbulent effects on particles, vaporization, and soot formation. In the case of the Lagrangian reference frame, the mesh nodes

are assigned properties as though they are part of the fluid. For this project, the Lagrangian method was selected for meshing, despite the multi-phase flow solution method not being enabled.

In ANSYS Meshing, parameters for sizing and boundary conditions need to be established. The named-selections tool is used to stipulate inlets, outlets, zones, and walls such that the solver was able to identify each boundary type correctly. Fluent auto-generates arbitrary boundary conditions if sectors are not named appropriately, as well as for contact regions and walls with convection on both sides. The quality of a mesh is often attributed to low skewness, which is defined as the difference between the shape of the element and the shape of an equilateral element with an equivalent volume. According to the ANSYS Fluent user manual, a skewness value of less than 0.9 is indicative of a high-quality mesh that will provide a converged solution, given the boundaries are also specified properly [27].

Due to the high velocity and low viscosity found in the combustion gas, a thin boundary layer was assumed. The mesh was sized such that the mesh was finer in the nozzle throat and boundary layers. This minimized computational costs and time to solve iterations, yet it also ensured accurate predictions in thermal boundary layers as well as in the fully-developed flow due to the high-resolution in focal areas and lower resolution in regions which experience smaller velocity, pressure, and temperature gradients. For the 2D geometry, mesh refinement was accomplished in the boundary layers and high-gradient regions solely using edge sizing and biasing.

To institute the desired resolution in the boundary layers inside of the nozzle, annulus, and cylindrical channels in the 3D models, the manual inflation option was used with a first-layer height of 10^{-4} and a growth rate of 1.2 for 10 layers. For the rectangular channels, edge sizing was utilized with a bias factor of eight towards the walls on the four-hundred short edges of the channels. The fine mesh towards the walls offered the ability to capture the thermal and velocity gradients in the boundary layer induced by the no-slip condition. The gradients produce thermal stratification and contribute substantially to the cooling effects of the fluid.

The inlets, outlets, walls, and zones were named appropriately using the named-selection tool to ease the task of managing boundary conditions within the solver. Skewness and orthogonal quality were continually monitored for mesh quality. Once a high-quality mesh was developed and

the boundaries were defined properly, the mesh was exported to the solver, Fluent. In Fluent, the solution was calculated for a moderate number of iterations to allow Fluent to locate the regions with high gradients. Then the mesh was adapted in these regions and the solution was recalculated. This method determined that the solution was mesh independent and validated the quality of the mesh refinement in the boundary layers.

In Fluent, the pressure-based steady solver settings was selected for all models investigated. In the 2D models, the solver was set to axisymmetric; however, the option was not available in the 3D execution of Fluent, thus full 3D models were simulated. Moreover, it is safe to assume that a full 3D model is more accurate than a partial model, and in this case, precision is of the utmost importance. For all simulations, the energy equation was enabled and a realizable $k-\varepsilon$ turbulence model was deployed for turbulent kinetic energy. ANSYS documentation states that the realizable $k-\varepsilon$ model has more accurate predictions for complex geometries and strong pressure gradients [27]. ANSYS Fluent solved the equations for conservation of mass and momentum, as well as equations for turbulent kinetic energy and dissipation. The equations that ANSYS Fluent solved for k was:

$$\frac{\partial \rho k}{\partial t} + \frac{\partial (\rho k u_i)}{\partial x_i} = \frac{\partial}{\partial x_j}\left[\frac{\mu_t}{\sigma_k}\frac{\partial k}{\partial x_j}\right] + 2\mu_t E_{ij} E_{ij} - \rho\varepsilon \tag{4.15}$$

and for dissipation, ε the equation was:

$$\frac{\partial \rho \varepsilon}{\partial t} + \frac{\partial (\rho \varepsilon u_i)}{\partial x_i} = \frac{\partial}{\partial x_j}\left[\frac{\mu_t}{\sigma_\varepsilon}\frac{\partial \varepsilon}{\partial x_j}\right] + C_{1\varepsilon}\frac{\varepsilon}{k}2\mu_t E_{ij} E_{ij} - C_{2\varepsilon}\rho\frac{\varepsilon^2}{k} \tag{4.16}$$

where u_i is directional velocity component, E_{ij} is the component deformation rate, μt is eddy viscosity, and σ_k, σ_ε, $C_{1\varepsilon}$, and $C_{2\varepsilon}$ are empirically derived constants for turbulent flow [27]. Eddy viscosity was given as:

$$\mu_t = \rho C_\mu \frac{k^2}{\varepsilon} \tag{4.17}$$

The previously calculated thermophysical properties of the fluids were set in the material section of the outline tree. The material of the housing was defined as steel and the internal Fluent

database values for density, specific heat capacity, and thermal conductivity were maintained. The materials for the channels and the nozzle were defined appropriately under the cell zone conditions section of the outline tree. The coolant inlets were designated as mass flow inlets under boundary conditions, with a pressure of 1000-psi, or 6.895 MPa and temperature of 203 K. The coolant channel outlets were classified as pressure outlets and the pressure were quantified using the calculated pressure drop in MATLAB. The pressure drop in the channels was calculated for each chamber pressure investigated using friction factor, density, velocity, and channel geometry. The outlet temperatures were set as the boiling temperatures of each fluid at the calculated outlet pressures. For all models, the boundary condition for the inlet of the combustion chamber was designated as a pressure inlet and was simulated for a range of chamber pressures.

Fluent requires the type of heat transfer to be defined in the boundary conditions for walls. The thermal boundary conditions for the walls were set as mixed, which in Fluent means a combination of conductive, convective, and radiative heat transfer. Fluent does not consider internal convection because the coefficients are calculated using empirical correlations as opposed to solving the Navier-Stokes equations; therefore it was necessary to set the convection coefficient value indicative of the convection on the exterior surface. The convective heat transfer coefficient was set at 7 W/m^2K as previously calculated with the MATLAB functions. The free-stream temperature was set to 233 K, heat generation was set to zero, and the external surface temperature was quantified depending on the analytically calculated wall temperatures in each region of the nozzle. The wall thickness was fixed at 1.5 mm, and the tabulated value of 0.8 for the emissivity of steel were implemented. The external surface temperature was set using the analytically calculated quantities for each region.

The reference values were computed from the channel input with appropriate areas and characteristic dimensions according to the ANSYS Fluent user manual. The surface area of all of the channels was utilized as the reference area, and the hydraulic diameter of a single ethane channel was used for the reference diameter. A pressure-velocity coupled pseudo-transient solution method was selected, and second-order spatial discretization was utilized for the pressure, density, momentum, turbulent kinetic energy, turbulent dissipation rate, and energy. A least-squares cell-based

gradient was selected and default relaxation factors were maintained. Values for the thermophysical properties, boundary conditions, and reference geometry were selected using a combination of NASA CEA, NIST RefProp, as well as the previously written functions in MATLAB. The standard initialization method was selected to be computed from the nozzle inlet, and calculations were run in both transient and steady-states. The transient step size was calculated by dividing the average element size by the average velocity. For all simulations, the conservation equations were solved iteratively until convergence standards were satisfied. To ensure convergence criteria had been met, residuals and outlet conditions were monitored and plotted.

Chapter 5

Results

The results of the ablative and regenerative cooling models are shown in this chapter. The analytical methods were solely employed for the ablative cooling; whereas, both analytical and numerical methods were utilized for regenerative cooling models. Ablative cooling proved sufficient for insulating the nozzle walls from the extreme combustion temperatures; however, recession of the material in the throat negatively affects engine performance. The results for the analytical and numerical analyses were comparable for the single and dual-channel regenerative cooling models. The single-channel design offered marginal cooling capabilities; however, the dual-channel model provided the supplementary cooling necessary.

5.0.3 Results of Analytical Model of Ablative Cooling

For the ablative cooling analytical model, the heat transfer from the combustion gas to the ablative surfaces and the subsurface engine wall was calculated to find surface temperatures using the resistance method. The surface temperatures of the thermal protective lining and engine wall were calculated using MATLAB for a variety of ablative materials at 100-psi, 130-psi, and 200-psi combustion chamber pressures. The calculations implemented the thermal conductivity values from Table 2.1 and assumed that the ratio of pyrolyzing material to non-pyrolyzing material in the carbon-phenolic and pyrolyzing graphite were low enough that the surface temperature was not held constant due to a phase change. The heat transfer calculations showed that carbon-carbon, carbon-phenolic, graphite, and pyrolyzing graphite all have low enough thermal conductivity to effectively insulate the engine wall from the extreme temperatures of the combustion gas. Each of the thermal protective layers was able to sustain the subsurface nozzle wall temperatures well within the range of the material limits, validating that recession rates are the principal concern for the viability of ablative cooling. Figures 5.1a and 5.1b show the wall temperatures for the ablative materials investigated at 130-psi and 200-psi.

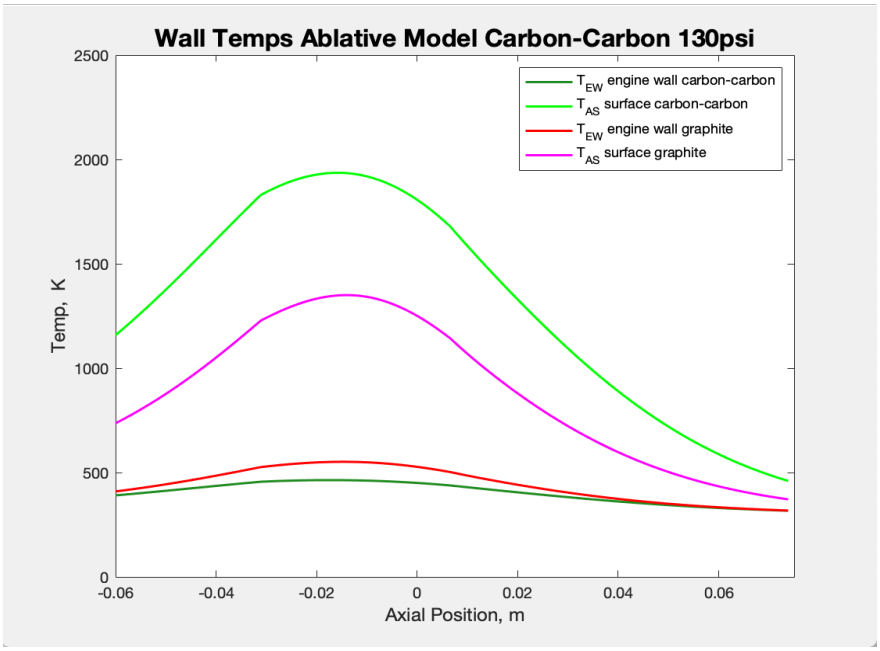

(a) Wall and ablative surface temps at 130-psi

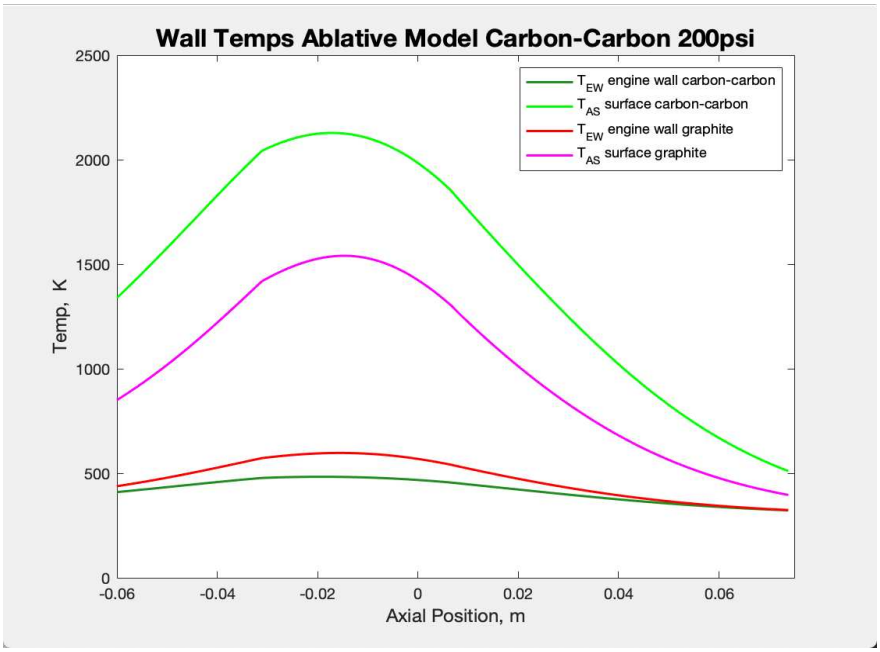

(b) Wall and ablative surface temps at 200-psi

Figure 5.1: Wall and surface temperatures for various ablative materials for 130-psi and 200-psi.

The mole fractions of O_2, O, and OH calculated using NASA CEA code were negligible for all O/F mass ratios [19]. The mole fractions of the three species with the highest concentrations for an O/F mass ratio of 7:1 were calculated with respect to the nozzle geometry, as seen in Figure

5.2. Notably, the oxidizing mole fractions are high near the throat where the heat transfer rates are highest, and the H_2O mole fractions are substantially higher than other oxidizing species.

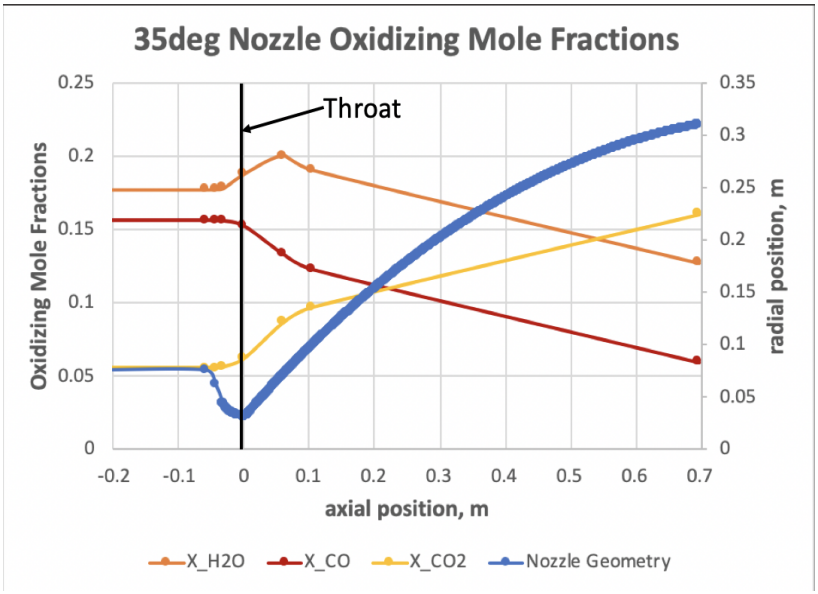

Figure 5.2: Oxidizing Species with respect to geometry

Determining recession rates is fundamental for designing a rocket engine with ablative cooling, thus calculating the mole fractions of oxidizing species in the combustion gas is required. The mole fractions of oxidizing species in the combustion products of the proposed liquid fuel with the solid fuel, 69% Ap, 12% HTPB, 19% Al, used in the research by Bianchi et al. regarding the erosion rates on carbon-carbon inserts in solid rocket engines at 1000-psi chamber pressure are compared in Table 5.1.

Table 5.1: Mole fractions at the throat of proposed liquid fuel and solid fuel used in research by Bianchi

	Temp, K	**Pressure, psi**	H_2O	CO_2	CO	OH
Ethane/Ethylene	3196	130	0.1835	0.0607	0.1835	0.0185
Solid Fuel [13]	3383	1000	0.1089	0.01049	0.2245	0.0058

The relatively high concentrations of oxidizing species found in the products of the C_2H_4/C_2H_6 fuel will contribute to a higher recession rate, but the lower chamber pressures in the proposed engine will counteract this effect. It has been concluded that chemical reactions between the oxidizing products of combustion and the nozzle wall cause chemical erosion and surface recession, especially in non-pyrolyzing materials such as graphite. Due to its low density and erosion rates, graphite is a commonly used non-pyrolyzing ablative material for lining the wall near the throat of rocket nozzles. Research conducted by P. Karthikeyan et al. provided an empirical relation that shows the erosion rate as a function of oxidizing species and graphite density [28]. The equation for the erosion rate of graphite as a function of density is:

$$Er_t = (0.5946 * (X_{H_2O} + X_{CO_2})^{1.02} * \rho_{gr}^{-1} * Pc^{0.876} * L_t^{-0.343} * r_t^{-0.076}) \tag{5.1}$$

where Er_t is erosion rate in mm/s, X_{H_2O} and X_{CO_2} are species mole fractions in the products, ρ_{gr} is the density of graphite in g/cc, P_c is chamber pressure in MPa, and L_t is the length from the injectors to the throat, and r_t is the throat radius, both in cm. Figure 5.3 shows erosion rates as a function of graphite density for 100-psi, 130-psi, and 200-psi chamber pressures.

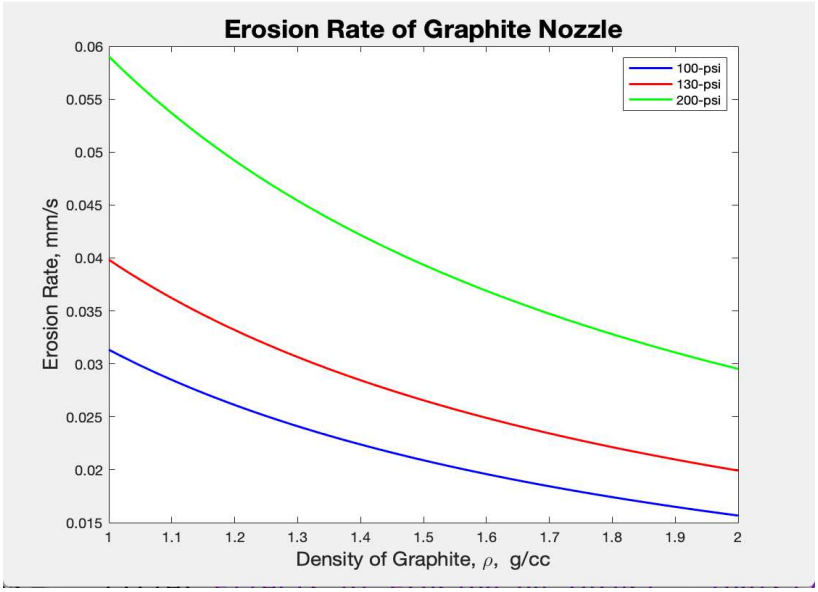

Figure 5.3: Erosion rates of graphite as a function of density and chamber pressure

Equation 5.1 presumes stoichiometric equivalence ratios, and thus does not include mole fractions of the additional oxidizing species potentially formed during the dissociation of the propellant. Nonetheless, it provides a salient tool for predicting erosion rates of a highly effective non-pyrolyzing thermal protective material. Research has consistently shown that erosion rates are linearly proportional to chamber pressure. These findings were further validated by the calculations of the recession rates of graphite for a range of chamber pressures. Excessive erosion at the throat can change the exit to throat area ratio and impact thrust, especially over a long burn duration. Figure 5.4 shows the effects of erosion on thrust with respect to time using the erosion rate for graphite with a density of 1.785 kg/m^3 to calculate the throat diameter over a burn duration of 120 seconds.

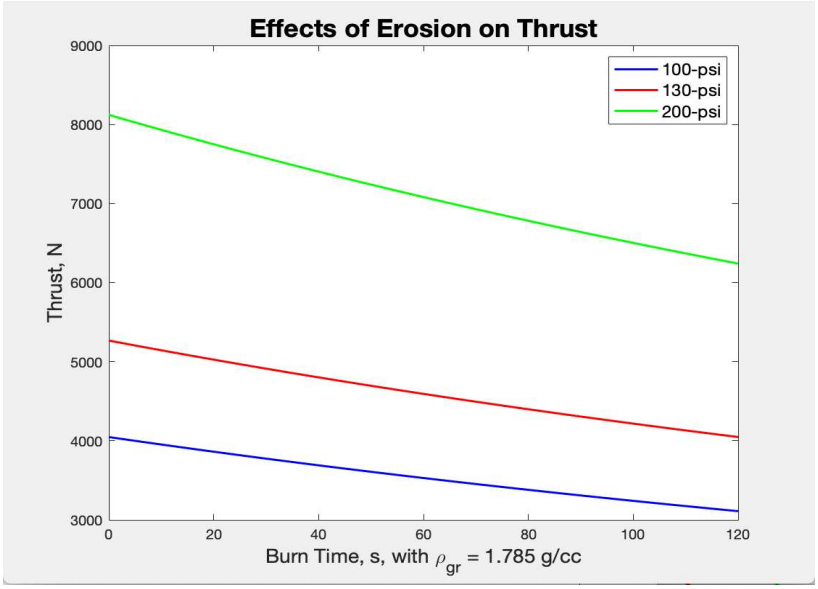

Figure 5.4: Effects of erosion on thrust force for 120 *s* burn time

The ability to predict erosion allows the design to compensate for the change in geometry on the manufacturing end. It is not uncommon to use a graphite insert at the throat in addition to the carbon-phenolic lining in the combustion chamber and bell. The best options for ablative cooling appear to be graphite and carbon-phenolic. The ratio of phenolic to carbon and the direction

of the carbon fibers greatly determine the ablation rates, which could be used for the advantage of controlling the shape of the bell with altitude. Due to the sacrificial nature of ablative materials, this cooling methodology has only been implemented in rockets designed for single-use applications. Regenerative cooling compels the concept of reusable rocket engines more immediately realizable.

5.0.4 Results of Analytical Regenerative Cooling Model

To avoid added complications to the injection design, it is imperative that the coolants remain in the liquid phase throughout the length of the cooling channels. Knowing the total heat transfer to the wall allows for the determination of whether or not the coolant has the potential to absorb enough thermal energy to keep the wall temperatures within the allowable limits of the material without undergoing a phase change.

Single-channel Model

In the analytical model, the wall temperatures remained within the thermal limits of steel; however, the fuel mixture surpassed its boiling temperature in the single-channel design in the 130-psi chamber pressure models, as seen in Figure 5.5.

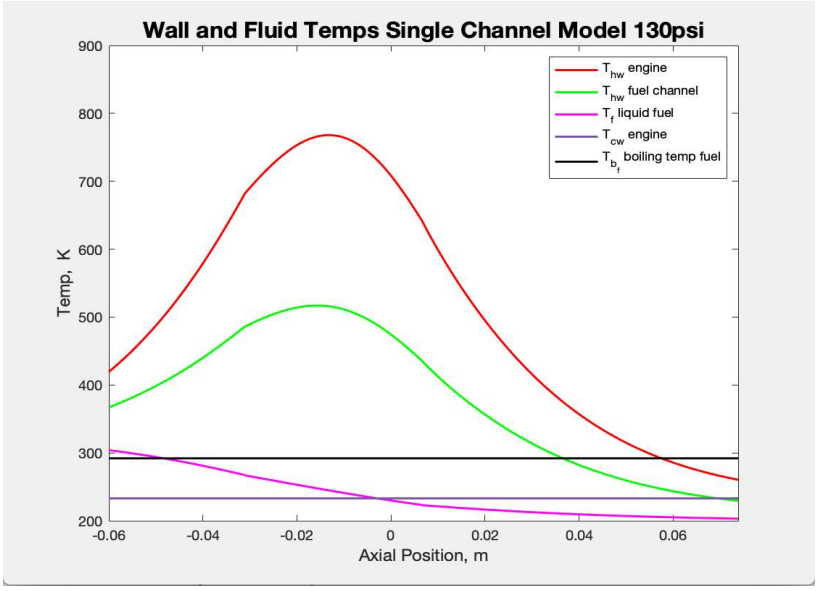

Figure 5.5: Single-channel temperatures at 130-psi chamber pressure

Boiling the coolant would greatly complicate the injection design, and therefore needs to be avoided. This motivated the investigation into the effects of marginally increasing the chamber pressure, and thus the mass flow rates of the propellant. The increased chamber pressure of 200-psi, the liquid C_2H_4/C_2H_6 remained cooler yet still surpassed the boiling temperature, further validating the challenges of employing regenerative cooling for small-scale rocket engines. The black line is at 292.5 K, the boiling temperature of C_2H_4/C_2H_6 at the given pressure. The large convection coefficients of the C_2H_4/C_2H_6 coolant offer the ability to transfer thermal energy from the engine, but the small temperature gradient is still inhibitive, as seen in Figure 5.6. Therefore, the use of both fuel and oxidizer as coolants in separate sets of channels was investigated.

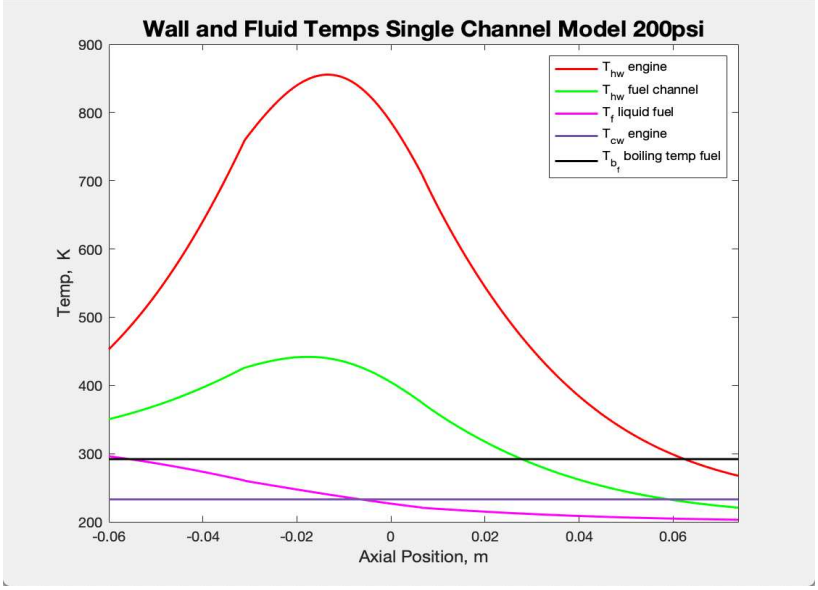

Figure 5.6: Single-channel temperatures at 200-psi chamber pressure

Dual-channel Model

Nitrous oxide has high convection coefficients, as well as substantially greater mass flow rates than the fuel, and therefore offered the ancillary thermal energy absorption needed to retain moderate temperatures in both the wall and the fluids. The analytical model showed that the addition of the liquid N_2O channels allowed the liquid fuel to remain in the liquid phase in the 130-psi cham-

ber pressure model while also maintaining wall temperatures within the thermal limits required to ensure the prolonged integrity of the steel, as seen in Figure 5.7.

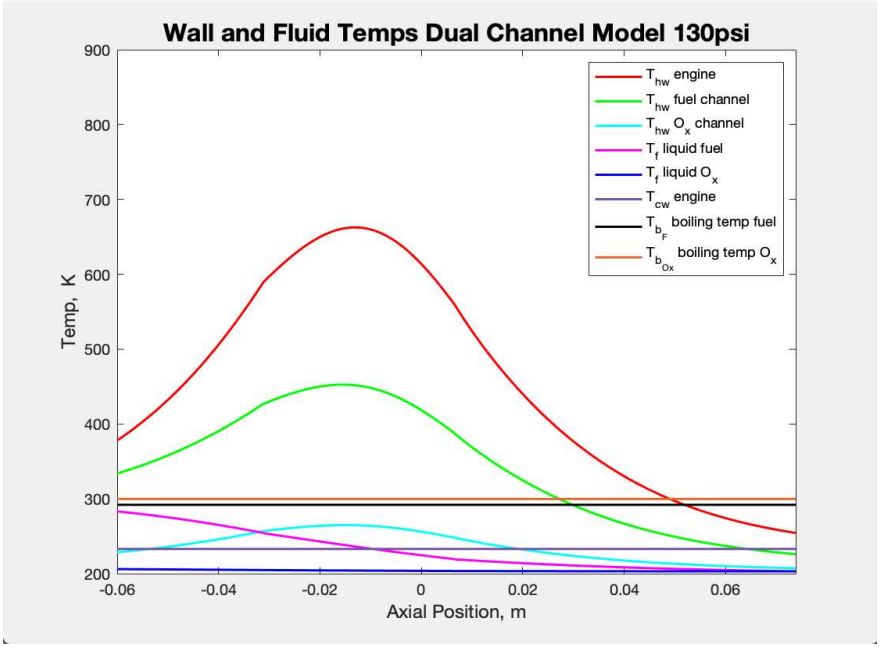

Figure 5.7: Dual-channel temperatures

The additional dark orange line in Figures 5.7 and 5.8 is at 299 K, the boiling temperature of N_2O at the calculated exit pressure of 6.8948 MPa; however, the temperature of the liquid N_2O did not exceed 208 K in the chamber pressures investigated. The exit temperature of the fuel coolant was below the boiling temperature in the 130-psi model; however, the calculations showed a narrow margin between the exit temperature and the boiling temperature. In the 200-psi model, the exit temperature of the fuel coolant remained further below the critical value depicted by the constant black line, as seen in Figure 5.8.

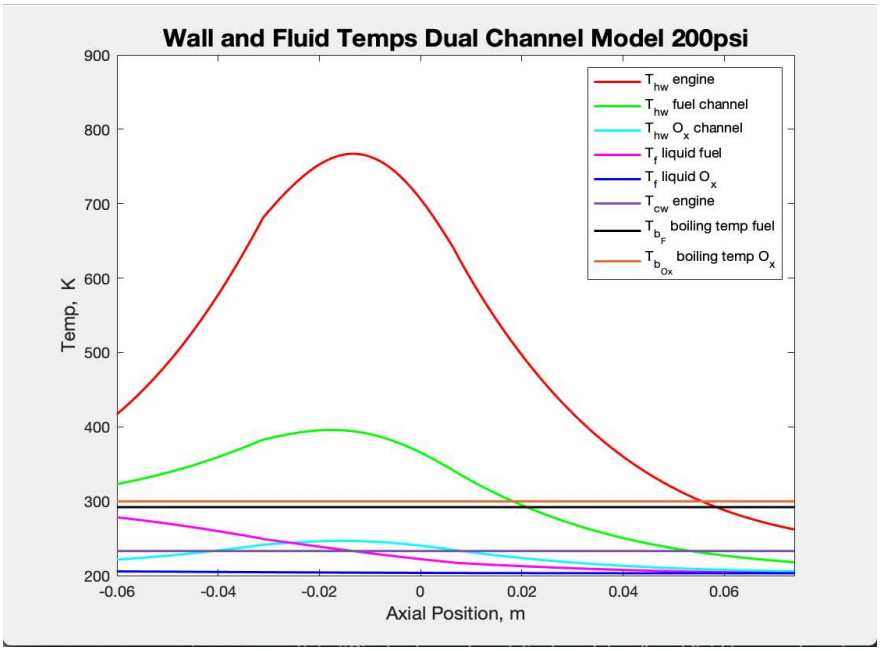

Figure 5.8: Dual Channel Temperatures

These results were compelling in favor of the dual-channel design; however, due to the margin of error and the required precision to ensure the longevity of the rocket engine, further evaluation was performed with numerical modeling. The intention was to cross-validate the results through an agreement of predictions from both methods.

5.0.5 Results of Numerical Regenerative Cooling Model

Preliminary models were created to evaluate the exhaust behavior for a variety of boundary conditions and determine the optimal parameters for the more complicated simulations. The geometry for the pilot model was created in ANSYS Design Modeler. A large plenum for the rocket to exhaust into was added to facilitate observing engine performance for a range of atmospheric pressures. Due to the high velocity and low viscosity found in the combustion gas, a thin boundary layer was assumed. The mesh was sized such that the mesh was finer in the nozzle throat and boundary layers. This minimized computational costs and time to solve iterations, yet it also ensured accurate predictions in thermal boundary layers as well as in the fully-developed flow due to the high-resolution in focal areas and lower resolution in regions which experience smaller veloc-

ity, pressure, and temperature gradients. The mesh refinement was verified by adapting the mesh for temperature and velocity gradients and ensuring the solution was mesh independent.

Uncooled Models

The proposed rocket is to be air-launched from an F-15 fighter at an altitude of 18 *km*. The atmospheric pressure was calculated as a function of altitude to be 6.556 *kPa*, using:

$$P = 101325(1 - 2.25577 \cdot 10^{-5} \cdot A)^{5.25588} \tag{5.2}$$

where P is pressure in *Pa* and A is the altitude in *m*. Subsequently, simulations were run with the plenum pressure set to 6.556 *kPa*. The outlet Mach number, velocity, temperatures, and residuals were monitored for convergence. In Fluent post-processing, Mach contours were generated for the 2D solutions. Figure 5.9 shows over-expansion of the nozzle with a plenum pressure of 6.556 *kPa*.

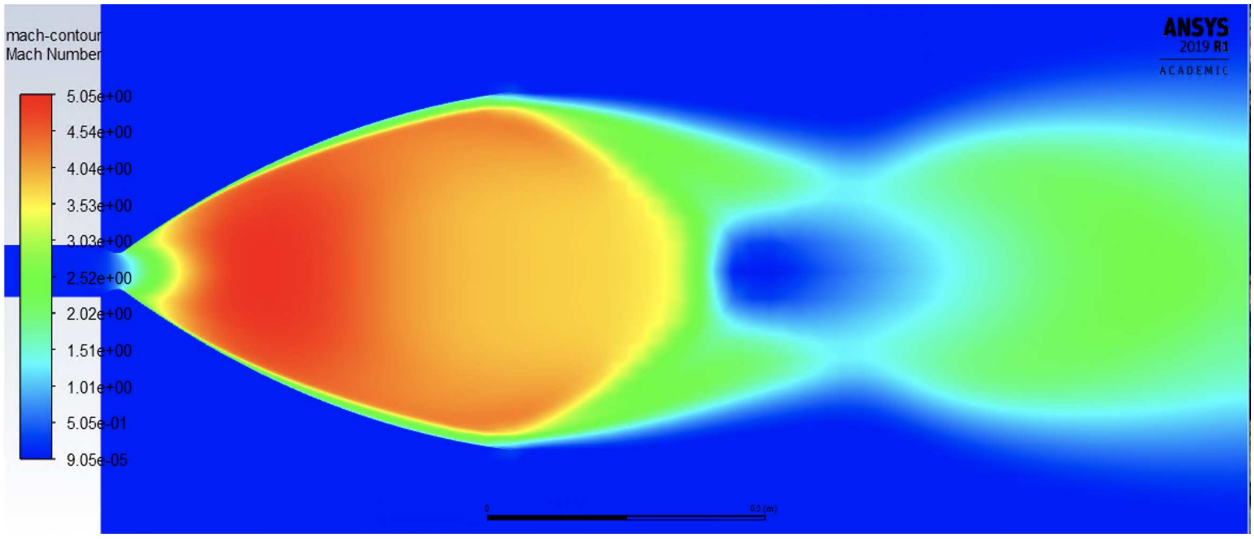

Figure 5.9: Mach contours at 6.556 *kPa* atmospheric pressure

Simulations were run for plenum pressures ranging from 101 *kPa* to 200 *Pa* and the exhaust behavior was examined. Figure 5.10 shows under-expansion at a plenum pressure of 200 *Pa* in the 35° rocket nozzle.

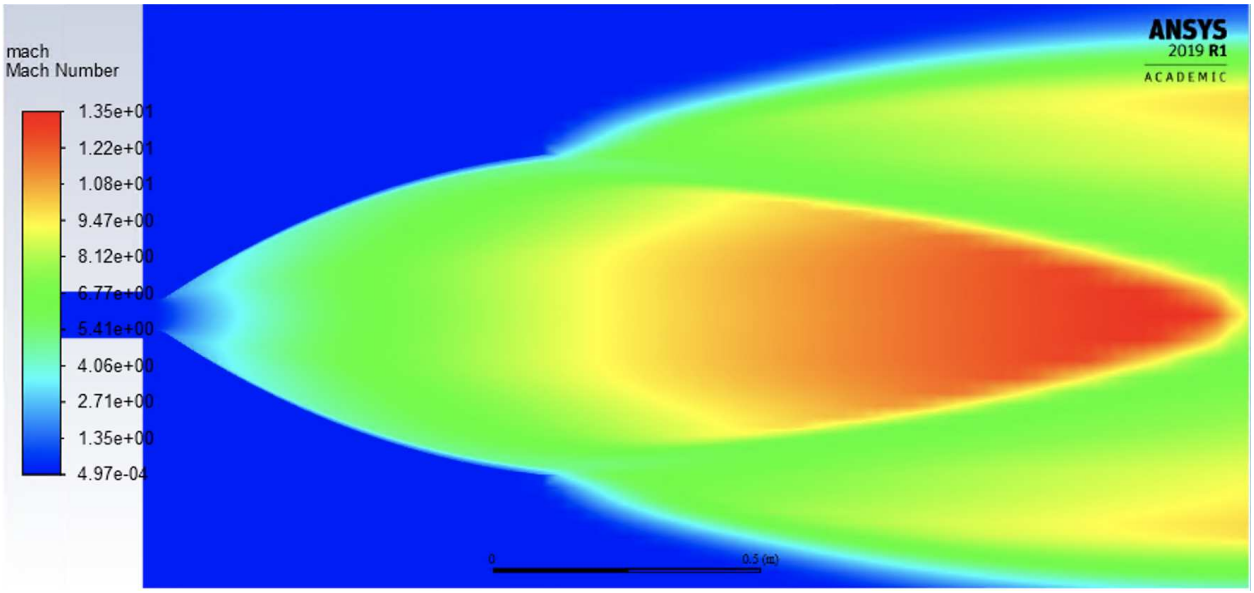

Figure 5.10: Mach contours at 200 *Pa* atmospheric pressure

The Mach numbers for both the 2D uncooled models were consistent for all plenum pressures. The area-weighted average Mach number of 4.91 at the outlet of the nozzle was calculated by Fluent compared to the Mach number of 5.2 calculated by NASA CEA code. The results for the Mach contour at the near-perfect expansion of 1 *kPa* atmospheric pressure can be seen in Figure 5.11.

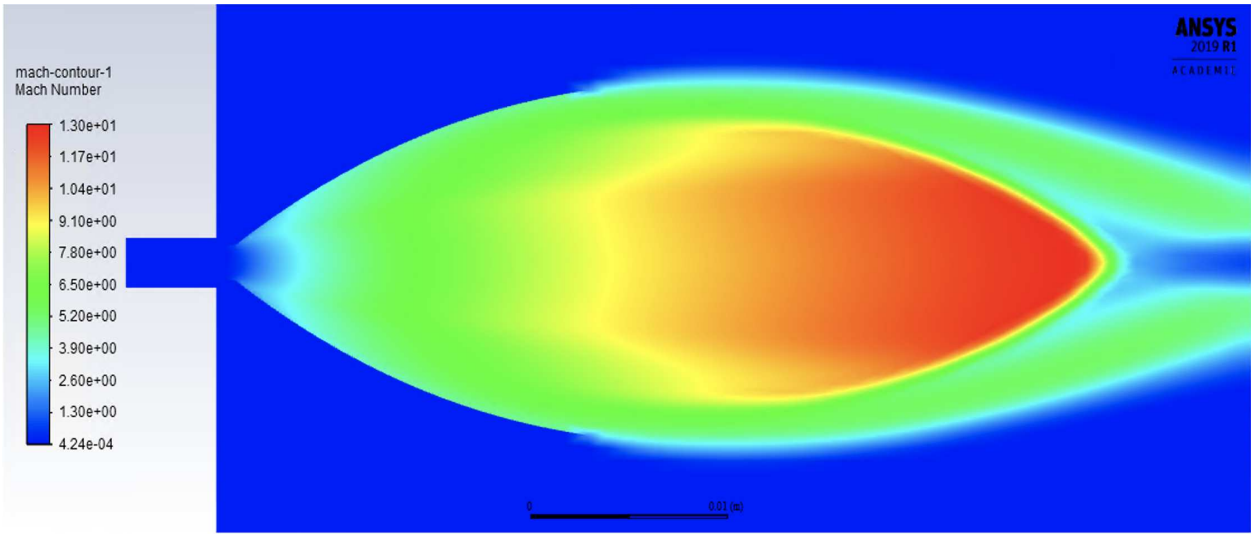

Figure 5.11: Mach contours at 1 *kPa* atmospheric pressure in the 35° nozzle

The preliminary uncooled model was duplicated in 3D to verify the consistency in predictive models and observe the exhaust gas behavior in the plenum. The Mach and temperature contours of the 3D uncooled model at 130-psi chamber pressure and a plenum pressure of 1 *kPa* can be seen in Figures 5.12a and 5.12b.

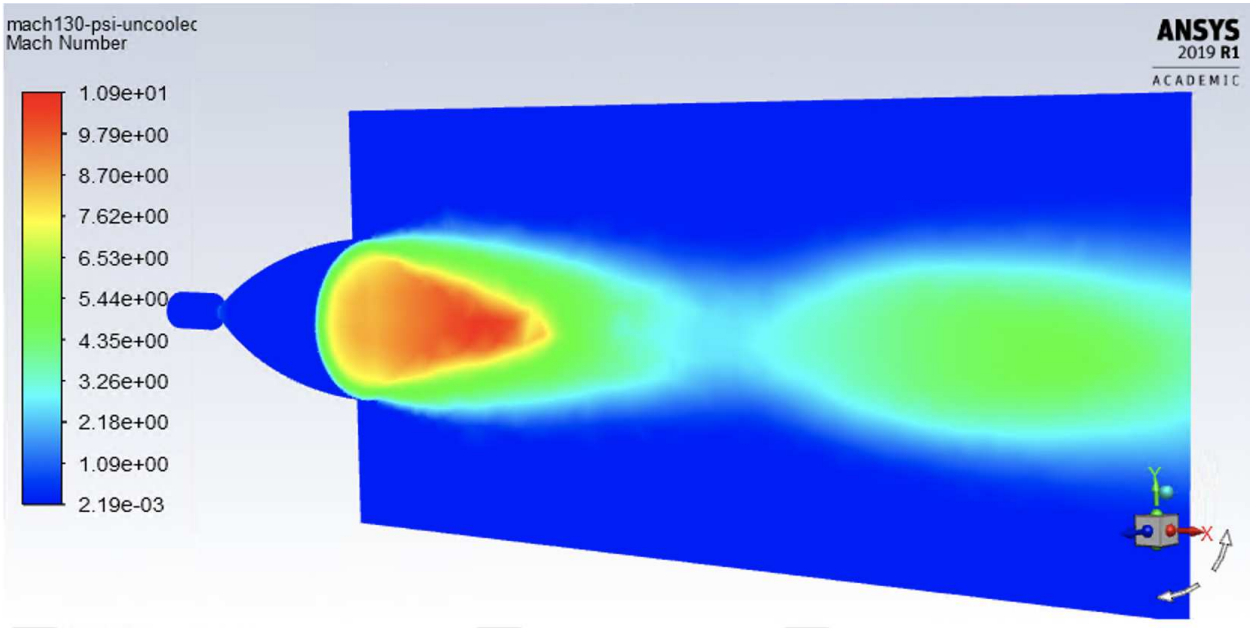

(a) Mach contours of 35° nozzle in 3D at 1 *kPa* atmospheric pressure

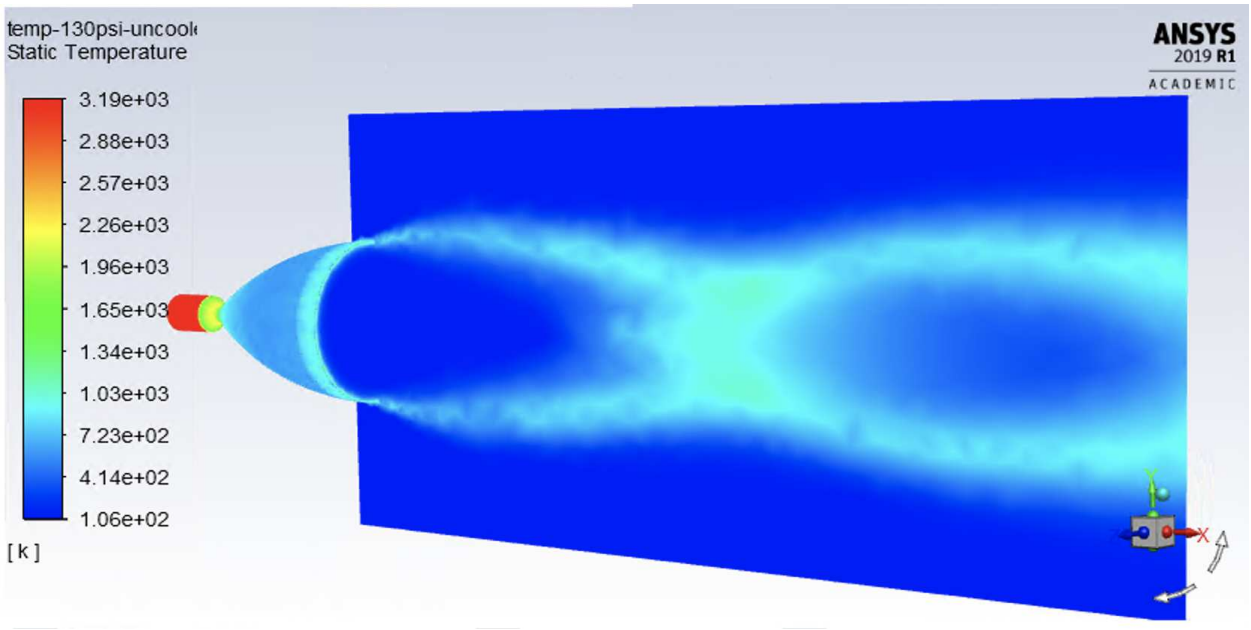

(b) Temperature contours of 35° nozzle in 3D at 1 *kPa* atmospheric pressure

Figure 5.12: Contours of 3D uncooled 35° nozzle at 1 *kPa* atmospheric pressure.

The temperature of the nozzle wall at the throat was calculated at 2419 K in the 2D model and 2307.4 K in the 3D model. At a supersonic area ratio of approximately four, which was the area ratio of the inlet of the annulus, the wall temperatures were found to be 1472.2 K in 2D and 1320.3 K, and the average temperature of the entire nozzle wall was 1336.3 K in 2D and 1306.0 K in the 3D models. The temperatures of both uncooled models were far above the allowable limit for maintaining material durability for any burn duration substantiating the necessity of a robust cooling design to allow long burn durations and ensure the longevity of the nozzle.

The converged simulations predicted similar combustion gas temperatures, but somewhat higher velocities as those shown by the NASA CEA equilibrium computations. The 3D model calculated an area-weighted average exit Mach number of 6.8, which is higher than NASA CEA predictions. This could because the Mach number changes dramatically in the radial direction, and NASA CEA calculates a single value. The values are within the limit to provide preliminary validation of accuracy. Accuracy was continually monitored for all simulations by utilizing consistent solution methods and comparing results. After simulations were run, the mesh was adapted for velocity and temperature gradients scaled by a global maximum. Simulations were run again to determine whether the predictions were mesh independent. The results were the same before and after mesh adaption, which implied the mesh had sufficient refinement in the regions with large gradients. Presumably, the full 3D predictions are more accurate than the single values for each selected axial location provided by NASA CEA code.

2D Annulus Models

Annular cooling is much simpler to model and analyze than cooling channels inside of a solid housing. Therefore, the initial cooled models were evaluated using a cooling annulus. Once the optimum boundary conditions, methods, and control settings were found for the uncooled simulations, two geometries with an annulus were generated in Design Modeler. One with the annulus defined as a fluid for the initial regenerative cooling simulations. The other with the annulus defined as a solid to present a closer geometric comparison to the annular cooling model. A high-quality mesh was created using the ANSYS Mesher with biases towards all walls and the throat of the

nozzle for boundary layer resolution. The mesh implemented for the 2D design with an annulus can be seen in Figures 5.13a and 5.13b.

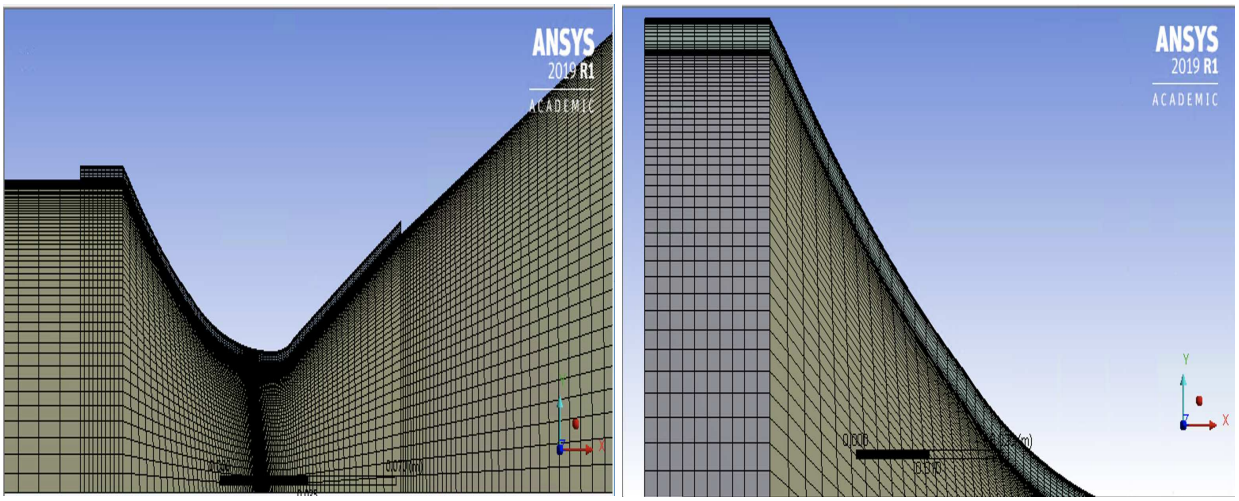

(a) 2D regenerative annulus mesh **(b)** Regenerative Annulus Mesh Zoom

Figure 5.13: 2D regenerative annulus mesh at throat

For consistency, the same controls, methods, and nozzle boundary conditions that had previously produced converged solutions in the 2D uncooled model were utilized in the initial annulus models, both uncooled and cooled. In the cooled annulus model, the inlet for the C_2H_4/C_2H_6 channel was tested both as a pressure and as a mass flow inlet boundary. The results were similar for both; however, the mass flow inlet boundary condition was found to be more consistent with NASA CEA and the analytical model over the range of chamber pressures and thus was utilized for the remainder of the simulations.

In 2D the required number of finite elements are far less for sufficient resolution and solution accuracy. This allowed for the plenum to be maintained to determine whether the cooling affected the exhaust behavior, while still achieving convergence within a reasonable timeframe. The solution for the uncooled annular simulation was consistent with the previous uncooled models, which provides preliminary validation of the predictive solutions, as seen in Figure 5.14.

The average wall temperature for the entire nozzle in the solid annulus uncooled simulations were 1305 K in the 130-psi model and 1384 K for the 200-psi chamber pressure model. These

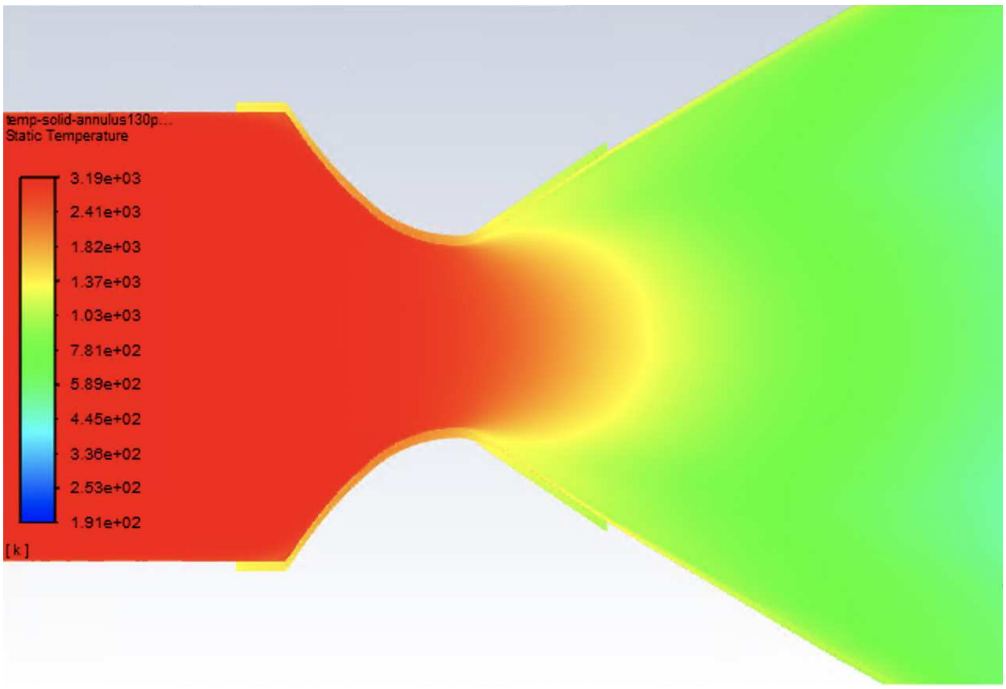

Figure 5.14: 2D uncooled nozzle temperatures 130-psi

temperatures are substantially greater than the thermal limit of steel. Steel begins to lose integrity at about 800 K; therefore, it would be ideal to maintain the temperature at around 700 K to ensure sustained nozzle wall strength.

For the cooled model, animations were created of the simulations to evaluate the behavior of the liquid C_2H_4/C_2H_6 filling the annulus, as well as to monitor potential changes in the exhaust behavior due to the reduced temperatures. The pressure outlet for the annulus was set at 6.895 MPa, which was the calculated exit pressure given the length of the annulus and thermophysical properties. The pressure outlet for the plenum was set at 1 kPa, and a plenum temperature of 233 K was stipulated. Simulations were then run using the previously calculated mass flow rates for the three chamber pressures investigated. The mass-flow rate, Mach number, annulus outlet temperatures, and residuals were monitored for convergence. A transient solution was initially run with a time step size calculated by dividing the average element size by the average velocity. The difference between the transient and steady-state solutions was negligible when compared to the

significant increase in computational time needed for a transient model; subsequently, steady-state solutions were employed for the remainder of the simulations.

The annular cooling model showed significantly lower wall temperatures, which confirmed heat transfer occurring in the simulation. The average nozzle wall temperature was 718.9 K for 130-psi chamber pressure and 732.8 K at 200-psi, which was approximately 585 K and 660 K cooler than the uncooled annulus models at the respective chamber pressures and below the 800 K limit for steel. However, according to both the 2D pseudo-transient and transient solutions, the C_2H_4/C_2H_6 transitioned into two-phase flow in the annulus for the 130-psi chamber pressure simulation. The computed temperature at the exit of the annulus was approximately 301 K for 130-psi chamber pressure and 292.3 K at 200-psi, essentially the boiling temperature, 292.5 K, of the C_2H_4/C_2H_6 mixture. The results of the 130-psi chamber pressure model can be seen in Figure 5.15.

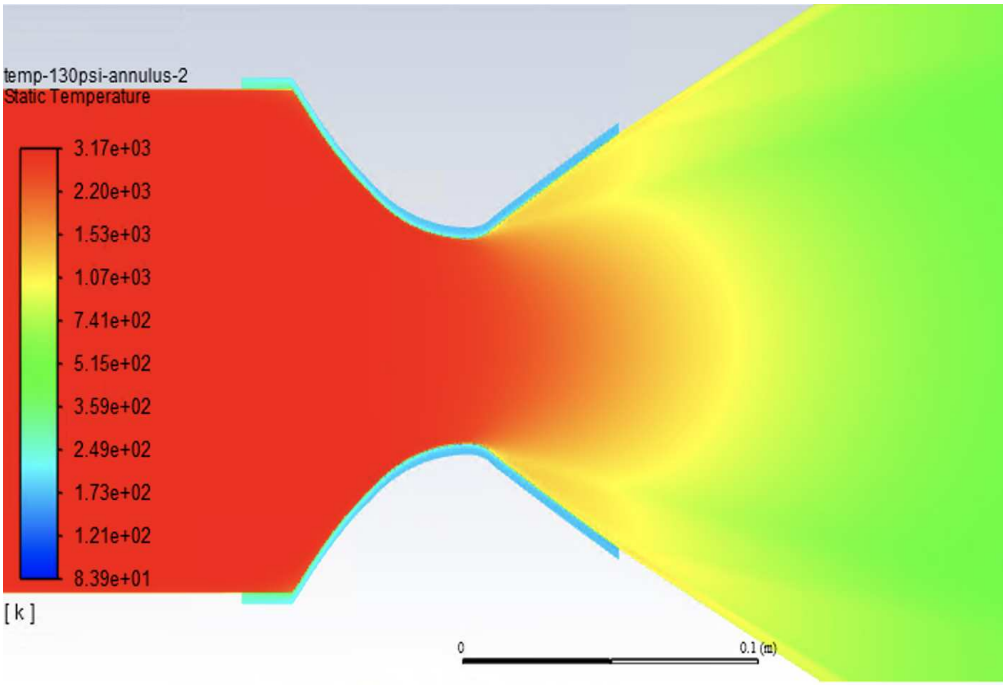

Figure 5.15: 2D regeneratively cooled temperatures of nozzle with annulus

The exit temperatures of the coolant calculated by the 2D annular regenerative cooling model were too close to the saturation temperature of the C_2H_4/C_2H_6 mixture to feel confident in the design. Moreover, the small thermal potential of the liquid phase and the importance of maintaining single-phase flow of the coolant required precise solutions and warranted the extra computational cost of full 3D simulations to ensure safety and preserve material resources.

3D Annulus Models

Injecting two-phase flow into the combustion chamber adds design complications, yet C_2H_4/C_2H_6 has a narrow temperature gradient to remain in the liquid phase. This mandates precision in the calculations of the coolant temperatures; therefore, the potentially added accuracy of a full 3D model is preferred. Annular models were developed in 3D using ANSYS Design Modeler. One design had a fluid annulus, and the other had a solid annulus for consistent geometric comparisons of heat transfer. The designs were then exported to ANSYS Meshing, and quality meshes were generated. The solid annulus mesh allowed for a hex-dominant mesh due to the lack of boundary layers, allowing for a greatly reduced number of elements and subsequently decreased computation time required for accurate predictions, as seen in Figure 5.16.

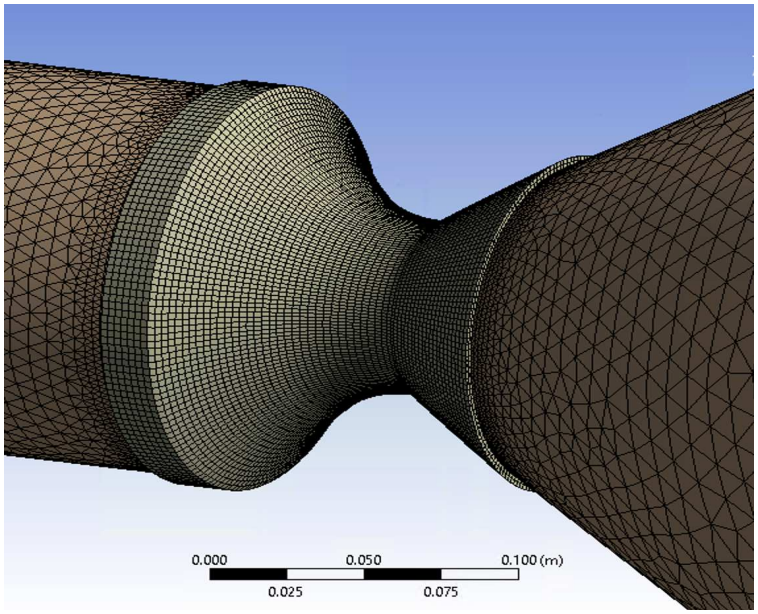

Figure 5.16: Mesh of the 3D solid annulus model

The annularly cooled design required boundary layer refinement of the mesh in both the nozzle and the annulus, and thus required 1.1×10^6 elements for proper solution resolution. The mesh with the boundary layer refinement near the walls of the fluid annulus can be seen in Figures 5.17a and 5.17b.

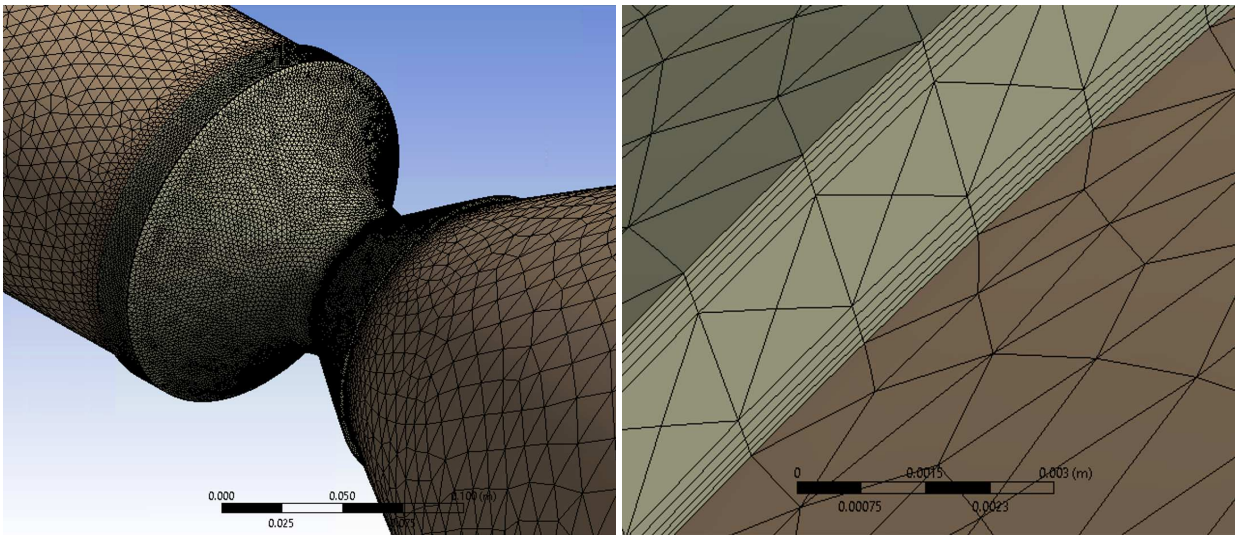

(a) Regenerative annulus mesh **(b)** Zoom of mesh for fluid annulus boundary layer

Figure 5.17: Mesh of the 3D fluid annulus

In Fluent post-processing, planes were created at both the XY-axis and the YZ-axis. Lines were generated in the nozzle wall at the entrance and exit of the annulus, the throat of the nozzle, and the combustion chamber wall. The vertex average temperature was calculated at each of these locations. In ANSYS Fluent, the vertex average is the integral of the vertex values divided by the number of vertices for the specified variable and surface. Additionally, the area-weighted average of the cooled portion of the nozzle wall was calculated. The cooling effects can be seen at the throat on the XY-plane in Figure 5.18. Figure 5.18a, which compares the uncooled model with a solid housing to the annular cooling model in Figure 5.18b. The thin green region seen in Figure 5.18b is the thermal boundary layer in the nozzle.

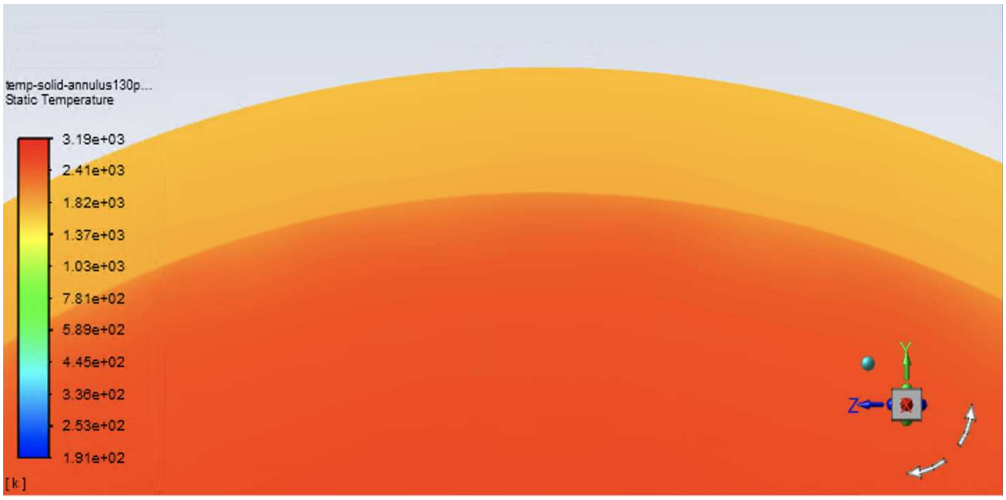

(a) Temperatures at throat in uncooled model 130-psi

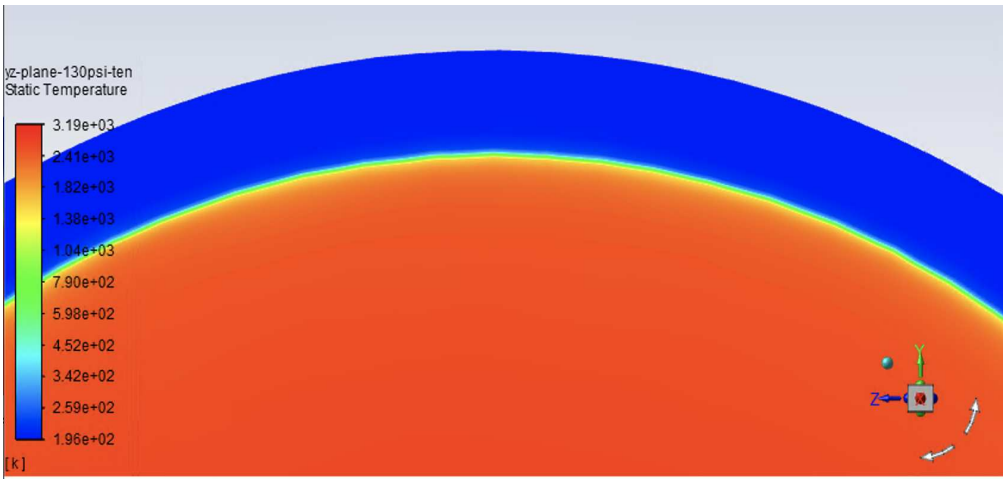

(b) Temperatures at throat in 3D annulus cooled model 130-psi

Figure 5.18: Temperatures of uncooled and cooled annular models on YZ-plane at throat

The 3D simulation at 130-psi chamber pressure calculated an annulus exit temperature of 288.9 K, which is 12.1 K less than the 2D model. The average wall temperature was 737.2 K in the nozzle at 130-psi chamber pressure, which was only 4.4 K higher than the 2D prediction. The coolant temperature at the exit of the annulus in the 3D model was 3.6 K below the boiling temperature for C_2H_4/C_2H_6 coolant temperature. This increased confidence in both the design and the computational expenditure of developing the full 3D models; yet still displayed marginal thermal energy absorption.

Table 5.2 shows the numerically calculated temperatures at the inflection locations along the nozzle wall for both cooled and uncooled 3D annular models, as well as the temperature of the coolant at the exit of the annulus for 130-psi and 200-psi chamber pressures. The nozzle wall temperature of the cooled section was an area-weighted average, while the wall temperatures at the throat, annulus inlet and exit were vertex averages on the 0.5 *mm* line created in the nozzle wall.

Table 5.2: Temperatures at specific locations in the nozzle wall and coolant temperature at annulus exit

Chamber Pressure, psi	**Coolant Outlet Temp, K**	**Annulus Inlet Temp, K**	**Nozzle Throat Wall Temp, K**	**Annulus Outlet Wall Temp, K**	**Cooled Section Wall Temp, K**	**Chamber Wall Temp, K**
130 cooled	288.9	509.8	797.4	899.7	737.2	2344.9
130 uncooled	N/A	1246.9	2006.6	1921.7	1847.2	2375.7
200 cooled	282.4	538.6	836.2	907.1	776.9	2439.2
200 uncooled	N/A	1322.9	2095.5	1980.4	1959.8	1720.2

Figure 5.19 illustrates the temperature differences between cooled and uncooled annulus models at 130-psi and 200-psi chamber pressure models in a bar chart.

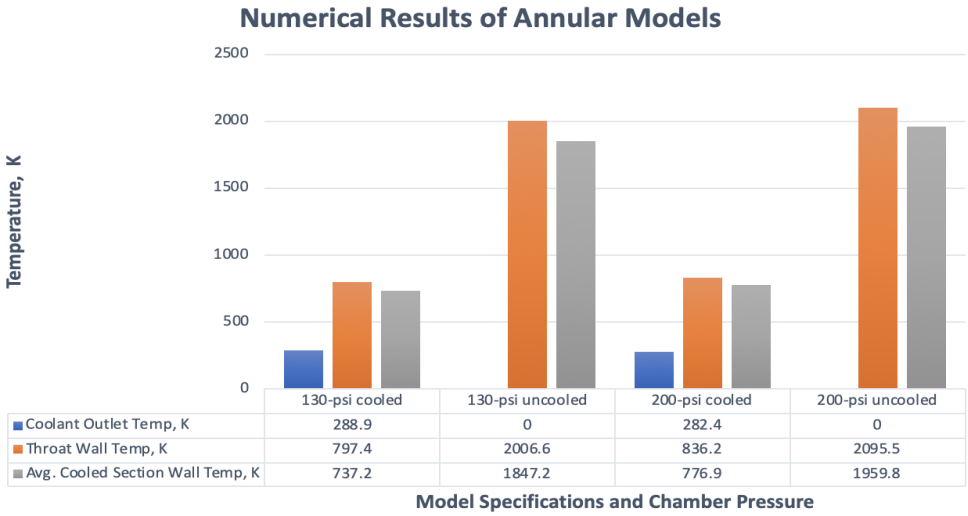

Figure 5.19: Bar chart of temperatures of annulus models

Figure 5.20 shows the isometric view of the isometric view of the entire 3D nozzle with a chamber pressure of 200-psi. Figure 5.20a shows the temperature contours of the nozzle for the uncooled solid annulus model for equivalent geometric comparison. Figure 5.20b shows the temperature contours of the annularly cooled model.

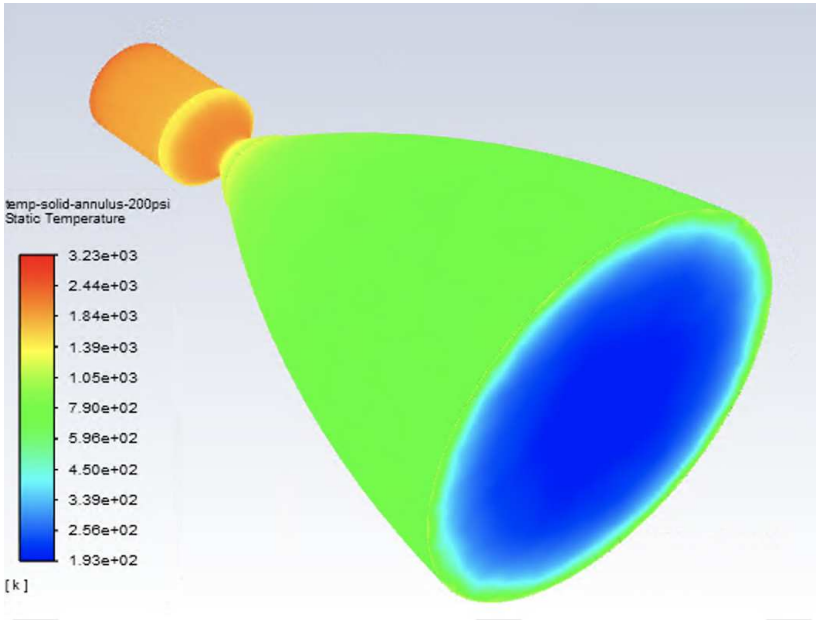

(a) Temperatures at 200 psi 3D solid annulus

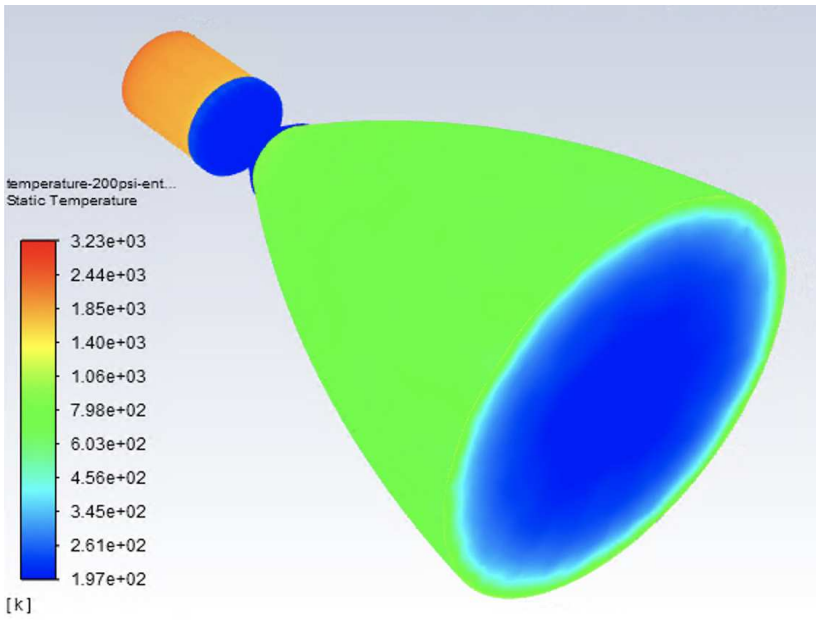

(b) Temperatures at 200 psi in 3D annulus cooling

Figure 5.20: Temperatures of uncooled and cooled 3D annulus model at 200-psi

The notable cooling effects at the throat of the nozzle seen in Figure 5.20 validates the cooling capability of regenerative cooling. The overall projections of the simulations were similar for both 2D and 3D; however, precision was paramount due to the modest allowable temperature gradient for the C_2H_4/C_2H_6 to remain in liquid phase throughout the length of the channels. These simulations exhibited that without cooling, the combustion chamber and throat region would reach unsustainable temperatures, and thus reiterated the necessity of developing a sufficient regenerative cooling method to maintain material strength and increase engine lifespans. Cooling channels are more challenging to manufacture than an annulus; however, due to the discrete channels and the parallel conduction and convection, a full 3D model was necessary for accurate predictions. Moreover, the channels augmented the cooling effects through more controlled flow and the solid material between the channels effectively acting like cooling fins. Additionally, advances in additive manufacturing have facilitated the production of more complex geometries. Therefore, the more complicated models utilizing cooling channels were investigated.

Single-Channel Models

The next stage of the project was to develop a model with single coolant channels in a steel housing and simulate the coupled FEA-CFD heat transfer and fluid dynamic behaviors. In addition to the convective cooling, the channels created a cooling fin effect due to the conduction from the combustion chamber to the atmosphere through the solid material between the channels. The predictions from the annular model indicated that a single-channel design may be necessary to absorb enough thermal energy to maintain material strength for the required burn duration while also ensuring the C_2H_4/C_2H_6 mixture remains in a liquid phase. Therefore, a single-channel design was built as an assembly of three separate parts in SolidWorks, the nozzle, housing, and the set of fifty channels.

Modeling in 3D substantially increased the overall number of finite volume elements. A relatively fine mesh was required for the steel housing and channels to ensure high-resolution of the boundary layers on all four walls of the small channels yet still have a conformal mesh between the channels and the housing. A conformal mesh is mandatory for heat transfer to occur within

the simulation. To limit computational time, regions with negligible gradients were designated to have larger mesh sizes. Nonetheless, approximately six million finite elements were created to provide accurate predictions. This necessitated remote access to a server capable of the computations within a reasonable time frame. For this reason, the plenum was eliminated from this model, which was justified by the attention being focused on the cooled section at the throat. The mesh developed for the single-channel model can be seen in Figure 5.21.

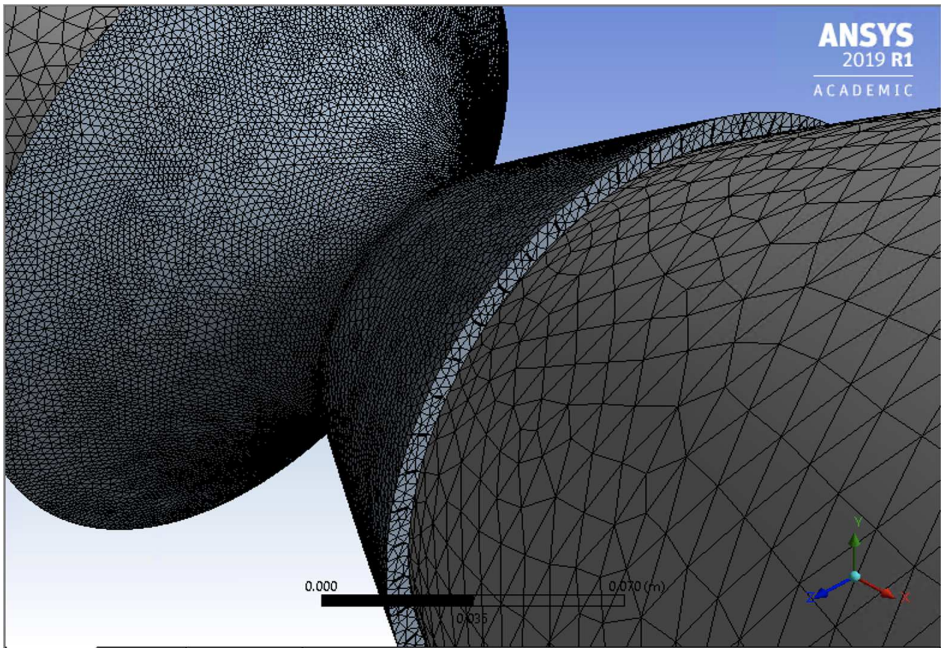

Figure 5.21: Mesh of single-channel regenerative cooling model

Each of the cooling channels were rectangular with a height of 3.3 *mm* and a width of 0.5 *mm*, giving a 6.604 aspect ratio, which is within the range found most effective by Pizzarelli [16]. The mesh was size to be finer towards the four walls of the channels as well as the nozzle wall to capture the high gradients in the boundary layers. The resolution in the boundary layer of the channels and the nozzle can be seen in Figures 5.22a and 5.22b.

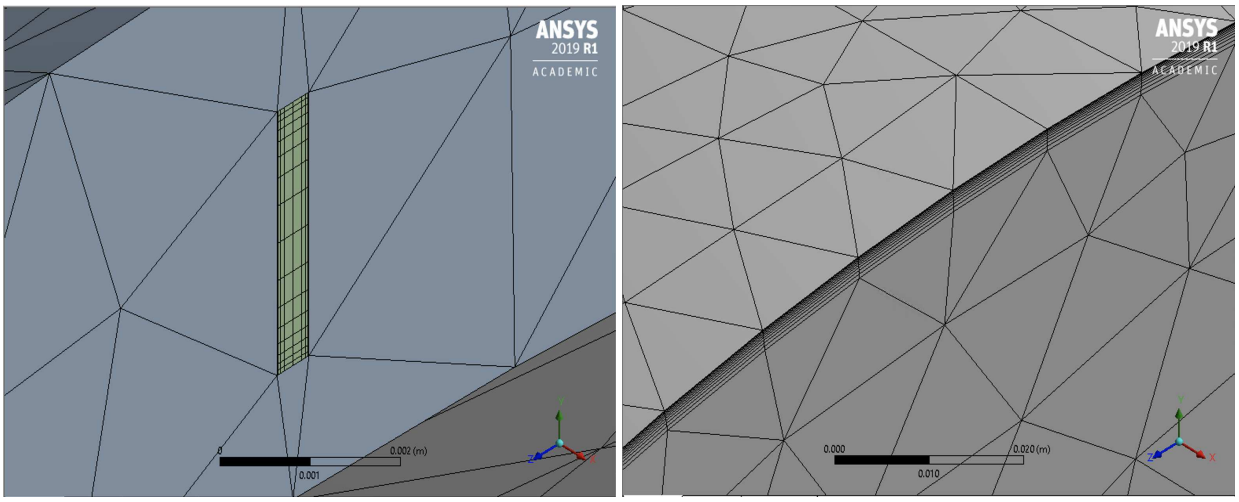

(a) Mesh for boundary layer of the channels in single-channel regenerative cooling model

(b) Mesh for boundary layer of nozzle in single-channel regenerative cooling model

Figure 5.22: Mesh of boundary layers in the single-channel regenerative cooling model.

A satisfactory mesh was created and exported to the solver, Fluent. In Fluent, the inlet and outlet of the nozzle were both set as pressure boundaries and chamber pressures of 130-psi, 200-psi, and 1000-psi were examined. The boundary conditions of the channels were specified as mass flow rate inlets and pressure outlets. The solution methods, and material properties were defined. The calculations were then initialized and the number of iterations were selected. Simulations were generated, and the channel mass flow rates, Mach number at the nozzle outlet, and scaled-residuals were monitored for convergence. The mesh was adapted, which asks Fluent to locate regions with high gradients and further refine the mesh in these regions. This was done until the solutions no longer changed, and were therefore mesh-independent, which further validates the models.

Once the mesh-independent solution converged, extensive post-processing results were analyzed. Graphical contours of the single-channel design were depicted for both cross-sections and in an isometric view. The isometric temperature contours were created both with the housing and with the housing suppressed. Suppressing the housing allowed the axial length of the channels to be observed. Animations were also created with the housing suppressed to monitor the coolant filling the channels as well as the behavior of the exhaust gas. Figure 5.23 shows the isometric view of the 200-psi chamber pressure design zoomed in on the nozzle throat with the coolant channels

exposed and filled with the liquid fuel coolant. The cooling effects on the nozzle wall are also apparent in Figure 5.23.

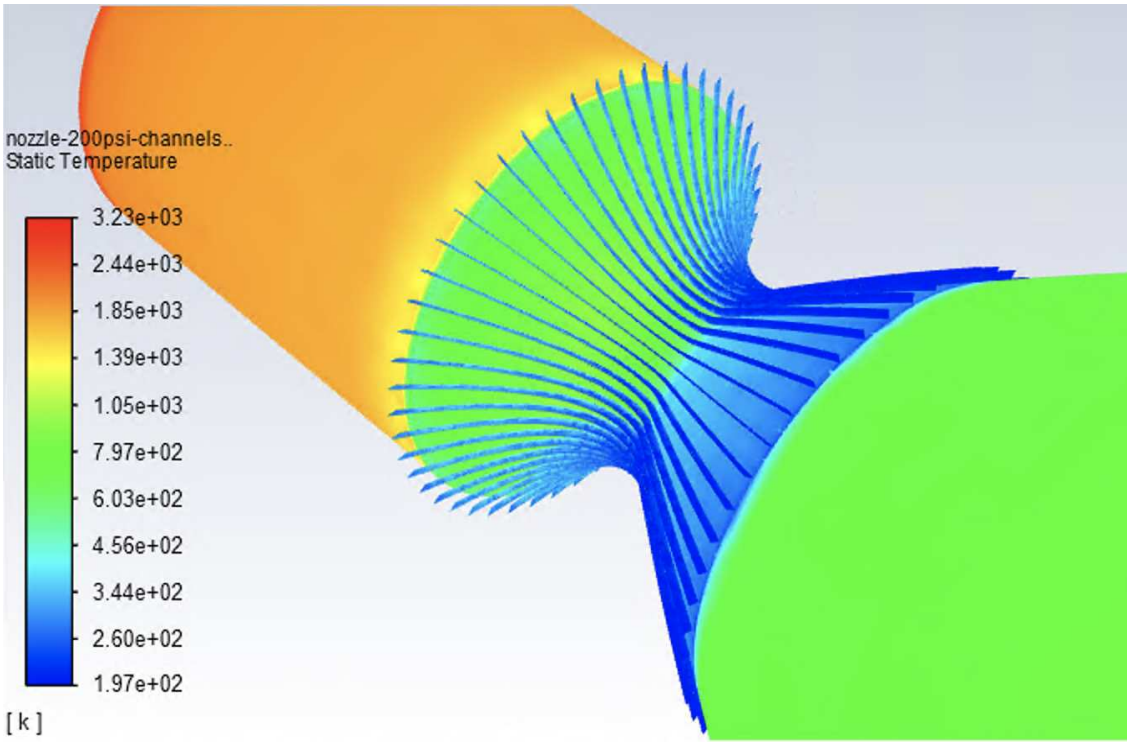

Figure 5.23: 3D temperature contour of single-channels at 200-psi zoom of throat

In Fluent post-processing, planes were created on the XY-axis and YZ-axis to observe the internal behaviors of the nozzle and channels. The predicted nozzle wall temperature at the housing inlet, the throat, and the housing outlet of the cooled model at 130-psi chamber pressure were 937.6 K, 1716.3 K, and 2336.6 K hotter in the uncooled model. The average wall temperature of the cooled model was found to be 722.8 K, which was 990.2 K lower than the uncooled model and within the range allowable for maintaining material integrity, which exemplifies the thermal energy absorption potential of regenerative cooling. Figure 5.24 shows the YZ-plane at the throat of the nozzle in both the uncooled and cooled models. Figure 5.24a shows that the solid housing was heated thoroughly by heat transfer to the wall from the exhaust gas in the nozzle, while Figure 5.24b shows the considerable potential of the single-channel regenerative cooling model.

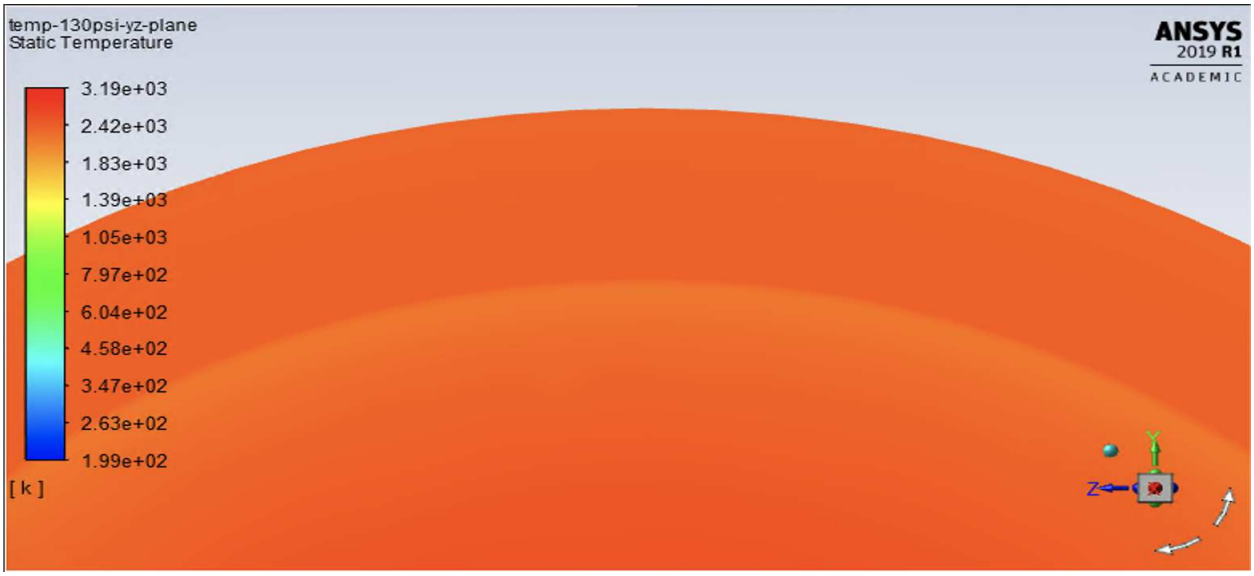

(a) Temperatures at 130-psi uncooled

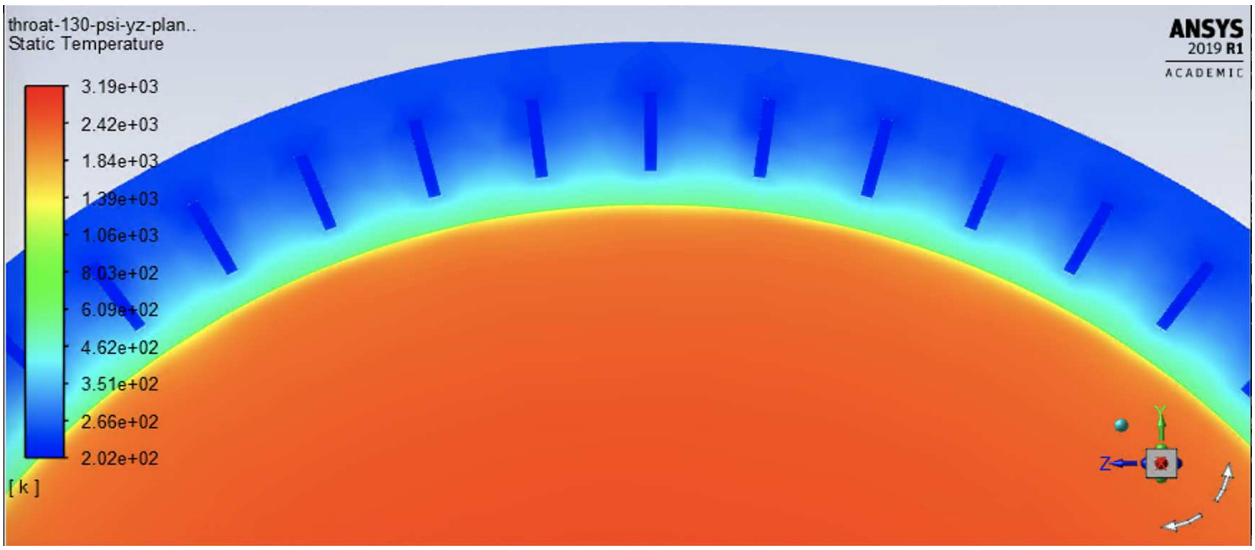

(b) Temperatures at 130-psi single-channel

Figure 5.24: Temperatures of 130-psi chamber pressure single-channel model and uncooled model.

In Fluent post-processing, additional lines were created on the XY-plane from the axis to the exterior surface of the housing. If the lines were to be illustrated in Figure 5.24, they would be from the x-axis in the positive y-direction to the exterior surface passing through the housing and the top-most center channel. The lines were created to observe the local temperatures and velocities as functions of radial position, allowing the boundary layer thicknesses to be discerned. The thermal gradients and boundary layers for the 130-psi single-channel model can be seen in Figure 5.25.

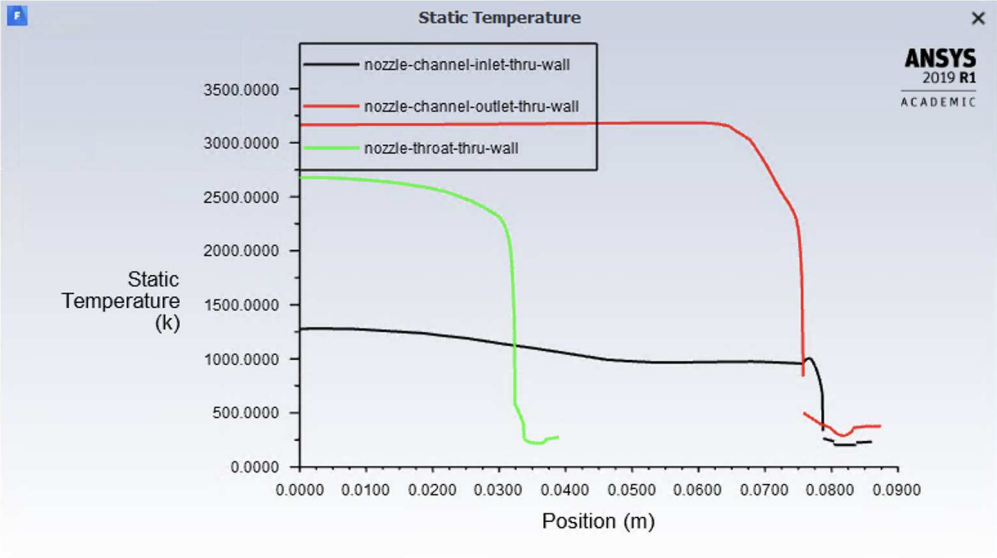

Figure 5.25: Thermal boundary layer for 130-psi single-channel model

The velocity gradients and boundary layers in the nozzle wall at the throat, inlet and outlet of the housing for the 130-psi model can be seen in Figure 5.26.

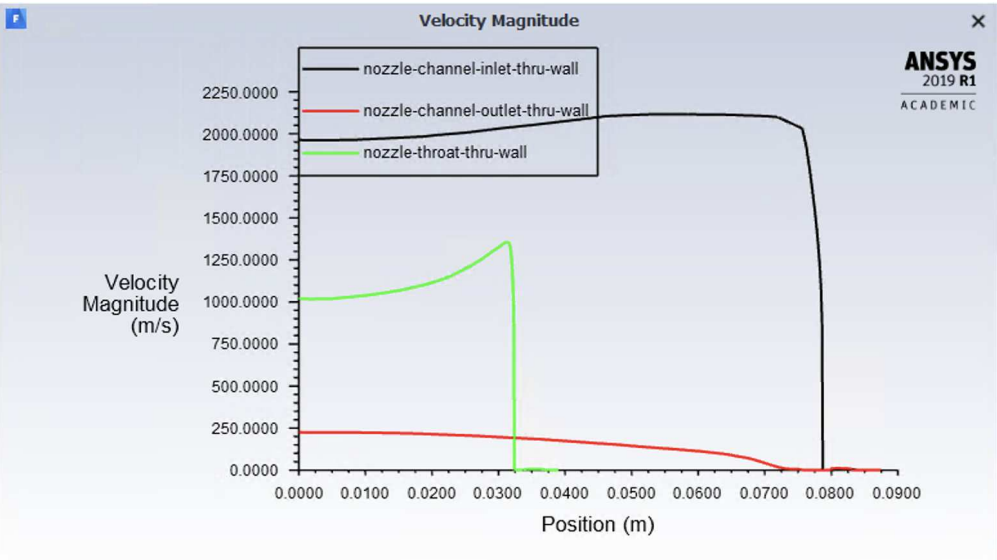

Figure 5.26: Velocity boundary layer for 130-psi single-channel model

Notably, in Figure 5.26, the velocity at the interface of the combustion chamber and converging section was much less than at the throat and in the diverging section due to the lower velocity and subsequent reduced turbulence created a much less defined boundary layer.

To further validate the behavior of the numerical analyses, simulations were run at 1000-psi chamber pressure using both the calculated mass flow rate of 1.6622 kg/s, which was the calculated value for 1000-psi chamber pressure, and the mass flow rate of 0.336 kg/s for 200-psi chamber pressures. The mass flow rate of 0.336 kg/s at 1000-psi yielded an exit temperature of the coolant of approximately 407 K. The results of the 1000-psi chamber pressure simulations confirmed that the reduced mass flow rate provided insufficient cooling at higher chamber pressures, as seen in Figure 5.27.

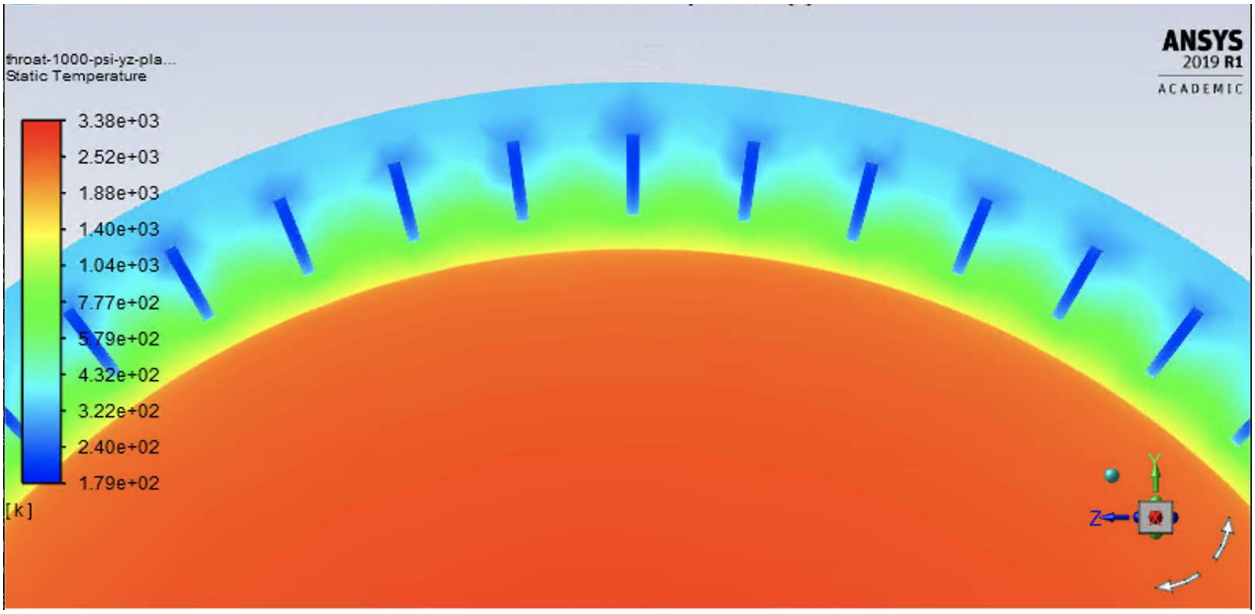

Figure 5.27: Temperatures at 1000-psi using mass flow rate for 200-psi

Comparatively, the outlet temperature of the coolant using the correct $\dot{m}$ was computed to be 252.7 K for the 1000-psi chamber pressure model, which is significantly less than the 292.5 K boiling temperature of the liquid fuel mixture and 154.3 K less than found with the lower mass flow rate. This supports the premise that regenerative cooling is more adequately suited for larger

payload rocket engines with the higher mass flow rates required for higher chamber pressures. The 200-psi model, as seen in Figure 5.28, had a channel exit temperature of 295.5 K using 0.336 kg/s, which is 3 K above the boiling temperature.

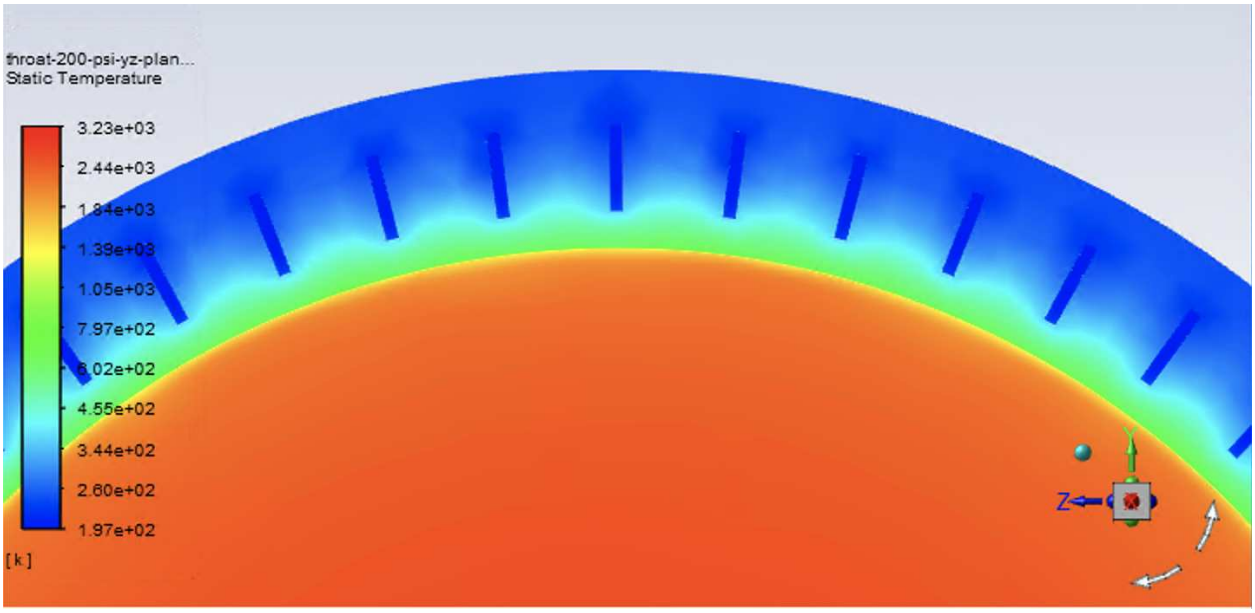

Figure 5.28: Temperatures at 200-psi

In Fluent post-processing, lines were created from the interior surface of the nozzle wall 0.5 *mm* in the positive y-direction on the XY-plane the thickness of the nozzle wall in the combustion chamber, at the outlet, and inlet of the channels, and the throat, and temperatures were evaluated at the lines. To establish an accurate comparison, a rocket engine with a solid uncooled housing was also simulated, and the vertex average temperatures were evaluated at the wall for each line. The vertex average temperatures at the lines in the combustion chamber, the inlet and outlet of the channel housing, and the throat of the nozzle were calculated, as well as area-weighted average temperatures of the coolant at the outlet and of the nozzle wall. The exact calculated values at the specified locations within the nozzle and the outlet coolant temperatures for the 130-psi and the 200-psi models are delineated in Table 5.3.

Table 5.3: Temperatures at specific locations in nozzle wall and outlet coolant temperatures of single-channel models. The boiling temperature of the coolant is 292.5 K.

Chamber Pressure, psi	Coolant Outlet Temp, K	Housing Inlet Temp, K	Nozzle Throat Temp, K	Housing Outlet Temp, K	Cooled Section Wall Temp, K	Chamber Wall Temp, K
130 cooled	303.5	639.6	688.4	739.4	722.8	1818.6
130 uncooled	N/A	1577.2	2404.7	3076	1713	3103.4
200 cooled	295.5	681.5	783.4	821.7	805.4	2020.6
200 uncooled	N/A	1648.3	2447.4	3155.6	1843.2	3178.5
1000 at 1.6622 kg/s	252.7	821.4	1053.1	935.2	1089.8	2781.3
1000 at 0.336 kg/s	407.0	1050.2	1143.4	1060.7	1099.3	2466.8

Figure 5.29 emphasizes the temperature differences between the cooled and uncooled single-channel models in the wall of the throat, the cooled section of the nozzle, and the outlet of the fuel coolant at both 130-psi and 200-psi chamber pressures.

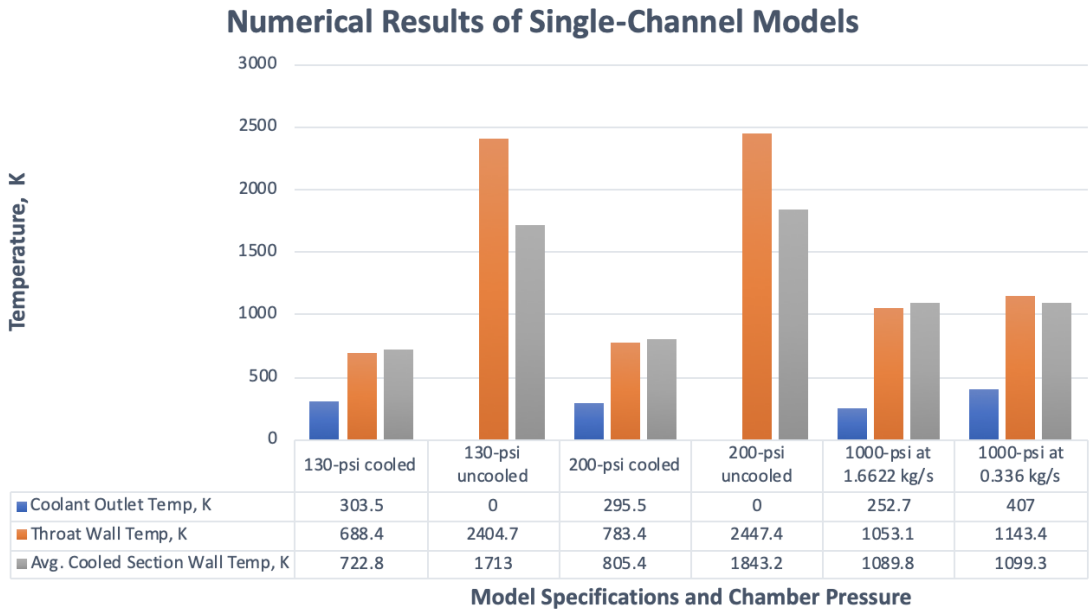

Figure 5.29: Bar graph of temperatures of both cooled and uncooled single-channel models

Despite the obvious cooling effect of the single-channel design on the nozzle walls, the outlet temperature of the C_2H_4/C_2H_6 from the channels in the 130-psi chamber pressure simulation was 303.5 K, which was 11 K above the boiling temperature of C_2H_4/C_2H_6 at the given pressure. The wall temperatures in the same locations along the nozzle were moderately higher for the 200-psi chamber pressure models due to the higher combustion temperature; however, the exit temperature of the C_2H_4/C_2H_6 mixture at the exit of the channels was 8 K cooler than the 130-psi model, which is still 3 K above the boiling temperature of 292.5 K, exhibiting the insufficient thermal energy absorption from the nozzle of the single-channel design. This motivated the investigation of the increased thermal absorption capability of a dual-channel regenerative cooling design potentially allowing the C_2H_4/C_2H_6 to remain in the liquid phase for the entirety of the channel at each of the chamber pressures of interest.

Dual-Channel Models

The single-channel model displayed significant thermal absorption capabilities; however, the results were insufficient, especially at the lower mass flow rates associated with lower chamber pressures. To avoid added injection design complications due to potential two-phase flow, a dual-channel design using both the fuel and the oxidizer as coolants in separate sets of channels was investigated. The mass flow rate of the N_2O is seven times higher than the C_2H_4/C_2H_6 mixture, providing more thermal absorption potential. Oxidizers typically are not utilized in regenerative cooling due to the possibility of fouling the channels; however, even long burn durations are relatively short time frames when considering fouling.

The channel housing was modified to accommodate a second set of cylindrical channels located distally to the 0.5 mm wide rectangular C_2H_4/C_2H_6 channels. The cylindrical channels having a diameter of 3.3 mm were staggered half-way between the rectangular C_2H_4/C_2H_6 channels to provide a direct conduction path from the interior nozzle wall. The dual-channel geometry was defined properly and exported to ANSYS Meshing. Figure 5.30a shows the boundary layer meshing of the channels, and Figure 5.30b shows the boundary layer in the nozzle.

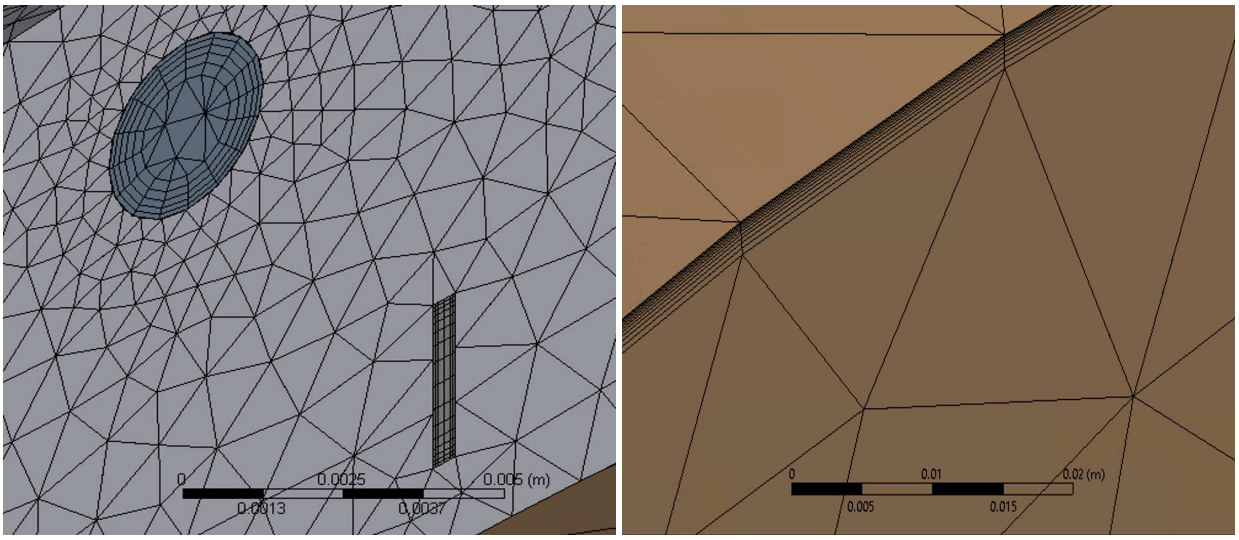

(a) Dual-channel boundary layers in channels **(b)** Dual-channel boundary layers in the nozzle

Figure 5.30: Dual-channel boundary layers in the nozzle

To achieve a high-quality conformal mesh in the one hundred small channels and the channel housing, over seven million finite control volume elements were required. Figure 5.31 shows the mesh of the channels with the housing suppressed.

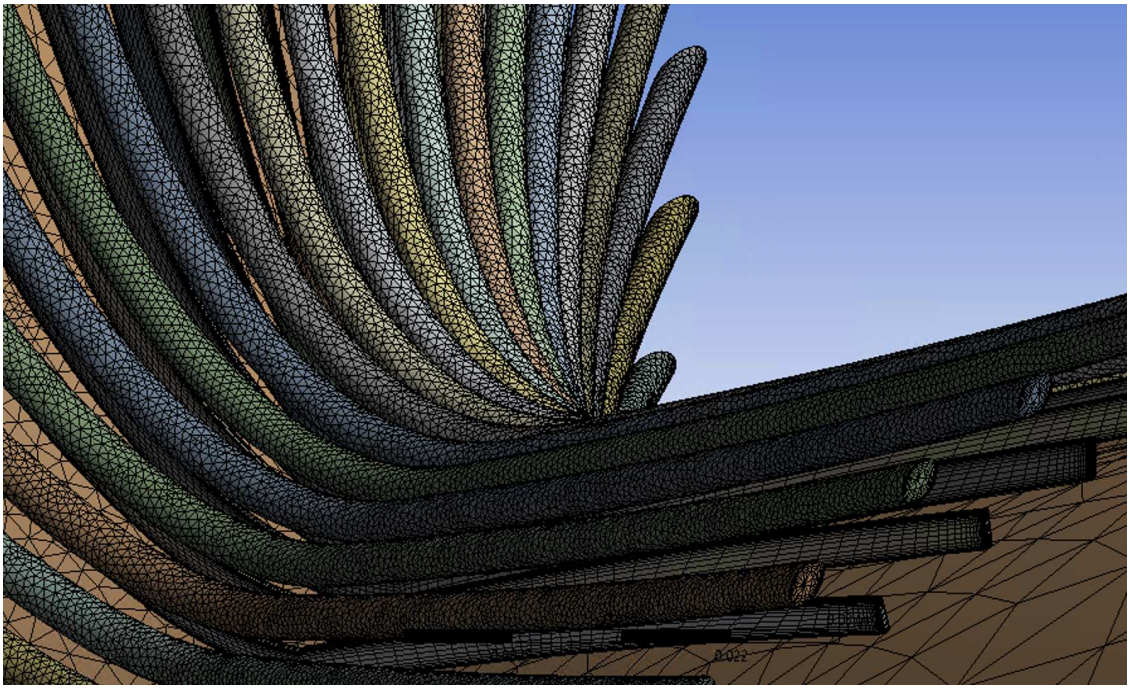

Figure 5.31: Mesh of dual-channel model with boundary layers

Figure 5.32 displays the mesh of the channel housing with the channels, as well as the larger element sizes of the nozzle. The nozzle had boundary layer refinement in the mesh, but could only be observed at the entrance and exit of the nozzle.

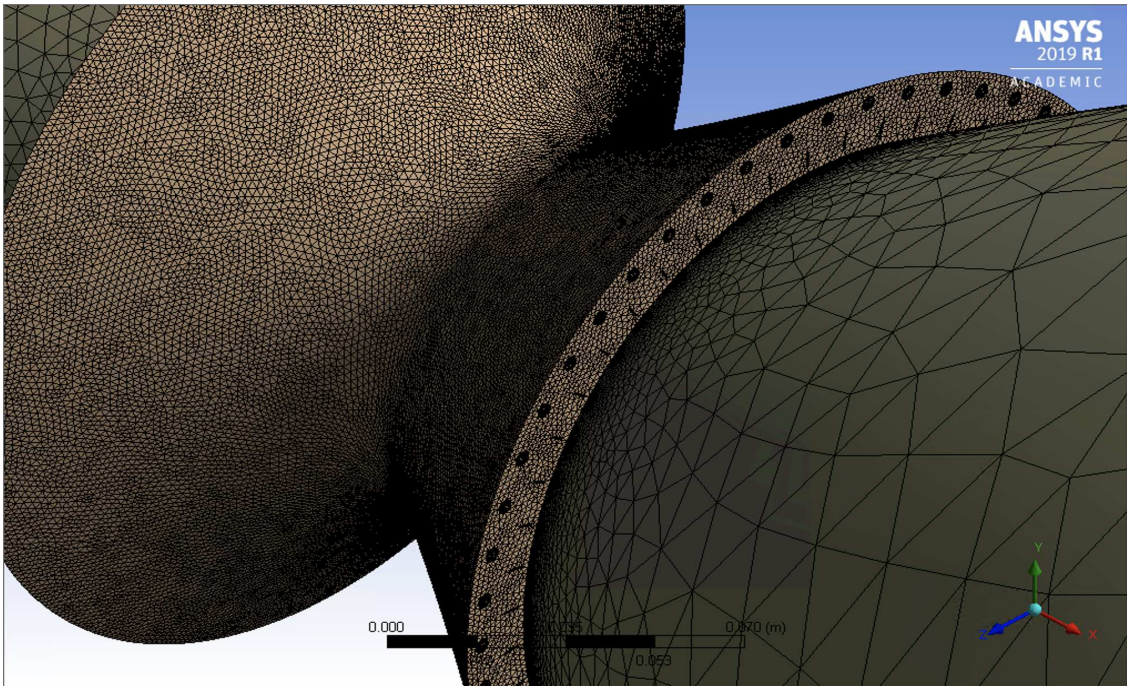

Figure 5.32: Mesh of dual-channel regenerative cooling

In the Fluent solver, the boundary conditions were set as before, with the channels being a mass flow inlet and the combustion chamber set as a pressure inlet. Thermophysical properties of the materials and heat transfer parameters were defined. A steady-state pressure-based solution method was utilized for the $k-\varepsilon$ turbulence model. Scaled residuals, mass flow rate, and temperature of the channel exit were monitored for convergence of the solution. Once convergence criteria were met, numerous post-processing details were examined. In Fluent post-processing, lines were drawn from the x-axis radially through the walls and channels at the housing inlet, exit, and the throat of the nozzle. The temperatures and velocities were plotted at these lines for observation of the thermal and velocity boundary layer thicknesses. The boundary layers were slightly thinner

with the higher chamber pressure; however, the difference was not noticeable enough to warrant displaying the plots.

Consistent with previous models, planes were created on the XY-axis and the YZ-axis for observation of the fluid dynamic behavior in the nozzle and channels. Additional lines were created at the same specified axial locations as the single-channel design within the nozzle walls to compute the wall temperatures at these inflection regions. Graphical representations of the dual-channel design were generated for both of the cross-sections, as well as in an isometric view. The isometric temperature contours were created both with the housing displayed and suppressed. Animations were created with the housing suppressed to monitor the fluids filling the channels and the behavior of the exhaust gas. The cylindrical N_2O channels were much larger than the C_2H_4/C_2H_6 channels to accommodate the larger mass flow rates. The rectangular C_2H_4/C_2H_6 channels are overshadowed by the cylindrical N_2O channels in Figure 5.33; nonetheless, the figure illustrates the nozzle throat with both sets of coolant channels exposed and filled with the liquid fuel coolant.

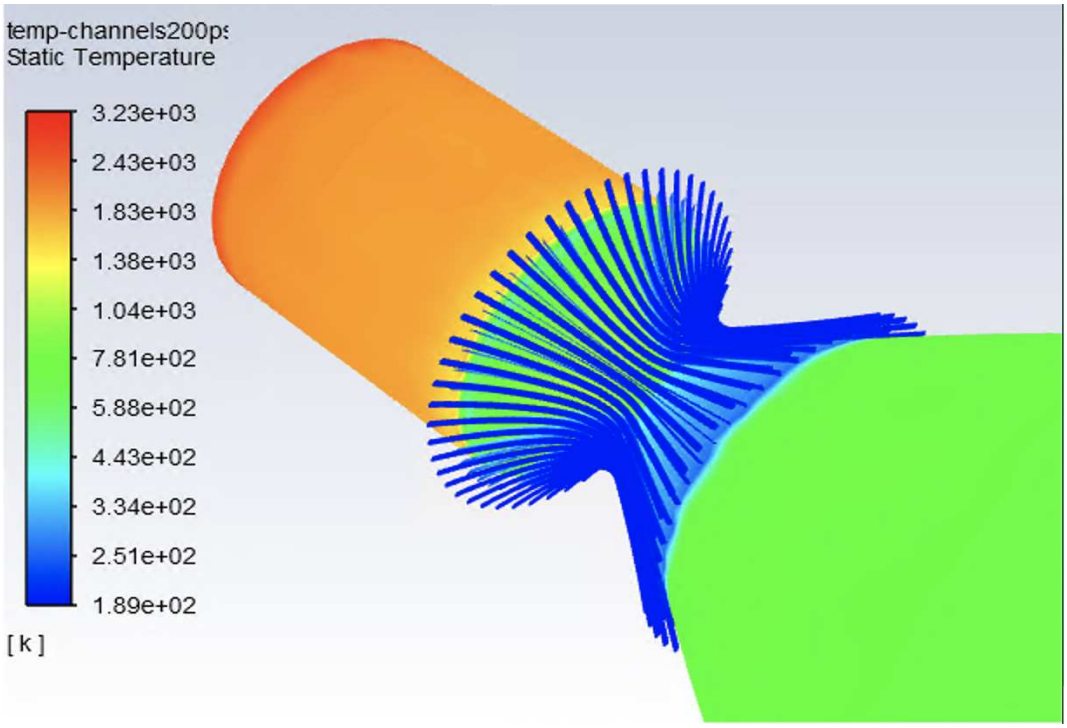

Figure 5.33: 3D temperature contour of dual-channel at 200-psi zoom

In the dual-channel design at 130-psi chamber pressure, the nozzle wall temperatures at the inlet and outlet of the channel housing and throat of the nozzle were 549.7 K, 591.2 K, and 613.1 K respectively. The average wall temperature of the cooled section of the nozzle was computed as 517.6 K, which is 205.2 K cooler than the single-channel simulation. The outlet temperature for the C_2H_4/C_2H_6 was found to be 285.0 K, which is 8.5 K cooler than the single-channel model and 7.5 K lower than the boiling temperature at the given pressure. The outlet temperature of the liquid N_2O was 206.7 K, which negligibly warmer than the inlet temperature. The temperature contours on the YZ-plane at the throat on the nozzle and housing for 130-psi chamber pressure can be seen in Figure 5.34, although the coolant in the channels did not absorb enough thermal energy to display a color differential on the scale of the plots.

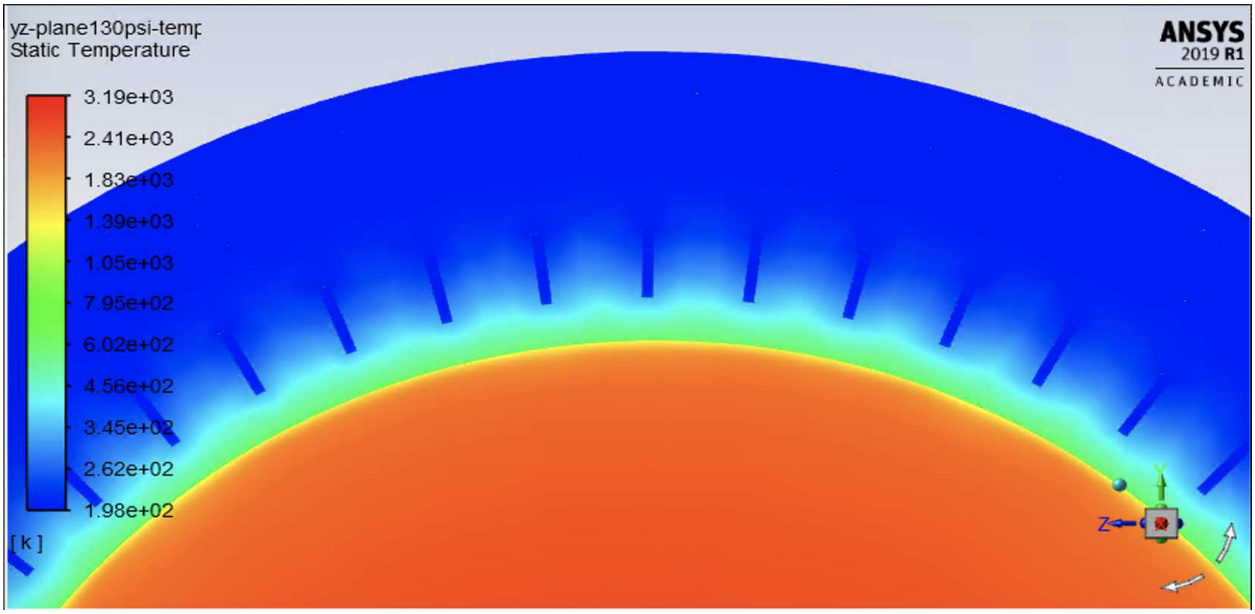

Figure 5.34: Temperature contour on YZ-plane of dual-channel model 130-psi

The increase of the temperature gradient in the axial direction within the channel housing on the XY-plane as well as the behavior of the exhaust gas can be seen in Figure 5.35. It can also be seen that the coolant temperatures remained below the critical values.

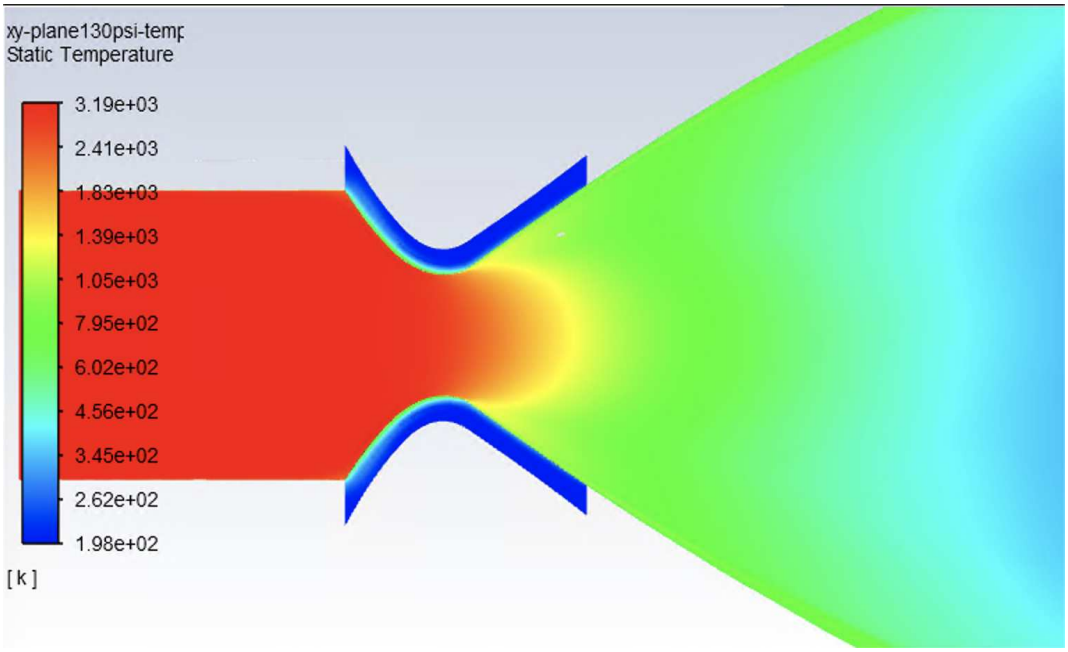

Figure 5.35: Temperature contour on XY-plane of dual-channel model 130-psi

The results of the CFD-FEA models of the heat transfer and fluid dynamics were consistent throughout the range of designs simulated. Table 5.4 differentiates the temperatures at the specified locations consistent with the single-channel simulations and the outlet temperatures of the coolants. The boiling temperatures of 292.5 K for C_2H_4/C_2H_6 and 299 K for the N_2O. The temperatures of the uncooled models are also tabulated for comparison.

Table 5.4: Temperatures at specific locations in nozzle wall and outlet coolant temperatures of dual-channel models

Chamber Pressure, psi	**Fuel Blend Outlet Temp, K**	**Nitrous Oxide Outlet Temp, K**	**Housing Inlet Temp, K**	**Nozzle Throat Temp, K**	**Housing Outlet Temp, K**	**Cooled Section Wall Temp, K**
130-psi cooled	285.0	206.7	549.7	613.1	591.2	517.6
130 uncooled	N/A	1577.2	2404.7	3076	1713	3103.4
200-ps cooledi	276.3	205.8	589.9	709.9	636.2	588.7
200 uncooled	N/A	1648.3	2447.4	3155.6	1843.2	3178.5
1000-psi cooled	242.8	788.7	1181.9	919.6	1048.5	781.3

Notably, the temperatures remained below the threshold of the allowable limits in the dual-channel models even at the lowest mass flow rate, which additionally validated the efficacy of the additional set of cooling channels. Figure 5.36 depicts the differences in temperatures between the cooled and uncooled dual-channel models for both 130-psi and 200-psi chamber pressures.

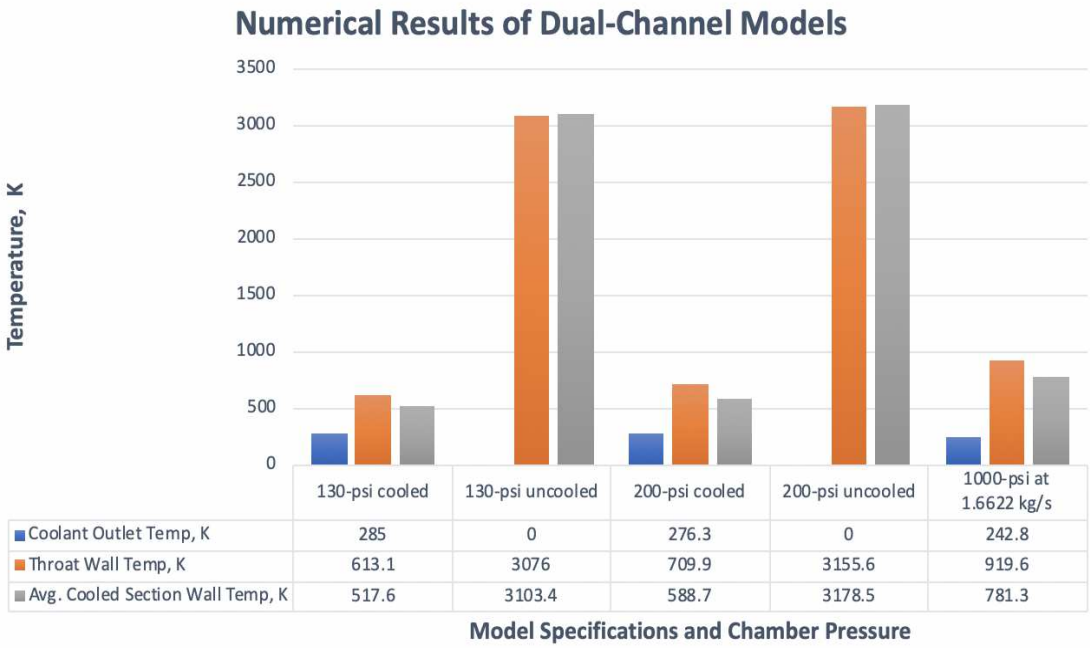

Figure 5.36: Bar graph of temperatures of both cooled and uncooled dual-channel models

Due to the distal location of the nitrous oxide channels, there was a negligible temperature gradient between the liquid nitrous oxide and the steel housing. This caused the channels to be imperceptible in the graphical representations on the YZ-plane cross-section at the throat in the130-psi and 200-psi chamber pressure simulations. In the higher chamber pressure models the temperature gradient profile allowed the temperature scale of the post-processor to differentiate the channels from the housing. Therefore, to observe the cylindrical N_2O channels inside of the steel housing, the temperature contour of the 1000-psi chamber pressure model is depicted in Figure 5.37.

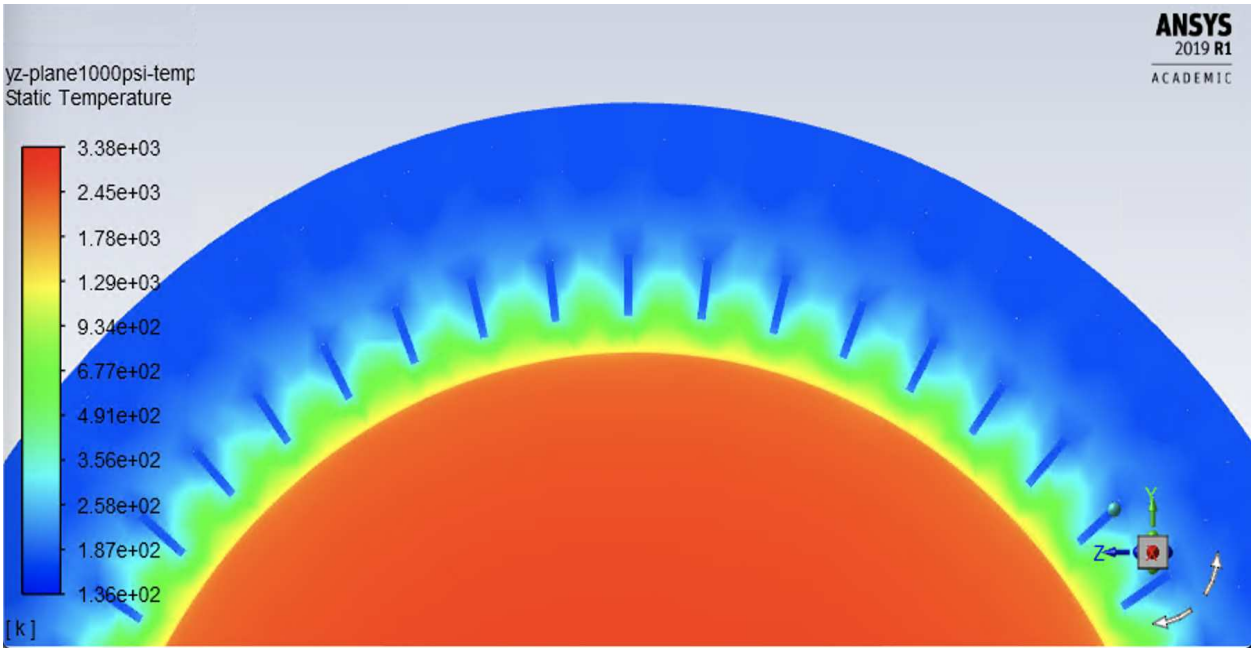

Figure 5.37: Temperature contour on YZ-plane of dual-channel model 1000-psi

In Fluent post-processing, twenty points were generated at equidistant intervals along the center-line of both the C_2H_4/C_2H_6 and N_2O channels to monitor temperature changes throughout the channel lengths. The vertex average temperatures were computed at each point for all chamber pressures investigated. The temperatures were plotted with respect to axial position within the channel to further display the effects of mass flow rate and chamber pressure on the coolant temperatures; however, the N_2O coolant temperature increases were negligible.

The single-channel and dual-channel model coolant temperatures along the channels are depicted in Figure 5.38. Figure 5.38a displays the temperature of the fuel coolant surpassing the constant green line that represents the boiling temperature. The insufficient thermal absorption capabilities of the single-channel design motivated the investigation of the dual-channel design. Figure 5.38b displays the temperatures remaining below the critical values in the dual-channel simulations at all chamber pressures investigated.

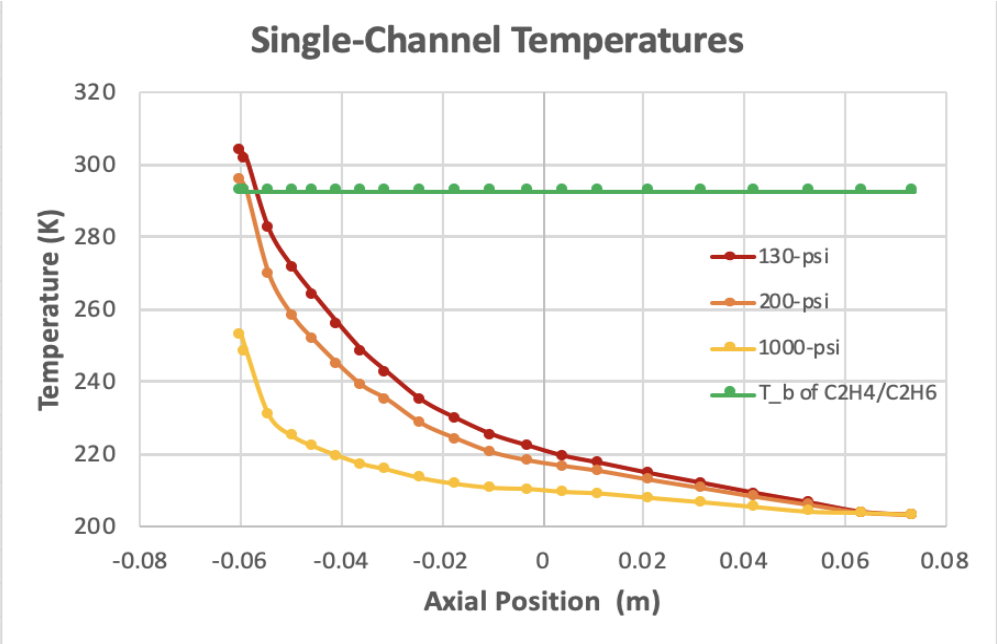

(a) Channel temperatures for all chamber pressures with constant mass flow rates

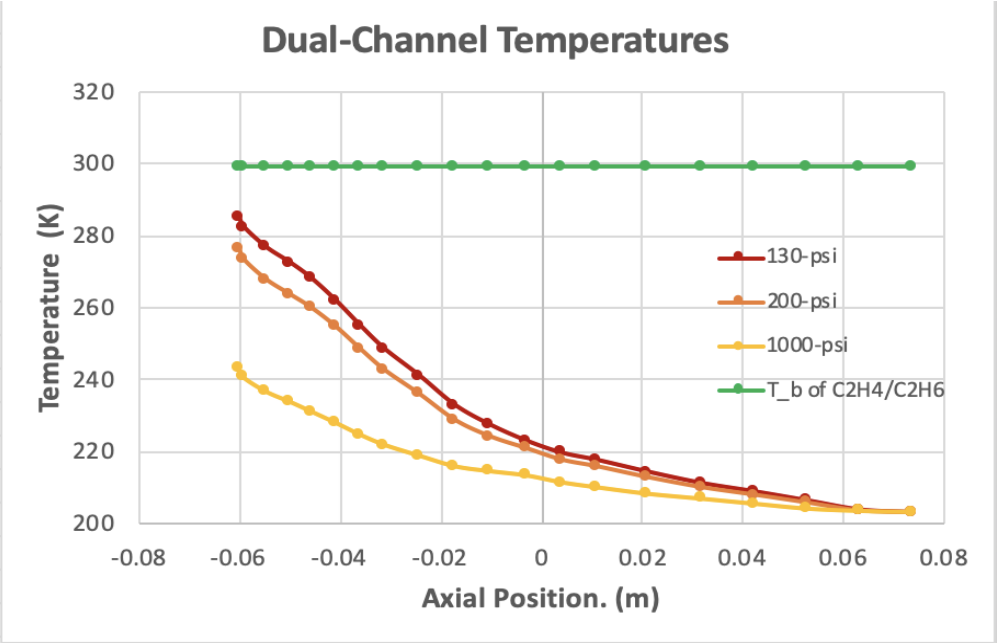

(b) Channel temperatures for all chamber pressures with C^* calculated mass flow rates

Figure 5.38: Comparing channel temperatures for all chamber pressures and all mass flow rates

The analytical and numerical methods displayed closely correlated results for both the single-channel and dual-channel models at all chamber pressures investigated. Table 5.5 compares the temperature values of the analytical and numerical analyses for the 130-psi and 200-psi chamber

pressure models in both the single-channel and dual-channel designs. The area-weighted average was selected for the temperatures of the C_2H_4/C_2H_6 coolant throughout the channels, the steel housing, and the exhaust gas at the throat. The vertex average was stipulated for the temperatures at the exits of the channels, as well as the walls. For brevity, SC signifies single-channel and DC is dual-channel in Table 5.5.

Table 5.5: Comparable temperatures for all modeling methods

Modeling Method, Cooling Design, and Chamber Pressure, psi	**Average C_2H_4/C_2H_6 Temp, K**	**C_2H_4/C_2H_6 Outlet Temp, K**	**Average Housing Temp, K**	**Throat Wall Temp, K**	**Average Exhaust Gas Temp at Throat, K**
Numerical SC 130-psi	246.3	303.5	414.5	688.4	2675.6
Analytical SC 130-psi	245.9	303.1	N/A	691.2	2882.9
Numerical SC 200-psi	241.5	295.5	438.8	783.4	2711.1
Analytical SC 200-psi	242.1	296.1	N/A	791.4	2907.5
Numerical DC 130-psi	236.3	285.0	286.0	613.1	2702.3
Analytical DC 130-psi	238.7	285.9	N/A	623.9	2882.9
Numerical DC 200-psi	233.3	276.3	296.9	709.9	2737.5
Analytical DC 200-psi	235.7	280.9	N/A	720.9	2907.5

The calculated values had satisfactorily small deviations between the analytical and numerical models, thus providing prediction validation. Moreover, the analytical model produced comparable results with much less effort and expense of the CFD/FEA software licenses. Figure 5.39 utilizes a bar chart to facilitate the comparison of the temperatures of the coolant at the outlet, the nozzle wall at the throat, and the average wall temperatures of the cooled section of the nozzle for the both analytical and numerical modeling methods for the single-channel and dual-channel designs at 130-psi and 200-psi chamber pressures.

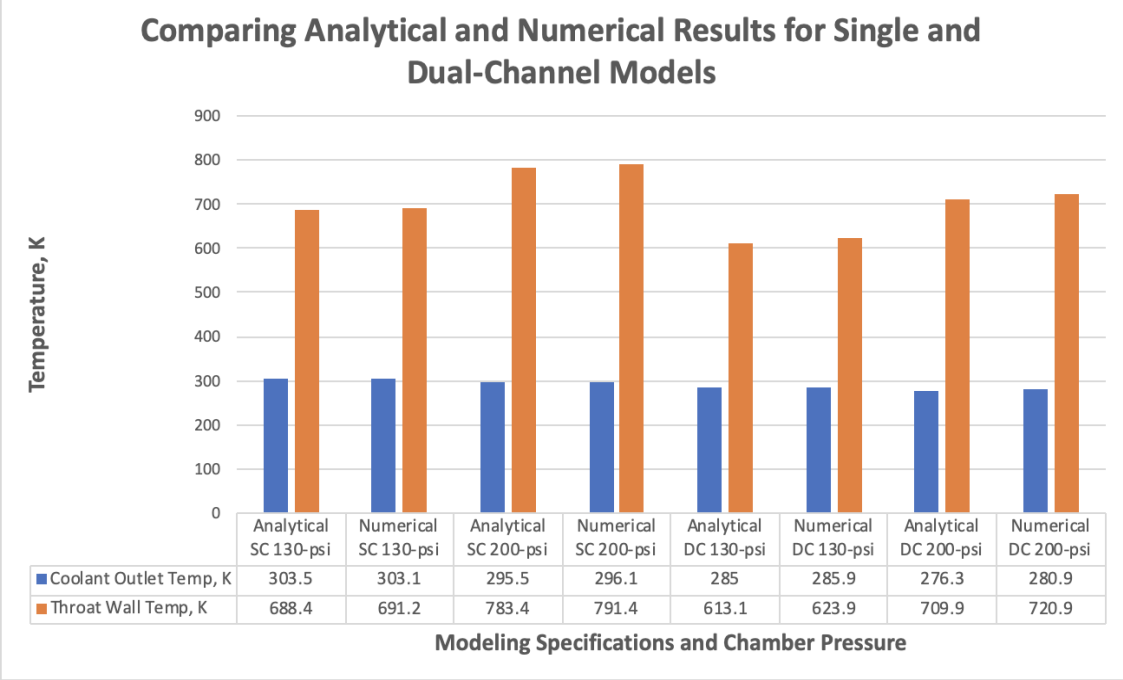

Figure 5.39: Bar graph of temperatures of all modeling methods and cooling designs

Chamber pressure is proportional to mass flow rate; therefore, despite the higher combustion temperatures, regenerative cooling has been more adequately suited for larger payload rocket engines. The analytical and numerical models consistently demonstrated the challenge of cooling low-pressure rocket engines. The addition of the nitrous oxide channels provided the necessary heat reduction to permit long burn durations at all chamber pressures examined. Contemporary advancements in additive manufacturing render previously impossible designs to be deftly fabricated in a wide array of materials. Subsequent experimental validation of the computational analyses is the requisite next step; however, the results of both the analytical and numerical models show promise.

Chapter 6

Future Works

Computational analyses are useful tools for informing optimal designs, preserving valuable time, and mitigating costly design flaws, yet models and simulations can continually be improved. Future works could include optimization studies of fuel type and the effects of the relative location and geometry of channels on cooling. The single-channel models cross-sections shown are at the throat, which is the most narrow region of the nozzle. Nonetheless, there is sufficient solid material between the channels to accommodate more channels in closer proximity to each other. It would be worth investigating whether this could provide sufficient cooling.

Additional potential future work could include determining whether the pressurized oxidizer would be sufficient as the sole coolant in a set of single channels due to the typically larger mass flow rates. The single-channel design was simpler to analyze and build, although experimental verification of channel fouling needs to be performed to ensure safe implementation.

It would be useful to derive the convection coefficients from the calculated properties despite CFD software not considering internal convection to compare with the analytical calculations. The values were strikingly similar considering the distinctly different modeling methods. Further research into the various assumptions and methods that potentially balanced to yield such remarkably similar results could provide constructive insight.

Future work also mandates experimental validation of recession rates of various ablative materials for liquid fuel over a range of chamber pressures. The literature surveyed only examined ablation rates for solid fuel at chamber pressures of 1000-psi and greater, yet having empirical functions for erosion rates for a wide range of materials and chamber pressures is vital for accurate performance predictions. Lastly, investigating the potential for utilizing regenerative cooling near the throat of the nozzle in conjunction with non-pyrolyzing ablative material in the combustion chamber and pyrolyzing material with high recession rates in the bell to possibly mitigate the change in supersonic area ratio could prove to be adventagous.

Chapter 7

Conclusion

Rocket engines need to be able to withstand the extreme temperature gradients that induce excessive heat transfer and material stress. Regenerative and ablative cooling methods have been deployed successfully for decades; however, each has inherent drawbacks. Ablative material erosion near the throat reduces engine performance over time. Regenerative cooling adds mechanical complications, thus weight and risk of failure. Moreover, effective regenerative cooling requires high mass flow rates characteristic of large rocket engines. The development of scalable regenerative cooling designs capable of absorbing sufficient thermal energy is cardinal to meet the ever-increasing demand of small payload engines, such as low-Earth orbit (LEO) launches. The ability to cool low-pressure rocket engines in combination with the employment of high-performance, yet relatively non-toxic, non-corrosive, stable, and inexpensive propellant, have the potential to attenuate the financial and environmental impacts of such launches.

- Ablative cooling is cost-effective, relatively simple to implement from a manufacturing perspective, and provides sufficient cooling. However, ablative material recession at the throat adversely affects engine performance progressively throughout the burn duration of the rocket. Therefore recession rates are the principal consideration to maintain optimal propulsion.

- Regenerative cooling is more mechanically complicated, and thus more expensive and prone to failure. Although utilizing the fuel as coolant boosts combustion efficiency by increasing enthalpy.

- Large payload rocket engines are more amenable to regenerative cooling due to the larger mass flow rates providing sufficient thermal energy absorption. Therefore, using the fuel as the sole coolant in low-pressure engines may not satisfy cooling demands. In the single-

channel design, the fuel coolant temperature surpassed the critical value and underwent a phase change within the channels.

- Utilizing both the fuel and oxidizer in separate sets of cooling channels yielded wall and coolant temperatures below the critical values; whereas, the single-channel design produced marginal temperatures in the models evaluated for this research. The dual-channel design provided the necessary supplementary thermal energy absorption to allow the coolants to remain single-phase for the entirety of the channels.

This research has exhibited that the regenerative cooling designs investigated are scalable from much larger launch size rocket engines to more modest payloads. Agreement was achieved across analytical analyses and numerical simulations for the range of chamber pressures investigated, providing ancillary validation of the modeling methods employed and the required confidence in the wall and outlet temperatures of the coolants. In both computational analyses, the single-channel design produced borderline results. The additional set of oxidizer coolant channels supplied the supplementary thermal energy absorption required to maintain the wall and fluid temperatures below the allowable limits.

Integrating ablative cooling in the combustion chamber and nozzle bell with dual-channel regenerative cooling near the throat has the capacity to provide adequate heat removal to ensure sustained material robustness and single-phase flow of the coolants indefinitely. Furthermore, keeping the temperatures below the threshold for long burn durations facilitates the prospect of reusable LRE's. These predictions have the potential to mitigate financial and environmental costs and propel the field of aerospace engineering into the future.

Bibliography

[1] G.P. Sutton and O. Biblarz. *Rocket Propulsion Elements, 7th ed.*, volume 7. John Wiley & Sons, NY, USA:, 2001.

[2] Cheryl L. Resch. Ablation models of thermal protection materials. *Johns Hopkins APL Technical Digest, Volume 13, Number 3*, pages 426–430, 1992.

[3] G. Paul Richter and Timothy D. Smith. Ablative material testing for low-pressure, low-cost rocket engines. Technical report, Lewis Research Center, NASA Technical Memorandum 107041, Cleveland, Ohio, October 1995.

[4] K. Klager. The interaction of the efflux of solid propellants with nozzle materials. *Propellant, Explosives, Pyrotechnics, Volume 2, Number 3*, pages 55–63, 1977.

[5] K. K. Kuo and S. T. Keswani. A comprehensive theoretical model for carbon/carbon composite nozzle recession. *Combustion Science and Technology, Volume 42, Number 3–4*, pages 145–164, 1985.

[6] P. Thakre and V. Yang. Chemical erosion of carbon-carbon/graphite nozzles in solid propellant rocket motors. *Journal of Propulsion and Power, Volume 24, Number 4*, pages 822–833, 2008.

[7] Masoud Ommati, Ahmadi Iman Fotovat, Seyed Mohammad Davachi, and Siamak Motahari. Erosion rate of random short carbon fibre/phenolic resin composites: modeling and experimental approach. 2011.

[8] S. D. Williams and Donald M. Curry. Thermal protection materials: Thermophysical property data. Technical report, NASA Johnson Space Center; Thermal Branch, Houston, TX, December 1992.

[9] Craig W. Ohlhort, Wallace L. Vaughn, Phillip O. Ransone, and Hwa-Tsu Tsou. Thermal conductivity database of various structural carbon carbon composite materials. Technical

report, Langley Research Center, NASA Technical Memorandum 4787, Hampton, VA 23365, November 1987.

[10] P. Thakre, T. Rawat, R. Clayton, and V. Yang. Chemical erosion of carbon-carbon/graphite nozzles in solid propellant rocket motors. *Journal of Propulsion and Power, Volume 29, Number 3*, pages 593–601, 2013.

[11] Donald M. McEligot, W. David Swank, David L. Cottle, and Francisco I. Valentin. Thermal properties of G-348 graphite. Technical report, Idaho National Laboratory, USDOE, Idaho Falls, Idaho 83415, May 2016.

[12] Howard G. Maahs. Ablation performance of glasslike carbons, pyrolytic graphite and artificial graphite in the stagnation pressure range 0.035 to 15 atmospheres. Technical report, Langley Research Center, NASA Technical Note D-7005, Hampton, VA 23365, December 1970.

[13] Daniele Bianchi, Francesco Nasuti, and Emanuele Martelli. Coupled analysis of flow and surface ablation in carbon-carbon rocket nozzles. *Journal of Spacecraft and Rockets, Volume 46, Number 3*, pages 492–500, 2009.

[14] Marco Pizzarelli. Regenerative cooling of liquid rocket engine thrust chambers. Agenzia Spaziale Italiana, November 2017.

[15] Mary F. Wadel. Comparison of high aspect ratio cooling channel designs for a rocket combustion chamber with development of an optimized design. Technical report, Lewis Research Center, NASA Technical Memorandum 1998-206313, Cleveland, Ohio, January 1998.

[16] Marco Pizzarelli, Francesco Nasuti, and Marcello Onofri. Evolution of cooling-channel properties for varying aspect ratio. *5th European Conference for Aeronautics and Space Sciences: Progress in Propulsion Physics Volume 8*, pages 117–128, 2016.

[17] M. Naraghi, S. Dunn, and D. Coats. Dual regenerative cooling circuits for liquid rocket engines. *42nd AIAA/ASME/SAE/ASEE Joint Propulsion Conference & Exhibit*, pages 1–19, 2006.

[18] Stephen R. Turns. *An Introduction to Combustion Concepts and Applications Third Edition*, volume 3. McGraw Hill Education, 2012.

[19] S. Gordon and B. McBride. Chemical equilibrium with applications. NASA Glenn Research Center, May 1996.

[20] ANSYS. Ansys 18.1 Chemkin-Pro Theory Manual. ANSYS, Inc., January 2017.

[21] A Bakali, L. Pillier, P. Desgroux, B. Lefort, L Gasnot, J.F. Pauwels, and I. da Costa. NO prediction in natural gas flames using GDF-Kin 3.0 mechanism NCN and HCN contribution to prompt-NO formation. *Science Direct, Volume 85, Issues 7-8*, pages 896–909, 2006.

[22] Robert Zubrin and Bret Windom. Storable clean ethane-ethylene nitrous oxide engine. Pioneer Astronautics, January 2018.

[23] P. J. Linstrom and W. G. Mallard. NIST chemistry webbook, standard reference data 69, August 1997.

[24] G. H. Walterm. Thermophysical properties of nitrous oxide, September 1991.

[25] V. Gnielinski. New equations for heat and mass transfer in the turbulent pipe and channel flow. *International Chemical Engineering, Volume 16, Issues 7-8*, pages 359–368, 1976.

[26] F. P. Incorpera and T. L. Bergman. *Fundamentals of Heat and Mass Transfer 7th edition*, volume 7. Wiley, 2011.

[27] ANSYS. Ansys fluent theory guide 12.0: Turbulence models. ANSYS, Inc., January 2009.

[28] P. Karthikeyan, V. K. Ravindran, Abilash, S. Hari Krishna, N. Narayanankutty, K. M. Usha, and S. Rakesh. Prediction of erosion characteristics for ablative throat insert liners using

ultrasonic velocity measurements. *Proceedings of the National Seminar & Exhibition on Non-Destructive Evaluation*, pages 167–170, 2011.